U.PORTO
FEUP FACULDADE DE ENGENHARIA
UNIVERSIDADE DO PORTO

# Numerical modelling of damage induced by lightning strike events in composite plates

Daniel Filipe Moreira Alonso

Thesis submitted to Universidade do Porto – Faculdade de Engenharia
in partial fulfillment of the requirements for the degree of
Master in Mechanical Engineering

Supervisor
Professor Albertino Arteiro

Mestrado Integrado em Engenharia Mecânica (MIEM)
Departamento de Engenharia Mecânica (DEMec)
Faculdade de Engenharia (FEUP)
Universidade do Porto (UP)

© Porto, 2019

# Acknowledgements

First of all, I would like to express my tribute and great gratitude to Prof. Dr. Albertino Arteiro, advisor of my thesis, for providing me the opportunity to collaborate in this work. His knowledge, his availability and help, all the contributions, ideas and advices were fundamental for the development of this work.

This thesis is the end of a five year path at FEUP, therefore, I express my gratitude to all my professors and colleagues, and all that contributed one way or another for my academic path during these years. Particularly, I would like to thank Prof. Dr. Paulo Tavares de Castro for all his availability and help.

I am also ever so grateful to my parents, my brother, my grandmother and all my family for allowing, encouraging and always helping me to pursue my dreams and goals. A special mention to Max and Bart who always cheered me up and filled me with happiness.

Finally, I am very grateful to my girlfriend, Débora, who is my rock, always by my side with invaluable support.

# Abstract

The growing interest and use of composite materials in aeronautical structural applications has led to new challenges regarding the damage induced by the direct effects of lightning strikes. Contrary to metallic structures, in which this damage is limited and well-known, the damage that occurs in carbon composites is associated with several complex phenomena due to their lower electrical and thermal conductivity which leads to an increase of the thermo-mechanical constraints. The understanding of these physical mechanisms is an important concern for the design and the optimization of aeronautical structures.

The main goal of this work is to understand the effect of the lay-up parameters, such as the stacking sequence, thickness and lay-up, on the behaviour of the laminates due to the mechanical stresses originated by the direct effects of lightning strikes. For this, a 3D finite element model was developed which included inter- and intralaminar damage models of the composite material. The intralaminar damage was included through a modified continuum damage mechanics model and the interlaminar damage was modelled using a user-defined cohesive formulation. The mechanical loads focus on the main non-thermal phenomena and mechanical forces.

The stacking sequence effect is studied through a parametric analysis involving various stacking sequences, which revealed that this parameter has influence on the shape and size of the damage area, but no influence on the damage depth, as reported experimentally. The lay-up parametric study showed that thicker ply blocks leads to larger damage projected areas and also higher damage depth, again in agreement with experimental observations.

This work highlights the advantages that computational modelling can provide to the development, choice and optimization of laminates for application in an aircraft, through simulations that do not require fabrication of laminates nor expensive tests, allowing for the prediction of the laminates behaviour in a cost-efficient and time saving manner.

Future developments include studying laminates with alternative stacking sequences and lay-ups, and the definition of a model that joins the thermal effects to the mechanical effects addressed here, providing an ampler and complete information of the damage induced by lightning strikes to carbon composites.

**Keywords**: Aerospace, composites, lightning strike, direct effect, damage.

# Contents

**Acknowledgements** iii

**Contents** vii

**List of Figures** ix

**List of Tables** xiii

**1 Introduction** 1

**2 State-of-art and literature review** 5

2.1 Lightning strike in aeronautical structures and certification . . . 5

2.1.1 Lightning strike . . . 5

2.1.1.1 Thundercloud electrification . . . 5

2.1.1.2 Lightning strike mechanisms . . . 6

2.1.1.3 Types of lightning flashes . . . 7

2.1.2 Aircraft lightning certification and protection . . . 7

2.1.2.1 Lightning current waveforms . . . 9

2.1.2.2 Zoning . . . 11

2.1.2.3 Lightning effects . . . 12

2.1.3 Lightning strike damage to composite materials . . . 14

2.1.4 Lightning strike protection . . . 20

2.2 Failure mechanisms . . . 23

2.3 LaRC03 Criteria . . . 26

2.3.1 Transverse compression failure ($\sigma_{22} < 0$) . . . 26

2.3.2 Transverse tension failure ($\sigma_{22} > 0$) . . . 27

2.3.3 Longitudinal tensile fibre failure . . . 29

2.3.4 Longitudinal compression fibre failure . . . 29

2.4 Three-dimensional failure criteria for fibre-reinforced laminates . . . 31

2.4.1 Transverse compression failure . . . 32

2.4.2 Transverse tension failure . . . 32

2.4.3 Longitudinal tension fibre failure ($\sigma_{11} > 0$) . . . 33

2.4.4 Longitudinal compression fibre failure ($\sigma_{11} < 0$) . . . 33

2.5 Three-dimensional invariant-based failure criteria for fibre-reinforced composites . . . 36

2.5.1 Invariant-based criteria for transverse failure . . . 36

2.5.2 Criteria for Longitudinal failure . . . 38

2.5.2.1 Longitudinal tension fibre failure ($\sigma_{11} \geqslant 0$) . . . 38

2.5.2.2 Longitudinal compression fibre failure ($\sigma_{11} < 0$) . . . 38
2.6 Numerical modelling of damage in composite materials . . . 39
2.6.1 Damage scale . . . 40

**3 Finite element, lightning and constitutive models 43**
3.1 Geometry and finite element model . . . 43
3.2 Mechanical lightning loads . . . 47
3.2.1 Lightning current . . . 47
3.2.2 Near surface explosion of the protection layer . . . 47
3.2.3 Supersonic plasma expansion . . . 48
3.2.4 Magnetic surface pressure . . . 49
3.3 Composite damage Model . . . 50
3.3.1 Complementary free energy and damage operator . . . 50
3.3.2 Damage activation functions . . . 51
3.3.3 Damage evolution . . . 52
3.3.3.1 Transverse loading . . . 52
3.3.3.2 Longitudinal loading . . . 52
3.3.4 Damage laws . . . 53
3.4 Delamination . . . 54

**4 Model definitions and convergence study 55**
4.1 Mass Scaling . . . 55
4.1.1 Introduction . . . 55
4.1.2 Reference model analysis . . . 56
4.1.3 Discussion . . . 60
4.2 Mesh Sensitivity . . . 66
4.2.1 Discussion . . . 67
4.3 Conclusions . . . 71

**5 Finite element analysis and parametric study 73**
5.1 Stacking sequence analysis . . . 76
5.2 Lay-up analysis . . . 81

**6 Conclusions and future work 91**

**References 95**

# List of Figures


1.1 Typical lightning damage of a CFRP [7]. . . . . 2

2.1 Generalized diagram showing the distribution of electrical charge in a typical *cumulonimbus* cloud ARP5412A [16]. P indicates the positive charge regions and N indicates the negative ones. . . . . 6
2.2 Representation of an airplane triggering a lightning strike [1]. . . . . 7
2.3 Types of lightning flashes [6]. . . . . 7
2.4 The two different processes that lead to a lightning strike to an aircraft through a bi-directional leader process. (a) The interception by the aircraft of a natural lightning discharge. (b) The aircraft itself triggers the lightning discharge [22]. . . 8
2.5 Principle of sweeping process on an aircraft in flight [23]. . . . . 9
2.6 Scheme of the waveform for return current [16]. . . . . 10
2.7 Top/bottom and side view of the lightning strike zone definitions for a generic large twin-engine passenger aircraft [28]. . . . . 12
2.8 Illustration of the various direct constraints at the attachment point [2]. . . . . 13
2.9 Schematics of the damaging dynamics at the surface of a protected laminate [31]. 15
2.10 Close-up of surface damage at 50 kA [3]. . . . . 15
2.11 Schlieren photography, showing the first arc, arc-flash light and acoustic shock waves [34]. . . . . 16
2.12 SEM micrograph of resin/fiber interfacial damage after a 38 kA lightning strike [35]. 17
2.13 Current intensity effect [3]. . . . . 17
2.14 SEM micrograph of delamination area [35]. . . . . 17
2.15 Lightning strike test results of uni-directional laminates [7]. . . . . 18
2.16 Local stress distributions around a fiber break in a unidirectional composite under longitudinal tension [46]. . . . . 23
2.17 Shear failure mode of a unidirectional composite under longitudinal compression [46]. 24
2.18 a) Formation of kinking zones due to microbuckling and b) kink band in unidirectional carbon/epoxy composite under longitudinal compressive loading [46]. . . . 24
2.19 Progressive microcracking leading to ultimate failure in a unidirectional composite under transverse tension [46]. . . . . 25
2.20 a) Shear failure mode under transverse compression [46] and b) fracture plane [49]. 25
2.21 Failure mode of unidirectional composite under in-plane shear [46]. . . . . 26
2.22 Fracture of a unidirectional lamina subjected to transverse compression and in-plane shear [47]. . . . . 27
2.23 Transverse tensile strength as a function of the number of plies clustered together [47]. . . . . 28
2.24 Imperfection in fibre alignment idealized as a local waviness [47] . . . . . 29
2.25 Components of the traction vector on the fracture plane [54]. . . . . 31
2.26 Coordinate systems associated to fibre kinking [54]. . . . . 33
2.27 Kinking plane and involved shear stresses [54] . . . . . 34

**List of Figures**


3.1 Model detail. . . . 44
3.2 Seeding and mesh detail. . . . 46
3.3 Damage evolution laws for longitudinal tension (A), longitudinal compression (B), transverse tension/compression (C), and in-plane longitudinal shear (D) failure modes [68]. . . . 53

4.1 Evolution of a) displacement in the thickness direction ($U_3$) and b) deformed mesh on the top ply of the reference model. . . . 57
4.2 Crater visible on the bottom ply at 10 $\mu$s. . . . 58
4.3 Evolution of the maximum principal stress top) on the top ply and bottom) on the bottom ply of the reference model. . . . 58
4.4 Maps of top) Maximum Principal (Absolute) stress and bottom) internal variable corresponding to fibre tension failure of the 4 top layers at 40 $\mu$s. . . . 59
4.5 Maps of top) Maximum Principal (Absolute) stress and bottom) internal variable corresponding to fibre tension failure of the 4 bottom layers at 40 $\mu$s. . . . 59
4.6 Critical interlaminar element responsible for the small time step increment. . . . 60
4.7 Kinetic energy of the reference model. . . . 61
4.8 Internal energy of the reference model. . . . 61
4.9 Displacement of the centre of the reference model in the thickness direction. . . . 61
4.10 Comparison of the kinetic energy. . . . 63
4.11 Comparison of the internal energy. . . . 64
4.12 Comparison of the displacement of the centre of the top layer. . . . 65
4.13 Mesh discretization. . . . 66
4.14 Meshes of a) the reference model and b) $Mesh_1$. . . . 67
4.15 Deformed shape of a) the reference model and b) $Mesh_1$. . . . 68
4.16 Comparison of the Maximum Principal (Absolute) stress fields (top) and internal variable corresponding to fibre tensile failure (bottom) of the top layer. . . . 69
4.17 Comparison of the Maximum Principal (Absolute) stress fields (top) and internal variable corresponding to fibre tensile failure (bottom) of the second topmost layer. 70
4.18 Comparison of the displacement of the centre of the top layer. . . . 71

5.1 Geometry of the finite element model. . . . 73
5.2 Evolution of the deformed shape of the top ply of the Original model. . . . 74
5.3 Comparison of top layer fiber damage of a) the Original model at 80 $\mu$s and b) similar real tested laminate [35]. . . . 74
5.4 Measurement of the displacement in the thickness direction the Original model. . 75
5.5 Measurement of the out-of-plane velocity of the Original model. . . . 75
5.6 Deformed shape of the top ply of the Original model from top) front and bottom) back at 80 $\mu$s. . . . 76
5.7 Comparison of displacement in the thickness direction of the measurement points of model $SS_1$ and model $SS_2$ with the Original model (O). . . . 78
5.8 Comparison of displacement in the thickness direction of the measurement points of model $SS_3$ and model $SS_4$ with the Original model (O). . . . 78
5.9 Position of the measurement nodes relative to the crest of the deformed shape of a) Original and b) $SS_4$ models. . . . 79
5.10 Comparison of the measurement of out-of-plane velocity of model $SS_1$ and model $SS_2$ with the Original model (O). . . . 79
5.11 Comparison of the measurement of out-of-plane velocity of model $SS_3$ and model $SS_4$ with the Original model (O). . . . 79

5.12 Map of the envelope of the damage variable $d_1$ of the top layer of models a) Original and b) $SS_4$. . . . . 80
5.13 Map of the envelope of the damage variable $d_1$ of the second topmost layer of models a) Original and b) $SS_4$. . . . . 80
5.14 Map of the envelope of the damage variable $d_1$ of the third topmost layer of models a) Original and b) $SS_4$. . . . . 81
5.15 Detail of deleted elements throughout all plies of the UD model. . . . . 82
5.16 Comparison of a) displacements in the thickness direction and b) predicted out-of-plane velocity of the UD model and Original model (O). . . . . 84
5.17 Comparison of fibre damage of the third layer of Original, CP and AP models. . . 84
5.18 Comparison of displacement in the thickness direction of the measurement points of model CP and model $CP_1$ with the Original model (O). . . . . 86
5.19 Comparison of displacement in the thickness direction of the measurement points of model AP and model $AP_1$ with the Original model (O). . . . . 86
5.20 Comparison of the predicted out-of-plane velocity of model CP and model $CP_1$ with the Original model (O). . . . . 87
5.21 Comparison of the predicted out-of-plane velocity of model AP and model $AP_1$ with the Original model (O). . . . . 87
5.22 Maximum Principal stress (Absolute) of the third layer of models CP and CP1 at 40 $\mu$s. . . . . 87
5.23 Maximum Principal stress (Absolute) of the third layer of models AP and AP1 at 40 $\mu$s. . . . . 88
5.24 Displacement in the thickness direction of the top ply of models CP and CP1 at 170 $\mu$s. . . . . 89
5.25 Displacement in the thickness direction of the top ply of models AP and AP1 at 170 $\mu$s. . . . . 89
5.26 Comparison of the deformed shape of the lay-up alternative cases at 170 $\mu$s. . . . 90

# List of Tables


3.1 Main characteristics of the expanded copper foil. . . . . 43
3.2 Alternative cases to study stacking sequence effects. . . . . 44
3.3 Alternative cases to study lay-up and ply thickness effects. . . . . 45
3.4 Ply interlaminar and intralaminar properties. . . . . 45
3.5 Ply *in situ* properties. . . . . 45
3.6 Parameters for root radius fit [68]. . . . . 47
3.7 Parameters for the Gauss pressure fit of ECF 73 [68]. . . . . 48
3.8 Parameters for root radius expansion fit [68]. . . . . 48
3.9 Time duration of the FE steps. . . . . 49

4.1 Alternative cases to study the *mass scaling* effect. . . . . 60
4.2 Performance parameters of the models under study. . . . . 62
4.3 Maximum values of the damage variables for the two top layers. . . . . 62
4.4 Maps of the envelope of the damage variables of the top ply for the *mass scaling* analysis at 80 $\mu$s. . . . . 63
4.5 Maps of the envelope of the damage variables of the second topmost ply for the *mass scaling* analysis at 80 $\mu$s. . . . . 64
4.6 Alternative cases to study mesh sensitivity. . . . . 66
4.7 Maps of the envelope of the damage variables of the top ply for the mesh sensitivity analysis at 80 $\mu$s. . . . . 68
4.8 Maps of the envelope of the damage variables of the second topmost ply for the mesh sensitivity analysis at 80 $\mu$s. . . . . 69
4.9 Maximum values of the Maximum Principal (Absolute) stress of the two top plies for the mesh sensitivity analysis. . . . . 70

5.1 Maps of the envelope of the damage variables of the top ply for the stacking sequence analysis at 80 $\mu$s. . . . . 77
5.2 Maps of the envelope of the damage variables of the second topmost ply for the stacking sequence analysis at 80 $\mu$s. . . . . 77
5.3 Comparison between the maps of the envelope of the damage variables for the top ply of the Original model and UD model, at 80 $\mu$s. . . . . 82
5.4 Comparison between the maps of the envelope of the damage variables for the second topmost ply of the Original model and UD model, at 80 $\mu$s. . . . . 83
5.5 Maps of the envelope of the damage variables of the top ply for the lay-up analysis at 80 $\mu$s. . . . . 85
5.6 Maps of the envelope of the damage variables of the second topmost ply for the lay-up analysis at 80 $\mu$s. . . . . 85
5.7 Maps of the envelope of the damage variables for the third topmost ply of models CP, CP1, AP and AP1 at 80 $\mu$s. . . . . 88

# Chapter 1

# Introduction

Some of the most recent widebody passenger jets, such as the Boeing 787 Dreamliner and Airbus A350-XWB, feature over 50% of its structural weight in carbon fibre reinforced polymers (CFRP). These materials provide direct benefits resulting from the greater specific mechanical properties, such as increased fuel efficiency and reduced pollutant and acoustic emissions. Other indirect advantages of CFRP-intensive airframes are reduced maintenance requirements and increased passenger comfort [1, 2].

Introducing composites to the primary structure of modern aircraft arises special problems in regards to lighting strike events. Lightning strike is a threat to all structures, whether metallic or composites, and requires careful consideration from a certification standpoint. While metallic structures, such as traditional aluminium airframes, are highly conductive, CFRP have a much lower electrical conductivity. Although carbon fibres are good conductors, the polymer matrix is an excellent dielectric and therefore reduces the overall conductivity of the composite laminate [2–4].

The primary objectives of designing against lightning direct effects are to prevent catastrophic structural damage, prevent hazardous electrical shocks to occupants, prevent loss of aircraft flight control capability, and to prevent ignition of fuel vapours. The basic lightning protection regulation for airframes is the same for all vehicle categories, and appears in the Federal Aviation Administration Advisory Circular AC 25–21, Section 25.581 "Lightning Protection of Structure" [5], which requires that an aircraft is able to sustain a lightning strike without experiencing catastrophic damage. For non-metallic components, compliance may be shown by designing the components to minimize the effect of a strike or incorporating acceptable means of diverting the resulting electrical current so as not to endanger the aircraft. These requirements are inherently non-specific, and allow manufacturers to adopt different certification strategies. However, SAE provides aerospace recommended practices (ARP) that can be utilized to show compliance with these requirements [3].

CFRP materials are used in zones highly exposed to the lightning strike such as fuselage and wings. Both thermal and electrical conductivity of CFRP composites are lower than those of metallic materials. Therefore, there is a necessity to improve the conductivity of these materials to the lightning strike threat through the use of lightning strike protections (LSP). Nowadays, the most common solution is the application of a metallic mesh on the surface of the composite layers. However, the implementation of these extra protections and their certification have an impact on the aircraft weight, the design manufacturing costs and the program delay [6]. Although there is an

improvement, lightning strike still causes damage in protected composite structures, because the semi-conductive intact carbon/epoxy laminates does not conduct away the totality of the lightning currents.

To ultimately develop a lightweight and cost-effective protection for these structures, it is of paramount importance to develop a thorough understanding of the effects of the damage characteristics. These are typically evaluated by coupon lightning strike tests of the composite laminate, Figure 1.1. These coupon tests are limited in how well they can represent the aircraft composite structure behaviour, and this is where the lightning damage analysis is expected to fill the gap [7].



**Figure 1.1:** Typical lightning damage of a CFRP [7].

The objective of the lightning damage analysis is to represent the aircraft composite structure behaviour, which is difficult to evaluate experimentally. Even on a simple composite laminate, the lightning strike damage is quite complex and not fully understood. This is due to the fact that the lightning damage occurs in a very short period, typically within 0.1 milliseconds. As the industry moves towards hybrid experimental/numerical design and certification processes, the development of reliable models that accurately predict the main effects of lightning strikes in the context of damage tolerance criteria becomes crucial.

The use of advanced analytical or numerical models for the prediction of the mechanical behaviour of composite structures can replace some of the mechanical tests and can significantly reduce the cost of designing with composites while providing to the engineers the information necessary to achieve an optimized design [8].

The present study aims to increase the knowledge of damage induced by lightning strikes on the most commonly utilized laminates of the aeronautic industry. The numerical analysis is performed using the Finite Element Method, in which the material is characterized by a continuous damage mechanics model and the loading is based on a physics model of the mechanical effects of the lightning strike. Through a parametric analysis, the objective of this thesis is to show the parameters that mostly affect the onset of damage due to the mechanical effects of lighting strikes and also to present the behaviour of different laminates, thus increasing knowledge that might lead to the optimization of aeronautic structures.

The dissertation is structured into six chapters as follows:

Chapter 1 presents a general overview of the thematic of lightning strikes and aeronautical composite structures and the objectives of the present study.

Chapter 2 shows a description of all topics involved in the development of this work. The lighting strike is briefly described in an aeronautic context as is the damage produced in composite materials and its protection and certification. The failure mechanisms of composites and the

failure criteria applied with the continuous damage mechanics model are also presented in this chapter. Finally, a brief introduction to numerical modelling of damage in composite materials is described.

Chapter 3 is devoted to the description of the finite element (FE) model. In this chapter, the mechanical lightning loads applied are presented, as are the continuous damage model and the process which models the delamination of composite materials. The alternative cases for the parametric analysis are also presented.

Chapter 4 shows a study focused on the optimization of the finite element model aiming to drastically reduce the CPU time to achieve the end of the simulation. To this end, the method of *selective mass scaling* is applied to the model. It is also performed a study which analyses the mesh sensitivity of the model.

Chapter 5 is dedicated to the parametric analysis of two parameters, the stacking sequence and lay-up of the laminate. The analysis of the influence of the stacking sequence on the damage distribution caused by the mechanical effects of lightning strikes is performed varying the stacking sequence of one quasi-isotropic laminate. The study of the lay-up effect on the damage distribution is done through the use of a uni-directional laminate and two different cross-ply and angle-ply laminates.

Chapter 6 presents the most relevant conclusions of the present study.

# Chapter 2

# State-of-art and literature review

## 2.1 Lightning strike in aeronautical structures and certification

### 2.1.1 Lightning strike

Lightning is a natural and atmospheric transient, high current electrical discharge, having a path length which is normally expressed in kilometres and attempts to equalize regions of opposite electrical charges [9]. Lightning flashes originate from the formation of electrical charge in the air or, more commonly, clouds. The most common producer of lightning is the *cumulonimbus* thundercloud. Lightning can occur during snowstorms, sandstorms and in the clouds over erupting volcanos. Lightning originating in sandstorms is not in anyway different from lightning associated with thunderstorms, but can present a problem because it is an unexpected event. On the contrary lightning associated to sandstorms and volcanic eruptions are not of serious concern to aircraft [10]. There are different types of lightning flashes, being the most common *cloud-to-ground*, *intracloud* and *intercloud*. An aircraft can be stroke by any of these types but the most frequent are *cloud-to-ground* and *intracloud*.

#### 2.1.1.1 Thundercloud electrification

Thunderclouds, also known as *cumulonimbus*, are the result of atmospheric instabilities which causes air convections, combined with a significant level of humidity. Warm and moist parcels of air rise in the inner of cold air mass due to their low density. During the rise of the parcels, condensation of water vapour cause formation of water droplets, and the continuous reduction of temperature in the vertical direction induces the development of ice crystals. The different phase changes of water, changing to liquid and then to solid state, release energy through latent heat, which supplies the upward motion of convective currents, resulting in the formation of the thundercloud [6]. Electric charges within thunderclouds are a result of complex processes of freezing, melting and also by collisions and splintering [11]. There are various hypothesis for the thundercloud electrification phenomenon and the most accepted involve rebounding collisions between ice crystals and graupel pellets [12, 13]. In the graupel-ice mechanism the ice crystals which are heavier, gain a descending trajectory. As they fall through the cloud they collide with lighter particles, with ascending

movement. A charge exchange occurs within the collision, the sign and amount of transferred charge depending on the ambient temperature and the liquid water content of the hydro-meteor [14]. After the collision the lighter particle is charged positively for warmer temperatures and for either very high or low cloud liquid water content. For colder temperatures and mid-range of cloud liquid water content they are charged negatively. The positive charge accumulates at the top of the thunderclouds and negative charges will be placed at the bottom, generating a positive dipole structure. A small positive region can also exist at the base [15]. The typical structure of the vertical electric field of a thundercloud is represented in Figure 2.1.

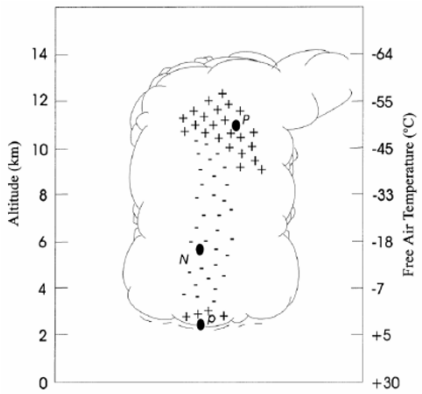



**Figure 2.1:** Generalized diagram showing the distribution of electrical charge in a typical *cumulonimbus* cloud ARP5412A [16]. P indicates the positive charge regions and N indicates the negative ones.

#### 2.1.1.2 Lightning strike mechanisms

The mechanisms which generate lightning are very complex, but can be explained in simple terms as involving a very high energy electrical discharge caused by the difference in potential between clouds or between the clouds and the ground, which lead to a disruptive electrical discharge due to the dielectric breakdown of the air between the clouds or between the clouds and the ground [17]. It is accompanied by a sound wave, thunder, caused by the sudden expansion of the air which is overheated by the electric arc.

Theoretical and experimental studies of the physical processes which occur during the development of lighting flashes have shown that lightning develops from a bi-directional leader propagation which remains a zero-net-charge channel [18, 19]. A positive electrical discharge, called positive leader, emanates from the lightning initiation zone in the direction of the thundercloud electric field to a negatively charged region. A negative discharge, the negative leader, propagates in the opposite direction onto positively charged regions. The leader propagation creates a conductive path and produces a current of a few hundred amperes inside the channel. For the case of a bi-directional propagation between a thundercloud and the ground, the negative leader that propagates toward the ground is called stepped leader. When the leader reaches the ground, establishing the connection with the thundercloud, a high pulsed current, known as return stroke, takes place [6]. The current of the return stroke can reach thousands of amperes in few microseconds and moves from the ground to the thundercloud charged regions.

Therefore a lightning strike originates from the initiation of a leader and is composed of two main components: an initial impulse and a continuing current. Most of the time, when an aircraft is struck, it triggers itself this event: in 90 to 95% of the cases, the aircraft is the one which initiates the leader and the lightning strike is caused by the presence of the aircraft in a charged

environment, Figure 2.2 . Thus a flash of lightning does not strike an aircraft randomly. The rest of the time (5 to 10%), the aircraft intercepts a forming discharge. Moreover, most of the lightning strikes happen during ascending and descending phases of the airplane, which corresponds to an altitude inferior to 5km and to *intraclouds* strikes, the less dangerous [1].

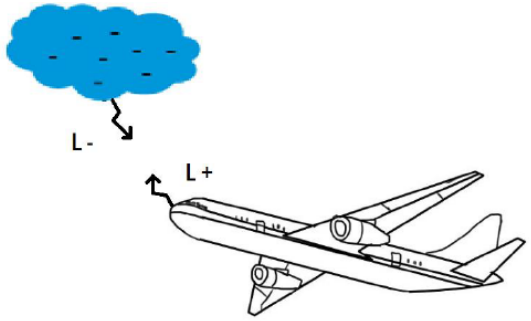



**Figure 2.2:** Representation of an airplane triggering a lightning strike [1].

#### 2.1.1.3 Types of lightning flashes

A lightning strike is due to the polarization of a cloud which unloads its excess of charges. The types of lightning can be classified based on the regions in which the lightning takes place and the polarity of the charge transferred from one region to another, as shown in Figure 2.3. A lightning flash is called *intracloud lightning* (IC) when the two charged regions belong to the same single cloud, the most common type. It can also be generated from two opposite charged regions of two different clouds, known as *intercloud lightning* (CC). In the case of lightning flash between cloud and ground it is called *cloud-to-ground* lightning (CG). This type is also classified by the polarity of the transported charges. Around 90% of lightning flashes that strike the ground come from the negative charged regions of clouds, and are named negative ground lightning (-CG), the other 10% are called positive ground lightning (+CG) and come from the positive charged regions of the cloud [9, 20].

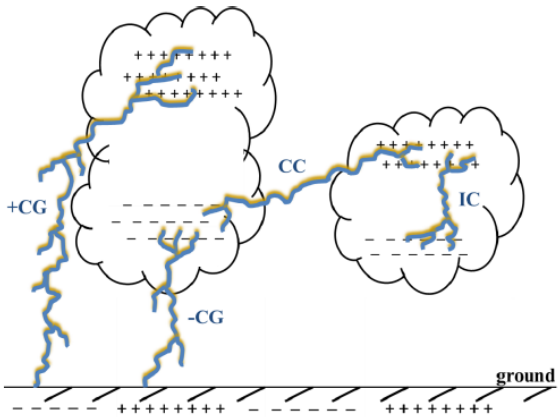



**Figure 2.3:** Types of lightning flashes [6].

### 2.1.2 Aircraft lightning certification and protection

An airliner has the average probability of being stroke by a lightning every 1,000 to 10,000 flight hours, shown by statistical analysis during flights [21]. That is dependent on various parameters such as: type of aircraft, local climate, route of flight, etc. For a commercial airliner, this is approximately one lightning strike every year. Lightning strike to aircraft presents more difficulties

than lightning strike to grounded structures. The shape of the stroked object locally enhances the electrical field, in both cases. But in aircrafts the amplification coefficient of the electrical field, defined by the ratio of the local field over the ambient atmospheric field, may reach 5 to 10 at the extremities, as for instance at the wings and at the tip of the stabilizers. When an aircraft triggers the lightning or when intercepts a forming discharge it is called the phase of lightning initiation, which lasts for a few microseconds. It is followed by the high current phase which lasts from tens to hundreds of milliseconds. During this phase the attachment point of the lightning to the aircraft assumes various positions due to the relative movement of the aircraft to the lightning, which is known as the *swept stroke*.

The lightning initiation phase is characterized by the development of a positive discharge from the aircraft, followed by, a few milliseconds later, the inception of a negative discharge propagating in the opposite direction, thus forming a bi-directional leader, Figure 2.4. Throughout all the lightning strike the aircraft is part of a continuous current path, generating two attachment points, generally, one entry point and one exit point. These are defined by the direction of the current, thus the entry point will be at a cathodic surface (negative electrode) and the exit point at an anodic surface (positive electrode). Consequently, the exit point is the attachment point of the positive leader and the entry point is the attachment point of the negative. The lightning will be of an intracloud or an intercloud if the discharge is bi-directional throughout the strike leader. If one of the bi-directional leaders reaches the ground, the aircraft forms a part of a cloud-to-ground lightning [22].

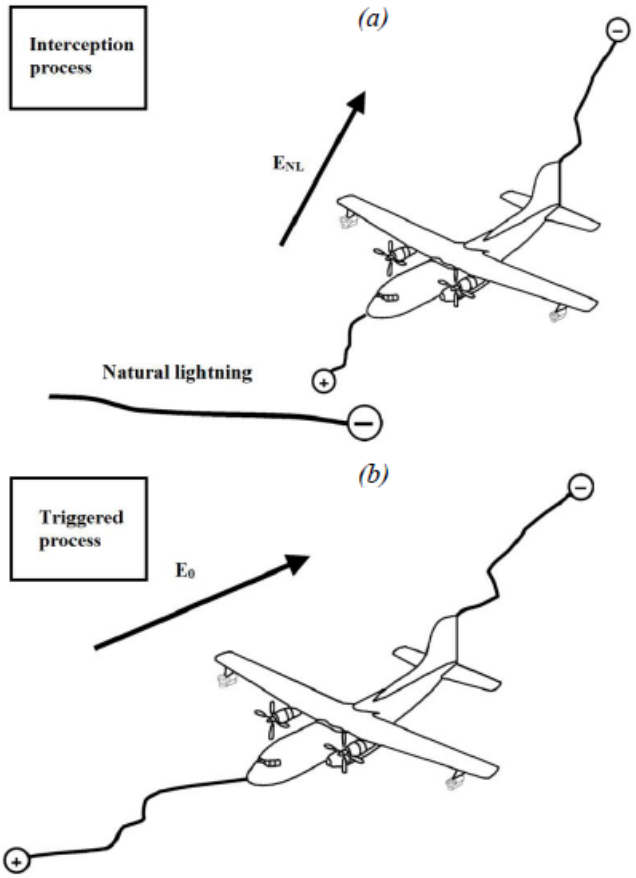



**Figure 2.4:** The two different processes that lead to a lightning strike to an aircraft through a bi-directional leader process. (a) The interception by the aircraft of a natural lightning discharge. (b) The aircraft itself triggers the lightning discharge [22].

Once an aircraft has been struck, the lightning arc will be developed between a stationary electrode, the cloud or ground, and a moving electrode, the aircraft. During this period the aircraft is in motion, relative to the stationary electrode, consequently the lightning channel attachment point will differ for distinct instants of time, the *swept stroke* phenomenon, Figure 2.5. In this phase the current is higher than in the initiation phase.

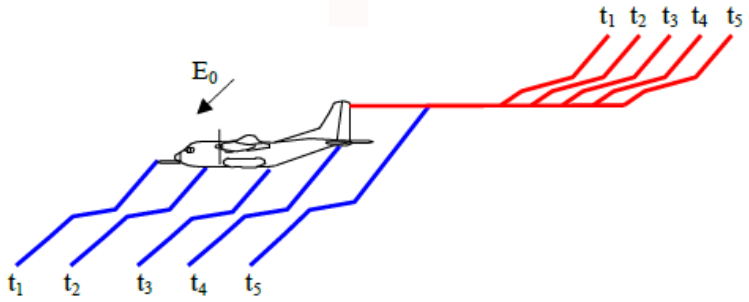



**Figure 2.5:** Principle of sweeping process on an aircraft in flight [23].

As an aircraft is expected to fly regardless of weather conditions it is likely to fly through conditions in which it will be struck by a lightning. A lightning strike can induce damage to the aircraft, therefore it is a potential safety hazard. As such, it is necessary to take into account this possible damage in the design phase of any aircraft. Lightning protection is designed to prevent or minimize this damage, improving durability and reliability of the aircraft on such events. The design must meet requirements set by certification authorities which guarantee the proper performance of the aircraft in the case of an upper bound lightning strike. Basic recommendations, to protect aircraft against catastrophic effects of lightning, are indicated by Civil certification authorities, such as EASA (European Aviation Safety Agency) and FAA (Federal Aviation Administration). EUROCAE (European Organization for Civil Aviation Equipment) and SAE (Society of Automotive Engineers) are standard committees that establish guides and normative to achieve these requirements. Thus, protection of an aircraft is based on standards and certification steps. These can be divided into three. The first step comprises the definition of the lightning environment specified by means of a standardized current waveform. The second step is called "*zoning*" in which the aircraft is divided into different zones with different levels of risk of arc attachment and swept zones. The final step is the determination of the direct effects the lightning has on materials, equipment, systems and structures, through experimental testing [6].

#### 2.1.2.1 Lightning current waveforms

Lightning is a natural phenomenon, thus it is unpredictable. Its current and waveforms vary considerably for each lightning. To study and certify an aircraft it is necessary to use an adequate current and waveform which can be representative of conditions encountered in flight. The SAE Aerospace Recommended Practice ARP5412 [16] quantifies the environment and levels which represent the minimum currently required by the certifying authorities. This report is internationally considered as the sole standard concerning the lightning threat. This threat is defined using data of lightning to the ground [24].

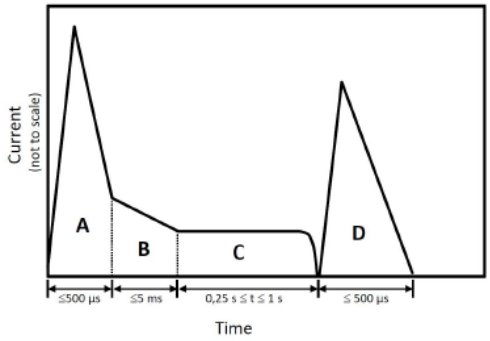



**Figure 2.6:** Scheme of the waveform for return current [16].

Several current waveforms were derived to represent the lightning environment, and to give upper bounds of the direct effects of lightning on aircraft, Figure 2.6. These waveforms represent idealized environments, which are to be applied to the aircraft for purposes of analysis and testing. They are not intended to replicate a specific lightning event, but they are intended to be composite waveforms whose effects upon aircraft are those expected from natural lightning. Lightning is composed of an initial stroke, an impulse and a continuing current [3].

For each waveform, peak current amplitude, action integral and time duration are the primary parameters that dictate the response of the structure. The action integral is a measure of the intensity of the strike, and therefore to ensure that the strike accurately simulates the real lightning event, it is important to ensure that such quantity is as high as specified by the requirements [3].

In the normalization document the lightning flash to be used to evaluate direct effects on aircrafts is composed of four different current components A, B, C and D, Figure 2.6.

The current wave is defined by the following parameters:

- The intensity peak of the current.
- The rise and descent times of the wave front.
- The electrical load transferred equals to $\int i\mathrm{d}t$ (C).
- The action integral equals to $\int i^2\mathrm{d}t$ (in $\mathrm{A}^2$.s or $\mathrm{J}/\Omega$) which represents the ability of the current to deposit energy on a resistive object.

Each component represents a different phase of the blasting current:

- Component A: Current of the first return stroke, this component has a peak intensity of 200 kA ±10%, an action integral of $2 \times 10^6$ $\mathrm{A}^2$.s ±20% and a total duration of 500 $\mu$.s at the maximum. The rise time from 10% to 90% of the peak value must be smaller than 50 $\mu$.s (compared to the component D). This component can cause damage by direct effects or indirect effects.
- Component B: intermediate current, average amplitude of 2 kA ±20% and an electrical load transferred of 10 C ±10% during 5 ms ±10%. This component corresponds to a transition phase of the discharge.

- Component C: continuous current, this component transfers an electrical load of 200 C ±20% during a time between 0.25 and 1 second, with intensity from 200 to 800 A. This component of limited amplitude can cause very important damages (in particular thermal ones) because of large quantity of electrical charges that it deposits.
- Component D: current of the subsequent return stroke, has a peak intensity of 100 kA ±10%, an action integral of $0.25 \times 10^6$ $A^2$.s ±20% and a total duration of 500 $\mu$.s at the maximum. The time from 10% to 90% of the peak value must be smaller than 25 $\mu$.s.

This standardized current waveform is applied by manufacturers to aircraft parts and structures in order to test, evaluate and certify the direct and/or indirect effects caused by lightning strikes. This is done by test campaigns where the material is subjected to this standardized lightning strike, most of the times following the guidelines defined by SAE or EUROCAE. Due to high temperatures and current intensity induced by the electric arc, only very few instrumentation can be applied to the specimens. Quantitative real-time measurement can only be obtained in the rear face of the specimen, face opposed to the one in which the electric arc is applied. The data measured is the velocity at chosen locations around the centre of the sample during the electric shock, and the displacement is derived from it. The velocity can be measured using a Velocity Interferometer System for Any Reflector (VISAR), with a velocity range of 0.01 m/s to 3,000 m/s with less than 1% error [1].

#### 2.1.2.2 Zoning

The lightning sweep stroke generates a series of discrete attachment points along the sweeping path, consequently the attachment point may dwell at various surface locations for different periods of time [25]. Therefore individual locations of an aircraft are exposed to different lightning current components. The dwell times at each attachment point vary according to the nature of the surface, the local geometry, the air flow and the current waveform which could cause reattachment if a current peak occurs [26]. Various studies have been carried to establish a map of the zones where lightning is often attached. The documents EUROCAE ED-91 [27] and SAE ARP5414A [16]divide an aircraft into different lightning zones. The purpose of lightning zoning is to determine the surfaces of the aircraft which are likely to experience lightning attachment.

- **Zone 1 -** Surfaces of the aircraft for which there is a high probability of initial lightning arc attachment (entry and exit areas).
- **Zone 2 -** Surfaces of the aircraft for which there is a high probability of lightning flash being swept from Zone 1 (point of initial arc attachment).
- **Zone 3 -** This zone includes all of the remaining airplane areas not covered by Zones 1 and 2. In this zone there is a low probability of an attachment of the lightning arc. However, Zone 3 areas may carry substantial lightning currents by direct conduction between the attachment (entry and exit) points.

Zones 1 and 2 are subdivided into A and B regions depending on the time that an arc stays attached to the zone considered. For a region of suffix A, there is a low probability that the lightning arc stays attached, while a B region has a high probability that the lightning arc remains attached. The location of lightning strike zones on an aircraft is determined based on its geometry and operational factors. The document EUROCAE ED-91 [27] defines the standard rules. Figure 2.7 presents an example of lightning strike zoning for a generic transport aircraft [28].

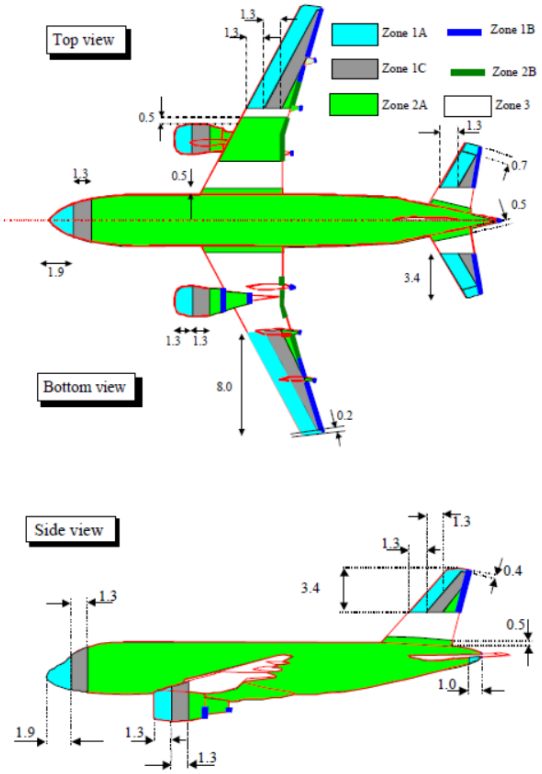



**Figure 2.7:** Top/bottom and side view of the lightning strike zone definitions for a generic large twin-engine passenger aircraft [28].

To assess the structural damage inflicted, laboratory experiments have the lightning current waveform associated with the zoning area from which the airframe part originates.

- **Zone 1A -** A + B + C*. C* is a reduced C component. An average current of 400 A is applied for 50 ms ±10% to deliver 20 C ±20%
- **Zone 1B -** A + B + C + D.
- **Zone 1C -** Ah + B + C*. The impulse Ah corresponds to a "lower" impulse A. Peak amplitude of 150 kA ±10%, Action Integral $0.8 \times 10^6$ $A^2$.s ±20%, Rise time 37.5 $\mu$s. Time duration $\leqslant$ 500 $\mu$s.
- **Zone 2A -** D + B + C*.
- **Zone 2B -** D + B + C.
- **Zone 3 -** A + C. The current is applied by conduction and not by arc attachment.

#### 2.1.2.3 Lightning effects

Lightning strikes induce various effects on an aircraft, these effects are mainly divided into two categories, direct effects and indirect effects.

Direct effects are associated with physical damage to structures at the attachment points, where

the current is more concentrated and intense, and to equipment, triggered by the attachment of the lightning arc to the fuselage. Direct effects are nowadays of primary concern because of the massive use of composite material in the aircraft structure. CFRP composites have poor electrical and thermal conductivity, when compared to metals, therefore are unable to conduct the high electrical currents and electromagnetic forces sufficiently to prevent structural damage. These effects introduce certain constraints which can be divided in two main categories, thermal and mechanical constraints [3].

Thermal constraints are present at the attachment points and in other parts in which significant current circulates, and they can cause deformation, melting or puncture of the fuselage. In other areas, they can produce explosions of conductors and generate hotspots. There are two main energy sources for these constraints, direct plasma heat flux and Joule resistive heating effect. Joule heating is more important when the material is resistive, the case of composite materials. Direct plasma heat flux has three possible mechanisms: conduction, electronic or ionic recombination and radiation flux [2].

Mechanical constraints may lead to breaking, delaminating and puncture of materials, particularly during current peaks. There are three potential sources for these constraints. The first is the overpressure resulting from the explosion of the lightning channel followed by the propagation of a strong shock wave through the radial direction of the arc. The explosion is generated from the fast increase in the arc temperature in a very small time interval, of a few microseconds. Another component with significant contribution to the mechanical constraint in the arc column and material is the magnetic force induced by the current circulation. The internal pressure of the arc column is reinforced by the concentric magnetic force, *magnetic pinch*, and also by the current flowing in the structure which acts as an additional mechanical constraint on the skin, *magnetic pressure*. The last source is the expansion which results from the very fast increase in temperature of the material. In addition to these sources, there are also other constraints such as dielectric breaking at the lightning attachment point or sparking at junctions and fasteners, Figure 2.8.

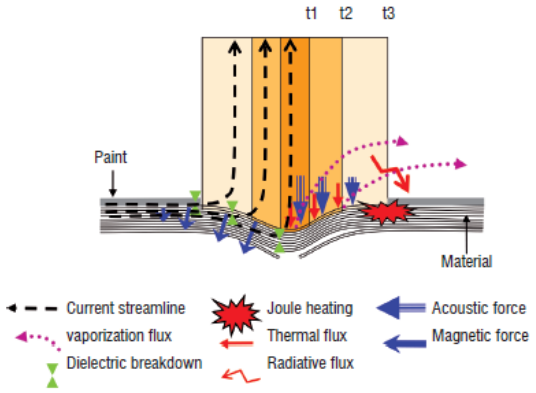



**Figure 2.8:** Illustration of the various direct constraints at the attachment point [2].

Indirect effects concern damage resulting from the interaction of high electromagnetic fields with electrical/electronic systems in the aircraft, denominated electromagnetic coupling. When subjected to a lightning strike, a current waveform, composed by many high current peaks, flows through the entry point. This electric current then travels all over the electrical system of the aircraft until it reaches the exit point. The difference of potential on impedance systems can make them act like source generating malfunction in the electronic equipment on board. These currents are a central matter for all that concerns electromagnetic compatibility.

### 2.1.3 Lightning strike damage to composite materials

Recent aircrafts have seen an increase of usage of composite materials in its structure. These materials have been applied for many decades in the interior and other non-structural elements, due to their low weight. In the last three decades the knowledge and development of these materials allowed for their introduction in structural elements. Due to their strength and lightweight, carbon fibre reinforced polymers (CFRP) are used in various parts of the aircraft, such as fuselage, wing boxes structural spars, etc, [6]. They have been replacing metallic materials in the structural functions for the sake of reducing overall weight and reduce fuel consumption. In some of the recent and advanced commercial airliners, such as the Airbus A350XWB and the Boeing 787 Dreamliner, around 50% weight of the aircraft is made of carbon composites, including the totality of the fuselage and most of the wings. These are zones highly exposed to the elements and more importantly to lightning strikes, originating difficulties in their design due to the lightning direct effects [3, 4].

The usage of CFRP composites brought new problems to the design of aircrafts due to their low conductivity, unlike metallic materials, to electrical currents and temperature, which means that high electrical currents and electromagnetic forces can produce significant structural damage. The electrical conductivity of a carbon tow, 60 $kSm^{-1}$, is much lower than that of aluminium, 37,000 $kSm^{-1}$ [6].

The electrical conductivity of a CFRP is highly dependent on the orientation of the carbon fibre: parallel conductivity (in the direction of the fibres, having the same order of magnitude of the conductivity of a carbon tow), transverse conductivity (transverse to the fibres), and through-thickness conductivity (in the thickness direction, between different layers) [29, 30].

Advanced composites have great mechanical properties but have the disadvantage of developing large strength degradation because of internal damage such as delamination and matrix cracks. Two important sources of internal damage related to aircrafts are impact through tool dropping and fragment hits during manufacturing, maintenance or operation, and lightning strikes. Damage to a composite such as a direct effect of a lightning strike during a flight may be a major issue in terms of aircraft durability and long-term operation [30].

Damage in carbon laminates due to a lightning strike is a complex multi-physical phenomenon, involving different forces. Hence, it is difficult to predict damage generated by a lightning strike on composite structures [30–32].

The lightning current while flowing in the structure generates a magnetic force (Laplace force) and Joule effect. The Joule effect phenomenon leads to a quick elevation of temperature in the materials close to the surface (metallic protection and first plies of the laminate), in conjunction with the energy transfer from the arc root that induces vaporization of the surface protection and disappearance of the paint layer, originating an explosion phase which is confined by the paint coating covering the structure. Surface explosion has therefore two contributors: vaporization of the metallic protection and vaporization of the resin impregnating the first plies of the laminate [32].

Thus, the complexity of the damage is not only due to the structure configuration but it is also influenced by paint and metallic protection, Figure 2.9, making the effects of these non-structural elements on damage very important [31, 32].

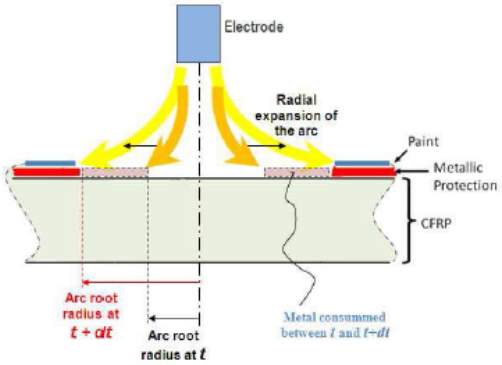



**Figure 2.9:** Schematics of the damaging dynamics at the surface of a protected laminate [31].

Damage phenomena are usually modelled within an electrical and thermal framework. In such models, energy is injected in the material by Joule effect induced by the circulation of electrical current through the material and protection as well as by heat transfer with the arc root. This energy input results in heating of the protection and material possibly followed by melting and vaporization. The extension of damage is assessed on the basis of the amount of these liquid or vapour phases. Such an approach is well adapted to describe damage on metals and has been extended to carbon fibre composite materials for the continuous C component. Thus, burnings and surface damage have mainly a thermal origin [31].

In depth damage is caused by more complex processes which involve mechanical effects in conjunction with thermal ones. Two types of damage can be segregated by their origins: surface and bulk damage. Surface damage is induced by thermal effects mainly on the metallic protection, while bulk damage is induced by mechanical stresses propagating through the material.

Surface damage can be understood on the basis of a thermal model, involving heating, melting or vaporization of the metallic protection and possibly of the composite topmost layer. Evaluation of the energy deposited there by Joule effect and by heat transfer from the plasma arc provides a time dependent damaged area in good agreement with test results.

Surface damage is the visible damage and manifests as fibre fracture, splitting, bulging, ply-lift and resin vaporization and in some cases the upper ply or plies even separate in small chips or fragments and leave an empty space on the surface, Figure 2.10. This damage is confined to the surface and in the region immediately surrounding the lightning attachment point [3, 30].

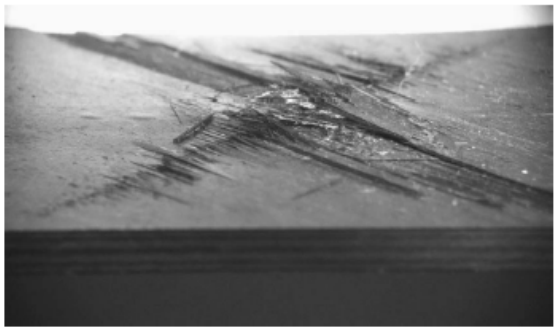


**Figure 2.10:** Close-up of surface damage at 50 kA [3].

Bulk damage is the result of a mechanical stress due to externally applied forces to the material and manifests has fibre-resin debonding, transverse cracks, fibre rupture and ply delamination [31, 33]. Mechanical stress fields are caused by the transferred momentum, which has two different sources: (1) mechanical forces due to air and surface explosion shock waves and explosive damage

of the resin and (2) electro-magnetic forces, Figure 2.11. These are the dominant contributions, which can be enhanced by the confining effect of the paint [31].

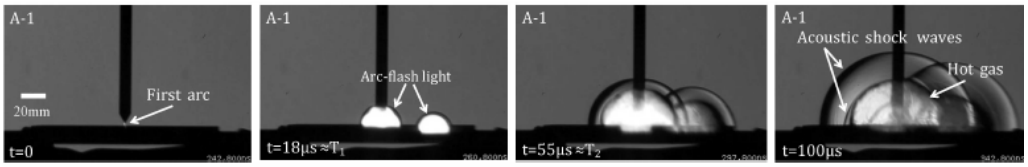



**Figure 2.11:** Schlieren photography, showing the first arc, arc-flash light and acoustic shock waves [34].

When a lightning strikes, a large amount of energy is delivered very rapidly, causing the ionized channel to expand with supersonic speed. If the shock wave encounters a hard surface its kinetic energy is transformed into a pressure rise, which causes damage to the structure.

On the other hand, resistive heating leads to a temperature rise, and in turn it initiates a breakdown of the resin/fibre interface by pyrolysis and gas release from the reacted resin. If the gases developing from the burning resins are trapped in a substrate, their rapid evaporation in inter-laminar layers results in an explosive fracture in the vicinity of the lightning strike attachment point causing damage to the structure. Inside the laminate the complex damage state comprises pyrolysed fibres, vaporized resin, and traces of inter and intra-ply arcing [3, 30, 35]. Thus, the combination of a shock wave event and a rapid evaporation of resin through resistive heating is a major cause of explosive damage of the surface plies.

CFRP laminates have anisotropic electrical properties in their transverse and thickness directions. The fibre volume fraction highly influences the specific electrical resistance of a laminate. A thicker resin interlayer laminate improves impact damage resistivity but also acts as an insulator to electrical currents and increases the specific resistance in both directions. Fibre damage is majorly caused by shock waves due to supersonic-speed expansion of the ionized leader channel when a return stroke occurs [30], and can be seen as an external demonstration of gas explosion inside the laminate. When the lightning strike intensity is low, the impact of gas explosion is not enough to break up fibre yarns, thus only delamination damage is created. As the strike level increases, the energy of gas explosion not only produces delamination, but also extends its impact to the surface and leads to the fibre damage [35].

Hosokawa et al. [36] tested skin panel specimens with different electrical properties, and concluded that those with lower electrical resistivity and higher thermal conductivity fibres had a better performance in regards to damage by lightning strike. The lightning current would flow fast enough through the specimen causing less damage. Also, the higher thermal conductivity allows the resistive heat, produced by Joule effect, to disperse faster leading to smaller delamination areas, thus avoiding severe damage.

Resin deterioration is the combined effect of resistive heating of the surface layer and high atmospheric temperature due to insulation breakdown of air. The high atmospheric temperature generated by the introduction of a large amount of energy to the leader channel causes resin evaporation and deterioration in the same way as resistive heating, Figure 2.12. Around the ionized leader channel of a natural lightning strike the temperature reaches up to 30,000 K [37], the starting temperature of pyrolysis for common epoxy resins being around 600 K, which is considerably lower than the heated atmospheric temperature due to lightning strikes [30]. Not only the electrical conductivity of the matrix resin properties affect the damage, but also the onset temperature of thermal decomposition, char yield, interlaminar fracture toughness and other material properties strongly affect lightning strike damage [33].

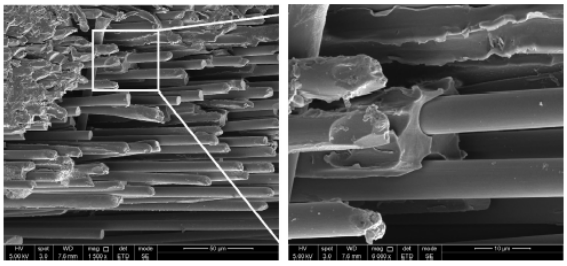


**Figure 2.12:** SEM micrograph of resin/fiber interfacial damage after a 38 kA lightning strike [35].

The intensity of the current has a relation with the damaged area. The increase of lightning conditions leads to an increase of the damaged area [3, 36], Figure 2.13.




**Figure 2.13:** Current intensity effect [3].

Delamination induced by lightning strike is a significant failure mode and can extend well beyond the visible damage area [30, 35, 38]. The lightning current that propagates inside the laminate generates Joule heating along the fibre direction, due to its good conductivity. Then, the interfacial bonding of the matrix with its adjacent fibres is severely damaged and the resin between sub-layers is broken up into small pieces under the influence of thermal–mechanical interacting stresses. The resin pyrolysis into gaseous substances, which remain entrapped in the interlaminar zones. Subsequently, the high temperature and pressure and limited volume space leads to a gas explosion causing delamination damage [35], Figure 2.14. Core delamination is originated by a mechanical stress field induced by mechanical forces generated at the surface of the panel which propagates through the laminate and reaches, at some interfaces, the delamination thresholds [32]. In such a process, the main contributor to delamination appears to be the surface explosion induced by the vaporization of the materials close to the surface [31]. Delamination can progress easily because of the lower interlaminar fracture toughness caused by thermal decomposition of the matrix resin [33], and it is clearly distinguished from resin damage which indicates that the cause of damage propagation of these two modes is different [30]. Damage tolerance to lightning strikes is therefore a critical aspect of composite airframe design.

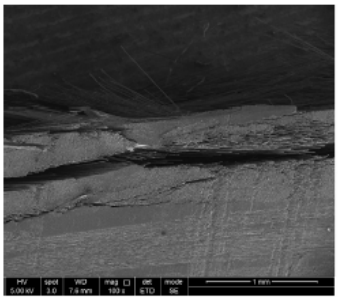


**Figure 2.14:** SEM micrograph of delamination area [35].

Experimental results show that the residual compressive strength is highly and negatively af-

fected by the damage inflicted by lightning strikes [3].

The response of CFRP laminates to lightning strikes is assessed by experimental tests according to regulations. Hirano et al. [30] found little influence of the variation of the testing panels size and thickness on the damage response for each damage mode.

Lay-up parameters, such as ply thickness and relative fibre angle, have influence on the damage induced by lightning strikes, as shown by experimental tests. Ply thickness is the number of stacked layers which have the same fibre orientation and the relative fibre angle is the difference of fibre angle between two adjacent layers.

Thicker ply blocks usually lead to a larger projected damage area [39, 40]. Hosokawa et al. [36] also concluded that thicker pitch-based carbon fibre skin layers have higher resistance to lightning-induced damage. Results of experimental tests on specimens allowed to observe that thicker skin panels have better ability to protect the core layers from damage caused by lightning strikes. Therefore, specimens from thicker skin panels show smaller damaged area than those from thinner skin panels. Kawakami also found that if the second ply was thick enough the lightning energy would not reach the second interface, thus limiting delamination to the first interface only [39].

Mamizu et al. [7] performed tests on different uni-directional specimens and compared the results with multi-directional specimens. The observed damages were similar in UD laminates but considerably different when compared to the quasi-isotropic laminates. In UD laminates, the damage footprint was shallow and mostly limited to the resin matrix, Figure 2.15. The lightning current seemed to stay near the surface, without penetrating the laminate.



**Figure 2.15:** Lightning strike test results of uni-directional laminates [7].

In his experiments, Kawakami [39] concluded that the stacking sequence influences the projected damage area by changing its shape. Also, even though the projected damage area is dependent on this parameter of the lay-up, the damage maximum depth is not.

Li et al. [35] tested similar specimens with different stacking sequences, $[45_2/0_2/-45_2/90_2]_s$ and $[30_2/0_2/-30_2/90_2]_s$, and found that the different fibre relative angles produced dissimilar delamination and fibre damage patterns. The two specimens were tested at the same current levels and the energy transferred by Joule heating was considered similar, generating equal amount of gases which were responsible for the internal damage.

Li et al. [35] concluded that small cells, which enclose the produced gases, are formed around the 0° direction. The explosion of the trapped gases due to the quick elevation of temperature and pressure increases damage. In the 30° specimen the small angle between sub-layers seems to confine the Joule heating to a smaller area leading to a higher damage. The 45° specimen revealed less damage which was attributed to the larger angle allowing a better dispersion of the Joule heating to a greater area. Thus, delamination seems to be influenced by the stacking sequence. Also, it can lead to fibre breakage if the explosion has high enough intensity.

The impulse waveform of artificial lightning applied in design and experiments is characterized by several lightning parameters which show strong relationship with certain damages modes [30,

35, 40, 41]. These lightning parameters are, according to the literature [30, 35, 39], maximum current, waveform, electrical charge, and specific energy (action integral).

The fibre damage area and the maximum damage depth increase almost linearly with increased peak current. Since both damage modes correspond to the same parameter they can be assumed to be the same damage mode. The resin deterioration area increases with an increasing electrical charge, this relation being non-linear. The delamination mode appears to have a dependence on the action integral of the impulse current.

Paint has influence on the damage inflicted due to the confinement of explosive gases, thus, paint thickness influences this confinement and has a strong relation with damage [32, 42]. Airbus studies have shown that, for thin carbon laminate flat panels protected with Expanded Copper Foil (ECF), there is a threshold effect. For paint thinner than 200 $\mu$m the delamination induced by lightning is small whereas, for thicker paint configurations, the damage increases with the paint thickness [32].

The behaviour of the paint layer can be resembled to a thick dielectric film over the metallic protection and produces two effects:

1. prevents the arc to expand freely (dielectric constriction effect) and dissipate its energy into the metal protection;

2. induces a mechanical confining effect which enhances the shock wave generated by the explosion induced by the sudden vaporisation of the metallic protection due to Joule effect.

This inertial confinement effect enhances the magnetic and arc overpressure due to a reduced arc radius. The confined surface explosion is an empirical evidence [43].

On their experimental tests, Murillo et al. [42] concluded that a small variation on the thickness of the paint can lead to a major increase in the size of the damage induced. Also, a thicker paint layer is associated to a faster deflection of the panel, which demonstrates the role of the thickness of the dielectric layer in the mechanical constraints sustained by the panel. Regarding the thickness of the panel, it does not affect on the amount of paint removed from the surface, and therefore the surface phenomena. However, thicker panels presented smaller bulk damage. Hence, thicker panels provide better tolerance to the mechanical forces, generated by a lightning strike. Because the thickness of the paint layer has such remarkable effect on the behaviour of composite panels subjected to lightning strikes, it should be carefully controlled, not only during the first painting process but also during repairing and repainting stages. The paint system should be designed to be easily stripped.

Water absorption seems to also have an influential role on the damage by lightning strike [41]. Hygrothermal ageing of the composite material influences the various damage forms leading to an enlarged damage zone, namely larger delaminations and a ply oriented fibre damage profile. Li et al. [41] also showed that the stacking sequence has a great effect on the behaviour of composites subjected to water absorption. An example with a fibre relative angle of 45° presented a current threshold level. When the current was lower than 10 kA, the residual strength showed an improvement, but for higher currents a decrease in the mechanical properties was observed. A composite with a fibre relative angle of 30° had a more significant decrease of the residual strength and no threshold, showing how the stacking sequence influences the effect of hygrothermal ageing on the mechanical properties.

### 2.1.4 Lightning strike protection

Lightning strike is a primary threat for composite structures, such as wind turbine blades and aircraft structures. In order to prevent damage to composite structures by lightning strikes, various kinds of protections have been developed [36].

An effective lightning protection, ideally, should have certain characteristics:

- Good conductivity in order to quickly spread lightning currents;
- Admissible low fusion and vaporization temperature;
- Must be as lightweight as possible;
- Corrosion resistant;
- Good mechanical properties;
- Easy to handle and form complex shapes around complex structure elements;
- Low cost and easy to maintain and repair.

Also, it should be applied at the surface of the panel making maintenance and repair easier and safer for the structure by keeping the majority of the current on the external part of the panel, protecting the inside. The protection function is to absorb and spread the energy induced by the lightning strike, so that through its conductivity the current is not confined to a small area, reducing the risk of severe damage. It is important to stress, however, that the paint, which is dielectric material, reduces the effect of the protection.

One major disadvantage of these protections is the weight. Composite materials are employed in order to reduce the overall weight of the aircraft. However, when the protection is applied to cover the whole composite structure, the weight gains are seriously reduced.

The most commonly studied protections are [44, 45]:

- Metallic wire mesh;
- Sheet or Expanded Copper Foil (SCF and ECF);
- Conductive paints (metallic paints);
- Coated carbon fibres;
- Carbon nanotubes.

**Woven wire fabrics** - Metallic woven wires are added to the outer ply of the CFRP laminate, typically these are woven in a 2D configuration. The periodic appearance of the wires within the CFRP ply intensifies the electric field at a multiplicity of locations, supporting in dielectric breakdown and multiple lightning attachment points which results in a significant arc root dispersion. Lightning tests have shown that interwoven wires provide a significant reduction in damage compared to unprotected samples. Simulated lightning strikes indicate that the stroke currents enter a wide area of the laminate surface and usually vaporize the exposed portion of wires. However, interwoven wire fabric tends to cause cracking of the laminate due to the differential coefficient of thermal expansion and/or due to explosion of the metallic wire caused by lightning current loads. Although, the damage may be limited to the outer CFRP plies, this is considered as a severe drawback of the interwoven wire protection measures [44, 45].

**Solid Metal Foils (SMF)** - Consists of a thin layer of metal deposited on the top surface of the laminate, most of the time, embedded in a layer of resin in order to insure their adhesion to

the material and provide an additional conductive layer to the structure. Metal foils of 0.001 in (0.025 mm) or greater thickness provide protection for the composite that is about the same as that provided by wire woven. However, and in spite of the excellent protection abilities of such foils, manufacturing concerns have limited their application at large scale in industry. It is actually extremely complicated to drape these foils over large or curved surfaces and structural parts. To do so, one is obliged to cut the protection to prevent the formation of wrinkles on which the arc may attach and provoke delamination and damage due to a failure of the protection layup. The presence of seams, due to the cutting of the protection can also result in unbounded areas that can confine moisture and thus deteriorate the foils by corrosion. Due to these difficulties solid metal foils are less commonly employed than other protection options [44, 45].

**Expanded Metal Foils (EMF)** - Expanded foils are created from SMF by a milling process that perforates and stretches a solid metal foil. Such foils resemble woven wire mesh but they are made out of a single piece of metal, which insures a better general conductivity to the foil because of the lack of contact between the wires. They are typically 0.05 to 0.1 mm thick and are widely used in aeronautics. The expanded foil can be done with aluminium, bronze or copper, which provides the most effective lightning protection. Fewer difficulties are encountered for draping EMF over large or curved surfaces than with SMF, as they can be stretched up to certain degree. They efficiently promote arc root dispersion and reduce thermal and shock wave damage. It should be noted that the expanded metal foils provide a good electromagnetic shielding due to the good contact afforded with the mechanical fasteners and hard metal surfaces. However, after a lightning strike, the mesh is generally vaporized at the arc root area. This is due to the thermal flux coming from the arc root and to the Joule effect inside the metal wires. The wires diameter varies between 50 $\mu m$ and 250 $\mu m$ and so the current densities inside the metal wires are very high. Even if the electrical conductivity is good, the energy due to Joule effect is not negligible inside the metal wires and can damage the metal meshes. In order to ensure an efficient bonding between the composite and the metal mesh, the metal mesh is partly embedded in the first resin thickness of the composite material. And so, a part of the lightning current can circulate in the carbon fibre, which might damage the composite material by Joule effect [44, 45].

**Conductive paints** - Another way to ensure more conductivity to a protected structure would be the use of a more conductive top layer applied above the composite materials. Paint, which is usually added for purely decorative or advertising purpose, could by this way be functional. The addition of conductive particles to the paint can be a way to increase the conductivity on all exposed surfaces of the plane. Conductive metallic particles or carbon allotropes are embedded in the polymer matrix. Carbon, aluminium or copper particles are the particles commonly added to the paint that covers the structure providing a certain amount of conductivity to the mechanical parts and thus lightning protection. The advantage of carbon allotropes is their high conductivity with low specific weight, enhancing relatively high loading without affecting the rheological properties and reducing mechanical properties. However, the results of this protection are marginal because the conductive particles are randomly scattered and seldom are in contact with each other [44].

Another concept is ionizable paint. These paints are composed of classical polymer matrix charged with special pigments which have a low ionisation potential. Ionizable paints can be used just as classical aeronautic paints. Neither conductive nor ionizable paints can provide a sufficient lightning protection level. They can only be associated with other protection measures, to minimize the adverse effects of conventional paint systems [44].

**Coated carbon fibres** - The electrical conductivity of carbon fibres can be enhanced by

metallic coatings. Metals can be deposed on fibres using e.g. the electroplating method or the colloid spray method. Carbon fibres are electroplated with metals such as copper or nickel, prior to their resin impregnation. Nickel is the most used electroplated metal due to the fact that it is relatively cheap, corrosion resistant and a good electrical conductor. Thick nickel films with an approximate 0.2 to 0.4 $\mu$m are used and the additional surface weight added by this coating is between 20 and 200 g/m$^2$ [44]. These protections were primarily applied for electromagnetic shielding rather than lightning protection. Generally, this method is applied only to the upper ply of a CFRP laminate in order to decrease the overall additional weight. This upper ply should be able to withstand the lightning strike and to conduct the lightning strike current. However, the efficiency of this lightning protection is lower than that of Expanded Copper Foil (ECF), which remains the most used lightning protection.

**Epoxy resins reinforced with carbon allotropes** - This method consists of nanoparticle reinforcement of composite materials to increase their mechanical, electrical, and thermal properties. In aerospace applications, carbon nanotubes are used due to their superior properties for multifunctional applications. The most commonly used carbon fibres offer a sufficiently high electrical and a reasonable thermal conductivity, but the epoxy matrix which surrounds them is an excellent electrical isolator. Thus, the objective is to improve the matrix properties and possibly to network the carbon fibres both within and between the adjacent plies. Studies have shown that the incorporation of carbon nanotubes or short carbon fibres can significantly enhance the electrical conductivity of the resin matrix reducing significantly the damage of unprotected CFRP laminates [44]. However, this lightning protection method is still insufficient for airframe CFRP laminates.

Another nanoparticle reinforcement is graphene and there has been a growing interest and study on graphene-reinforced polymers. Graphene is a single layer graphite sheet that consists of sp$^2$ carbon atoms covalently bonded in an honeycomb crystal lattice. The addition of small quantities of graphene materials can simultaneously provide significant improvements in strength, toughness, electrical and thermal conductivity, and chemical inertness to a number of polymers. Graphene platelets have emerged as very promising nano-fillers in multifunctional composites, even more promising than single or multi-wall carbon nanotube structures. Studies have shown that the incorporation of graphene platelets can significantly enhance the mechanical, thermal, and electrical properties of polymers and CFRP laminates but for lightning protection applications as a stand-alone system far from being sufficient [44].

The presence of a protection such as ECF allows to reduce significantly the damage due to lightning strike on composite structures. The extent of damage between a protected and an unprotected sample is different both at the surface (near the impact point) and in the depth of the material. However, these protections are not optimized and represent an additive weight on the composite structures which were preferred to metal because of their lightweight. Moreover, lightning tests in laboratory are expensive and do not allow to extract a lot of information. In order to evaluate these protections and to improve the common knowledge of lightning interaction, other means must be used. One of these means is the numerical simulation which facilitates the test of various configurations in a short period of time.

## 2.2 Failure mechanisms

The modes of failure of composite materials are more complicated than isotropic materials. Not only the behaviour of a composite material is characterized by elastic with transversely isotropic symmetry, which has 5 independent material constants, but also the tensile and compressive strengths along the fibres and in the transverse direction. Also, the shear strength is independent. Failure criteria are needed to characterize an envelope which defines the strength of a transversely isotropic ply under a state of combined stresses or strains. These envelopes have to pass through the measured strengths (measured from experimental characterization) and must be closed, so that they do not imply infinite strengths under certain combined stresses. Each of the basic strength material properties correspond to a unique failure mode, consequently, composite materials are characterized by 5 basic failure modes.

1. Longitudinal tension – when a unidirectional ply is loaded in tension in the direction along the fibres, the phase with lower ultimate strain will fail, typically the fibre. Fibre strength changes from point to point and from fibre to fibre, being governed by a statistical distribution, which means that failure starts in localized regions of individual fibres, Figure 2.16. The fibres usually do not fail all at the same time, the rupture starting at the weakest points and spreading through the material, resulting in a non-uniform stress state around the fibre breaks.

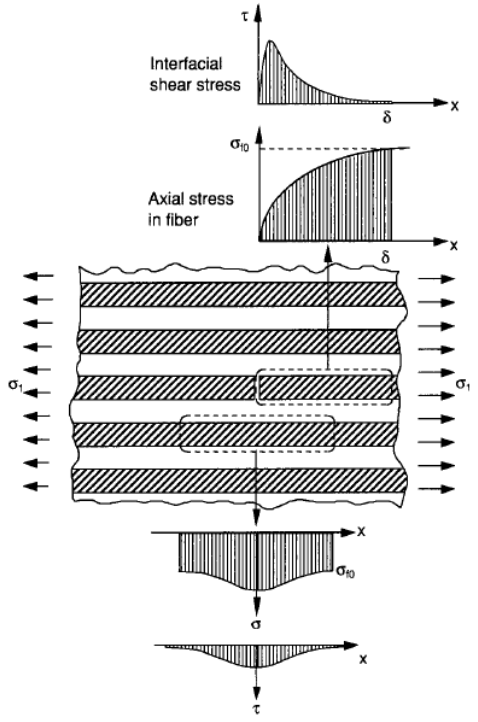



**Figure 2.16:** Local stress distributions around a fiber break in a unidirectional composite under longitudinal tension [46].

   When individual fibres fail under tension the internal loads must redistribute to other areas of the structure. Therefore, localized fractures increase the normal shear stresses in the adjoining fibres, these local stress concentrations promote matrix cracking and fibre matrix debonding. Increasing the load further results in aditional fibre fracture leading to final rupture.

2. Longitudinal compression – shear-type failure which occurs from the collapse of the fibres as

a result of shear kinking and damage of the supporting matrix, Figure 2.17. Fibre kinking appears as a shear deformation leading to the formation of a kink band, Figure 2.18. The analysis of the kinking phenomena is usually based on the assumption of a local initial fibre misalignment. Fibre misalignment leads to shear stresses that rotate the fibres, increasing the shearing stresses and leading to instability [47].

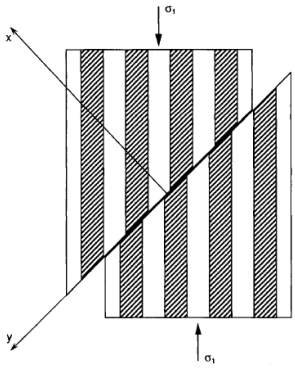
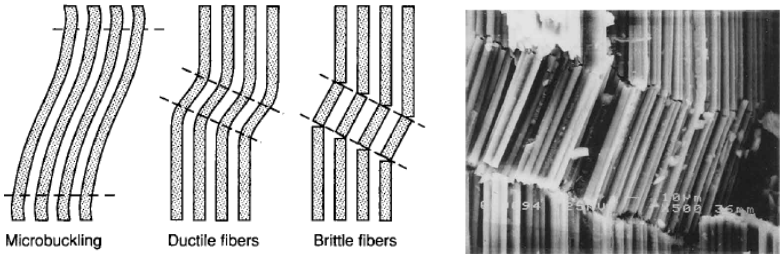



**Figure 2.17:** Shear failure mode of a unidirectional composite under longitudinal compression [46].




a b

**Figure 2.18:** a) Formation of kinking zones due to microbuckling and b) kink band in unidirectional carbon/epoxy composite under longitudinal compressive loading [46].

3. Transverse tension – results in high stress and strain concentrations in the matrix and fibre-matrix interface, leading to a cleavage type of failure along the fibres, Figure 2.19. The failure is caused by a crack opening mode in the form of isolated interfacial microcracks. Under the presence of transverse tensile stresses and in-plane shear stresses, the combined effect of small defects present in a ply, such as small fibre-resin debonds, resin-rich regions, and resin voids, trigger a transverse crack that extends through the thickness of the ply. The transverse cracks are formed without disturbing the fibres: they occur at the fibre–matrix interface and in the matrix. Cracks increase in number with increasing load and finally coalescing into a catastrophic crack transverse to the direction of the applied stress.

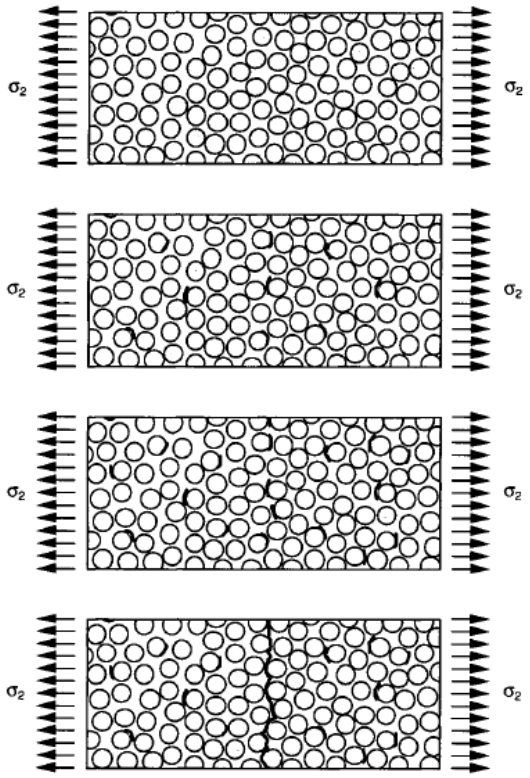
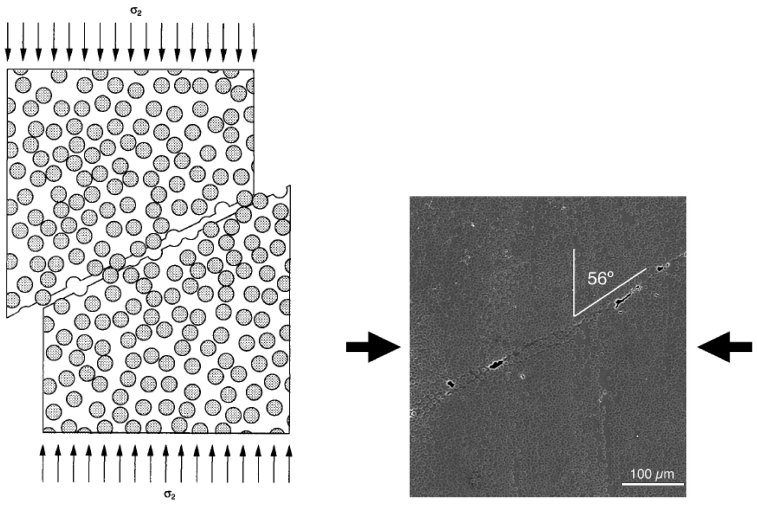



**Figure 2.19:** Progressive microcracking leading to ultimate failure in a unidirectional composite under transverse tension [46].

4. Transverse compression - under transverse compression, high interfacial shear stresses cause matrix shear failure and fibre-matrix debonding, leading to an overall shear failure mode characterised by a wedge shaped transverse fracture, Figure 2.20a. The increase of the compressive transverse stress causes a change in the angle of the fracture plane. For carbon-epoxy and glass-epoxy composites loaded in pure transverse compression, the fracture plane is typically at an angle of $53° \pm 3°$, Figure 2.20b, with respect to the thickness direction [48].




a b

**Figure 2.20:** a) Shear failure mode under transverse compression [46] and b) fracture plane [49].

5. In-plane shear – similar to transverse tension, a high shear stress concentration develops at the fibre-matrix interface, causing shear failure in the matrix and/or fibre-matrix debonding,

Figure 2.21.

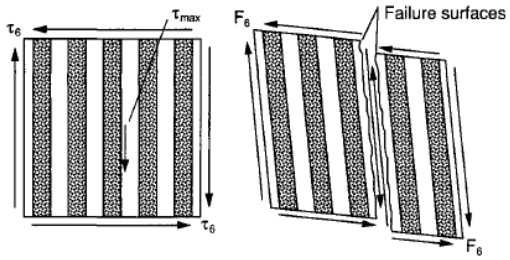



**Figure 2.21:** Failure mode of unidirectional composite under in-plane shear [46].

Advanced phenomenological failure criteria can model distinct failure modes, dividing the ply failure mechanisms between longitudinal failure mechanisms, in which failure occurs both in the fibres and matrix, and transverse failure mechanisms, which include matrix and fibre-matrix interface cracking.

## 2.3 LaRC03 Criteria

The LaRC03 criteria [47] is a set of four phenomenological failure criteria for fibre-reinforced polymer laminates to predict matrix and fibre failure. The criteria are divided between matrix failure and fibre failure, tension and compression for each case. Matrix failure relates to transverse failure mechanisms while fibre failure relates to longitudinal failure mechanisms. The failure indexes for a given failure mode are written as an equality stating that the stress sates which violate the inequality are not physically admissible.

### 2.3.1 Transverse compression failure ($\sigma_{22} < 0$)

The fracture plane can be subjected to transverse as well as in-plane stresses, in which case the effective stresses must be defined in both orthogonal directions:

$$\tau_{eff}^{T} = \left(\left|\tau^{T}\right| + \eta_{T}\sigma_{n}\right) \tag{2.1}$$

$$\tau_{eff}^{L} = \left(\left|\tau^{L}\right| + \eta_{L}\sigma_{n}\right) \tag{2.2}$$

The stress components acting on the fracture plane can be expressed in terms of the in-plane stresses and the angle of the fracture plane, $\alpha$, Figure 2.22:

$$\sigma_{n} = \sigma_{22} \cdot \cos^{2}(\alpha) \tag{2.3}$$

$$\tau^{T} = -\sigma_{22} \cdot \sin(\alpha)\cos(\alpha) \tag{2.4}$$

$$\tau^{L} = \sigma_{12} \cdot \cos(\alpha) \tag{2.5}$$

Combining the previous equations, the effective stresses for an angle of the fracture plane $\alpha$ between 0° and 90° are:

$$\tau_{eff}^{T} = [-\sigma_{22}\cos(\alpha)(\sin(\alpha) - \eta^{T}\cos(\alpha))] \tag{2.6}$$

$$\tau_{eff}^{L} = [\cos(\alpha)(\sigma_{12} + \eta^{L}\sigma_{22}\cos(\alpha))] \tag{2.7}$$

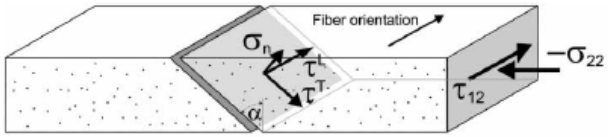



**Figure 2.22:** Fracture of a unidirectional lamina subjected to transverse compression and in-plane shear [47].

The criterion for matrix failure under transverse compression assumes a quadratic interaction between the effective shear stresses acting on the fracture plane:

$$FI_M = \left(\frac{\tau_{eff}^T}{S^T}\right)^2 + \left(\frac{\tau_{eff}^L}{S_{is}^L}\right)^2 \leqslant 1 \tag{2.8}$$

The subscript M designates matrix failure and $S_L$ and $S_T$ are, respectively, the longitudinal and transverse shear strengths. The subscript "is" in $S_{is}^L$ refers to the *in situ* longitudinal shear strength which should be used for general laminates, instead of the strength of a unidirectional laminate. In a general laminate the constraining effect of adjacent plies increases the effective strength of a ply. The coefficients of longitudinal and transverse influence, $\eta_L$ and $\eta_T$, are calculated from the case of uniaxial transverse compression ($\sigma_{22} < 0$ and $\tau_{12} = 0$). When failure is achieved, the in-plane compressive stress is equal to the matrix compressive strength, $\sigma_{22} = -Y^C$:

$$\eta_T = \frac{-1}{\tan(2\alpha_0)} \tag{2.9}$$

$\eta_L$ is estimated from the longitudinal and transverse shear strengths, as proposed by Puck:

$$\frac{\eta^L}{S^L} = \frac{\eta^T}{S^T} \Rightarrow \eta_L = \frac{s^L \cos(2\alpha_0)}{Y^C \cos^2(\alpha_0)} \tag{2.10}$$

The transverse shear strength $S^T$ can be calculated as:

$$S^T = Y^C \cos(\alpha_0)\left(\sin(\alpha_0) + \frac{\cos(\alpha_0)}{\tan(2\alpha_0)}\right) \tag{2.11}$$

The angle of fracture plane is the one which maximizes the failure index (2.8), by searching the fracture angle within a loop of possible fracture angles $0 < \alpha < \alpha_0$.

### 2.3.2 Transverse tension failure ($\sigma_{22} > 0$)

The failure criterion for transverse failure for predicting cracking in a ply under in-plane shear load and transverse tension is based on the fracture mechanics analysis of a crack in a ply.

The failure index for matrix tension is expressed in terms of the ply stresses and *in situ* strengths $Y_{is}^T$ and $S_{is}^L$:

$$FI_M = (1-g)\frac{\sigma_{22}}{Y_{is}^T} + g\left(\frac{\sigma_{22}}{Y_{is}^T}\right)^2 + \left(\frac{\sigma_{12}}{S_{is}^L}\right)^2 \leqslant 1 \tag{2.12}$$

In order to predict accurately matrix cracking of a laminate which is subjected to transverse stresses and in-plane shear, the failure criteria must be able to calculate the *in situ* strengths.

Firstly described in [50], the *in situ* effect, in the case of a ply being constrained by other plies with other fibre orientations, leads to higher transverse and shear strengths of a ply, when compared with the strengths of a similar ply in a unidirectional laminate. Therefore, this effect depends on the fibre orientation and ply thickness. For example, Figure 2.23 shows that thinner plies exhibit higher transverse tensile strengths.

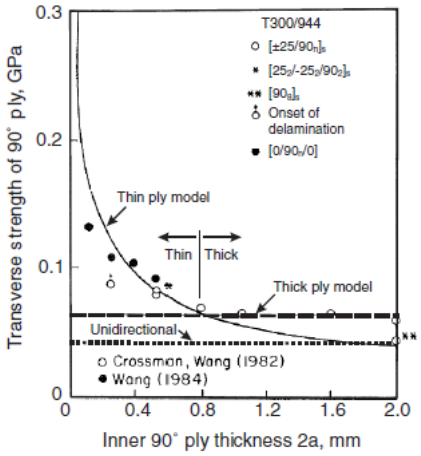



**Figure 2.23:** Transverse tensile strength as a function of the number of plies clustered together [47].

The thickness of the plies is defined by the length of the slit crack. For a thick ply the slit crack is much smaller than its thickness, $2a_0 \ll t$, whereas a thin ply is characterized for having a smaller thickness than the imposed defect, $t < 2a_0$. The minimum thickness of a thick ply is dependent on the material.

For thick plies the crack can grow in the transverse and longitudinal directions, with the crack energy release rate twice as greater in the transverse direction as in the longitudinal direction [47]. In thin plies the slit crack can only grow in the longitudinal direction. Consequently, the *in situ* strengths are calculated differently regarding each case.

The *in situ* shear strengths can be obtained by the general expression [51]:

$$S_{is}^{L} = \sqrt{\frac{(1+\beta\phi G_{12}^{2})^{1/2}-1}{3\beta G_{12}}} \tag{2.13}$$

where the parameter $\phi$ is defined accordingly to the configuration of a given ply.

**Thin ply**:

$$Y_{is}^{T} = \sqrt{\frac{8G_{Ic}(L)}{\pi t \Lambda_{22}^{0}}} \tag{2.14}$$

Thin inner ply [51]:

$$\phi = \frac{24G_{IIC}}{\pi t} \tag{2.15}$$

Thin outer ply [51]:

$$\phi = \frac{48G_{IIC}}{\pi t} \tag{2.16}$$

$$g = \frac{G_{Ic}}{G_{IIc}} \tag{2.17}$$

The toughnesses $G_{Ic}(L)$ and $G_{IIc}(L)$ can be assumed to be the values determined by standard Fracture Mechanics tests, such as the double cantilever beam test (DCB) for Mode I and the end-notch flexure test (ENF) for Mode II [47].

**Thick ply**:

$$Y_{is}^T = 1.12\sqrt{2}Y^T \tag{2.18}$$

$$\phi = \frac{12(S^L)^2}{G_{12}} + \frac{72}{4}\beta(S^L)^4 \tag{2.19}$$

$$g = 1.12^2 \frac{\Lambda_{22}^0}{\Lambda_{44}^0}\left(\frac{Y^T}{S^L}\right)^2 \tag{2.20}$$

$Y^T$ and $S^L$ are the material tensile and shear strengths measured in unidirectional laminate tests.

$$\Lambda_{22}^0 = 2\left(\frac{1}{E_2} - \frac{\nu_{21}^2}{E_1}\right) \tag{2.21}$$

$$\Lambda_{44}^0 = \frac{1}{G_{12}} \tag{2.22}$$

Applying $g = 1$ to equation (2.12), it reverts to the very well-known Hashin criterion for transverse matrix cracking under both in-plane shear and transverse tension, with ply strengths replaced by the *in situ* strengths [47]:

$$FI_M = \left(\frac{\sigma_{22}}{Y_{is}^T}\right)^2 + \left(\frac{\sigma_{12}}{S_{is}^L}\right)^2 \leqslant 1 \tag{2.23}$$

### 2.3.3 Longitudinal tensile fibre failure

This mechanism of failure is determined by the phase with lower allowable strain, normally the fibre, therefore the criteria for longitudinal tensile fibre failure is based on a non-interacting maximum allowable strain criterion. Puck and Shurman [48, 52] recommended, based on experiments, that the criteria should be based on the 'effective strain' acting on the fibres [47].

$$FI_F = \frac{\varepsilon_{11}}{\varepsilon_1^T} \leqslant 1 \tag{2.24}$$

### 2.3.4 Longitudinal compression fibre failure

This mechanism of failure results from a shear kinking damage of the supporting matrix which misaligns the fibres and leads to the formation of a kink band. The fibre misalignment originates shear stresses which rotate the fibres, increasing the shearing stresses and leading to instability [47]. This analysis is based on the assumption of a local initial fibre misalignment [53].

The failure by fibre compression is predicted using the stresses in the misalignment coordinate presented in Figure 2.24:

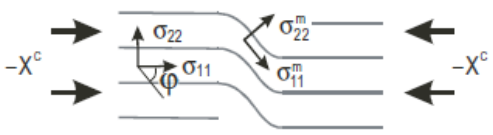



**Figure 2.24:** Imperfection in fibre alignment idealized as a local waviness [47]

$$\sigma_{11}^m = \cos^2\varphi\sigma_{11} + \sin^2\varphi\sigma_{22} + 2\sin\varphi\cos\varphi|\sigma_{12}| \tag{2.25}$$

$$\sigma_{22}^m = \sin^2\varphi\sigma_{11} + \cos^2\varphi\sigma_{22} + 2\sin\varphi\cos\varphi|\tau_{12}| \tag{2.26}$$

$$\sigma_{12}^m = -\sin\varphi\cos\varphi\sigma_{11} + \sin\varphi\cos\varphi\sigma_{22} + (\cos^2\varphi - \sin^2\varphi)|\sigma_{12}| \tag{2.27}$$

Where $\varphi$ is the fibre misalignment angle. Applying the stresses from equations (2.25) to (2.27), to the failure criterion for transverse failure in matrix tension and matrix compression gives the respective failure criteria. Therefore, for matrix compression ($\sigma_{22} > 0$) the failure criterion is:

$$FI_F = \left\langle \frac{|\sigma_{12}^m| + \eta_L\sigma_{22}^m}{S_{is}^L} \right\rangle \leqslant 1 \tag{2.28}$$

Introducing the transformed stresses of equations (2.25) to (2.27) into the failure criterion for transverse tension, equation (2.12) gives the failure criterion for fibre compression with matrix tension,

$$FI_M = (1-g)\left(\frac{\sigma_{22}^m}{Y_{is}^T}\right) + g\left(\frac{\sigma_{22}^m}{Y_{is}^T}\right)^2 + \left(\frac{\sigma_{12}^m}{S_{is}^L}\right)^2 \leqslant 1 \tag{2.29}$$

The total misalignment angle can be decomposed into two portions, $\varphi = \varphi^0 + \varphi^R$, the initial misalignment, $\varphi^0$, resulting from a manufacturing imperfection, and the rotational angle imposed by the shear stresses, $\varphi^R$.

$$\varphi = \frac{|\tau_{12}| + (G_{12} - X^C)\varphi^C}{G_{12} + \sigma_{11} - \sigma_{22}} \tag{2.30}$$

$$\varphi^C = \tan^{-1}\left(\frac{1 - \sqrt{1 - 4(S_{is}^L/X^C + \eta_L)(S_{is}^L/X^C)}}{2(S_{is}^L/X^C + \eta_L)}\right) \tag{2.31}$$

$\varphi_C$ is the misalignment angle for pure longitudinal compressive failure.

When the loading case is matrix biaxial compression where there is high transverse compression combined with moderate fibre compression, matrix failure can occur without damage to the fibres or formation of a kink band. In this case matrix damage can be evaluated by applying the stresses in the misalignment frame to the failure criterion for transverse compression failure, resulting in:

$$FI_M = \left(\frac{\tau_{eff}^{mT}}{S^T}\right)^2 + \left(\frac{\tau_{eff}^{mL}}{S_{is}^L}\right)^2 \leqslant 1 \tag{2.32}$$

## 2.4 Three-dimensional failure criteria for fibre-reinforced laminates

Catalanotti et al. in [54] proposed a 3D version of the previous criteria. Defining $\alpha$ as the angle between the fracture plane and the through-thickness direction, Figure 2.25, the failure index will be dependent on the tractions acting on the fracture surface and on the angle $\alpha$.

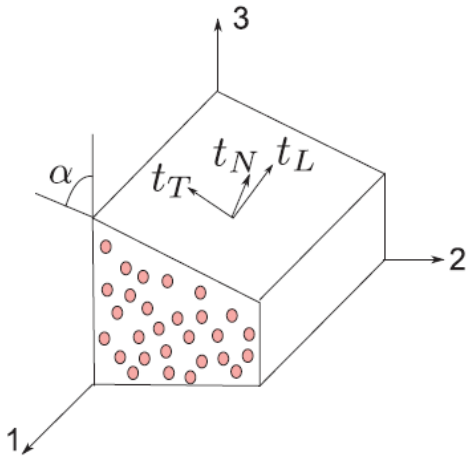



**Figure 2.25:** Components of the traction vector on the fracture plane [54].

Defining the unit normal vector to the fracture plane as:

$$n_1 = [\ 1 \quad 0 \quad 0\ ]^T \tag{2.33}$$

$$n_2 = [\ 0 \quad \cos(\alpha) \quad \sin(\alpha)\ ]^T \tag{2.34}$$

the traction acting on the fracture plane, $t$ is:

$$t = \sigma \cdot n_2 \tag{2.35}$$

where $\sigma$ is the stress tensor. The orientation of the fracture plane is function of the components of the traction vector that maximizes the failure index for a particular value of $\alpha$. Figure 2.25 represents these components, the normal stress and the two shear stresses (longitudinal and transverse):

$$t_N = t \cdot n_2 \tag{2.36}$$

$$t_L = t \cdot n_1 \tag{2.37}$$

$$t_T = t \cdot (n_1 \times n_2) \tag{2.38}$$

The failure criteria depends on the sign of the normal stress, either matrix compression for $t_N < 0$ or matrix tension for $t_N > 0$.

### 2.4.1 Transverse compression failure

The failure index for transverse compression is based on the Puck's criterion, modified in order to take into account the *in situ* effect, i.e., the increase of the shear strength of a ply when embedded in a multidirectional laminate:

$$\phi_{MC} = \left(\frac{t_L}{S_L^{is} - \eta_L t_N}\right)^2 + \left(\frac{t_T}{S_T^{is} - \eta_T t_N}\right)^2 \tag{2.39}$$

$S_L^{is}$ is the *in situ* longitudinal shear strength, $S_T^{is}$ is the *in situ* transverse shear strength and $\eta_L$ and $\eta_T$ are friction coefficients which correspond to the two slopes in the diagram $t_N - \tau$ when $t_N = 0$:

$$\eta_L = -\frac{\partial t_L}{\partial t_N}\Big|_{t_N=0} \tag{2.40}$$

$$\eta_N = -\frac{\partial t_T}{\partial t_N}\Big|_{t_N=0} \tag{2.41}$$

With the relationship between the friction coefficients proposed by Puck and Shurmann [52]:

$$\frac{\eta_L}{\eta_T} = \frac{S_L^{is}}{S_T^{is}} \tag{2.42}$$

The *in situ* strengths can be determined as:

$$Y_C^{is} = -\frac{S_L^{is}(2\cos^2(\alpha_0) - 1)}{\eta_L \cos^2(\alpha_0)} \tag{2.43}$$

$$S_T^{is} = \frac{1}{2}\frac{(2\sin^2(\alpha_0) - 1)S_L^{is}}{\sqrt{1 - \sin^2(\alpha_0)} \cdot \sin(\alpha_0)\eta_L} \tag{2.44}$$

### 2.4.2 Transverse tension failure

When transverse tension is applied ($\sigma_{22}$ or $\sigma_{33}$) there is a combination of $t_N$ and $t_T$ on the generic fracture plane and the fracture angle $\alpha \neq 0$ will be a function of $Y_T^{is}$ and $S_T^{is}$, and therefore it depends on the material system:

$$\phi_{MT} = \left(\frac{t_N}{S_T^{is}}\right)^2 + \left(\frac{t_L}{S_L^{is}}\right)^2 + \left(\frac{t_T}{S_T^{is}}\right)^2 + \lambda\left(\frac{t_N}{S_T^{is}}\right)\left(\frac{t_L}{S_L^{is}}\right)^2 + \kappa\left(\frac{t_N}{S_T^{is}}\right) \tag{2.45}$$

$t_N$, $t_L$ and $t_T$ were previously defined. The parameter $\kappa$ is obtained by imposing $\phi_{MT} = 1$ when $t_N = Y_T^{is}$:

$$\kappa = \frac{{S_T^{is}}^2 - {Y_T^{is}}^2}{S_T^{is} Y_T^{is}} \tag{2.46}$$

The parameter $\lambda$ is determined by:

$$\lambda = 2\eta_L \frac{S_T^{is}}{S_L^{is}} - \kappa \tag{2.47}$$

### 2.4.3 Longitudinal tension fibre failure ($\sigma_{11} > 0$)

As before, the function that predicts longitudinal tensile fracture is the maximum strain criterion:

$$\phi_{LT} = \frac{\varepsilon_{11}}{\varepsilon_1^T} \tag{2.48}$$

### 2.4.4 Longitudinal compression fibre failure ($\sigma_{11} < 0$)

The kinking failure mode is influenced by three dimensional stress states. Argon [53] hypothesis assumes a local initial fibre misalignment, and kink bands are triggered by localized matrix failure in the vicinity of misaligned fibres.

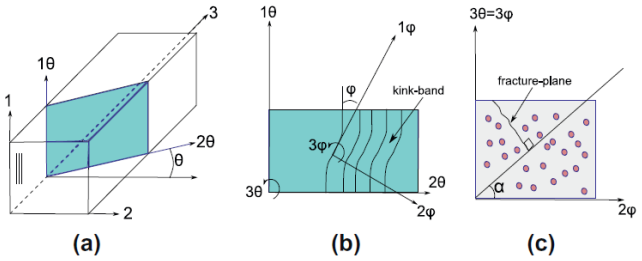



**Figure 2.26:** Coordinate systems associated to fibre kinking [54].

Figure 2.26 features the coordinate systems and planes used in the model. The coordinate system 123 is aligned with the axes of the composite, where 1 represents the fibre direction, 2 and 3 the transverse directions.

The kinking plane is represented in Figure 2.26a, and its associated coordinate system, $1^\theta 2^\theta 3^\theta$, is obtained by the rotation of the frame 123 around the axis 1 of an angle $\theta$, angle of the kinking plane.

Figure 2.26b shows the fibres on the kinking plane, and the kinking angle $\varphi$. The coordinate system $1^\varphi 2^\varphi 3^\varphi$ is originated from $1^\theta 2^\theta 3^\theta$ by a rotation of $\varphi$ around the axis $3^\theta$. After this transformation it is possible to use the failure criteria (2.39) and (2.45) in the misalignment coordinate system to predict fibre kinking.

Figure 2.26c shows the representation of the fracture angle with respect to the misalignment frame, identified by $\alpha$. Kinking failure can now be predicted employing the matrix failure index in the misalignment frame, which requires two rotations of the stress tensor. The angle $\theta$ is assumed to be a function of the stress field and the kinking plane is defined by the shear stresses that act on the plane 2-3, Figure 2.27, therefore $\theta$ can be calculated as:

$$\theta = \arctan\left(\frac{\sigma_{13}}{\sigma_{12}}\right) \tag{2.49}$$

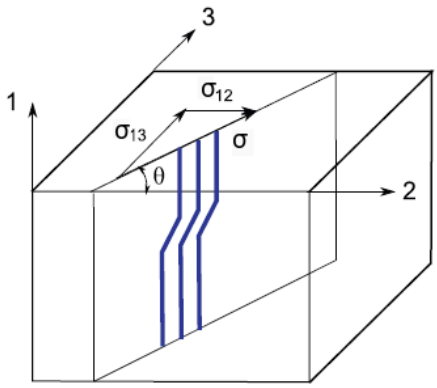



**Figure 2.27:** Kinking plane and involved shear stresses [54]

If the shear stresses $\sigma_{13}$ and $\sigma_{12}$ are both equal to zero then the kinking angle can be calculated by the maximum principal stress acting on the transversely isotropic plane. Following Pinho et al. [55], if the shear stress in the kinking plane $\sigma_{23}^{(\theta)} \neq 0$, an out-of plane movement of the kinked fibres will occur, which contradicts the evidence that fibres kink on this plane. Therefore the angle $\theta$ can be obtained by imposing $\sigma_{23} = 0$ and knowing the stress tensor in the kinking plane $\sigma^{(\theta)}$:

$$\theta = \frac{1}{2}\arctan\left(\frac{2\sigma_{23}}{\sigma_{22} - \sigma_{33}}\right) \tag{2.50}$$

Applying a rotation of $\theta$ (counterclockwise) to the stress tensor, results in:

$$\sigma^{(\theta)} = \mathrm{T}_{0\theta} \cdot \sigma \cdot {\mathrm{T}_{0\theta}}^{T} \tag{2.51}$$

where $T_{0\theta}$ is the rotation matrix between the material coordinate system and the kinking plane:

$$\mathrm{T}_{0\theta} = \begin{bmatrix} 1 & 0 & 0 \\ 0 & \cos(\theta) & \sin(\theta) \\ 0 & \text{-}\sin(\theta) & \cos(\theta) \end{bmatrix} \tag{2.52}$$

Stresses in the misalignment plane are defined with a rotation $\varphi$, resulting in the new coordinate system:

$$\sigma^{(\varphi)} = \mathrm{T}_{\theta\varphi} \cdot \sigma^{(\theta)} \cdot {\mathrm{T}_{\theta\varphi}}^{\mathrm{T}} \tag{2.53}$$

and $\mathrm{T}_{\theta\varphi}$ is the matrix rotation.

$$\mathrm{T}_{\theta\varphi} = \begin{bmatrix} \cos(\varphi) & \sin(\varphi) & 0 \\ \text{-}\sin(\varphi) & \cos(\varphi) & 0 \\ 0 & 0 & 1 \end{bmatrix} \tag{2.54}$$

The tensile components on the fracture plane can be expressed by:

$$t_N^{(\varphi)} = \cos^2(\alpha)\sigma_{22}^{(\varphi)} + 2\cos(\alpha)\sin(\alpha)\sigma_{23}^{(\varphi)} + \sin^2(\alpha)\sigma_{33}^{(\varphi)} \tag{2.55}$$

$$t_T^{(\varphi)} = -\sin(\alpha)\cos(\alpha)(\sigma_{22}^{(\varphi)} - \sigma_{33}^{(\varphi)}) + (\cos^2(\alpha) - \sin^2(\alpha))\sigma_{23}^{(\varphi)} \tag{2.56}$$

$$t_L^{(\varphi)} = \cos(\alpha)\sigma_{12}^{(\varphi)} + \sin(\alpha)\sigma_{13}^{(\varphi)} \tag{2.57}$$

if $t_N^{(\phi)} < 0$ the failure index is:

$$\phi_{KMC} = \left(\frac{t_L^{(\varphi)}}{S_L^{is} - \eta_L t_N^{(\varphi)}}\right)^2 + \left(\frac{t_T^{(\varphi)}}{S_T^{is} - \eta_T t_N^{(\varphi)}}\right)^2 \tag{2.58}$$

whereas if $t_N^{(\phi)} \geqslant 0$ the failure index becomes:

$$\phi_{KMT} = \left(\frac{t_N^{(\varphi)}}{S_T^{is}}\right)^2 + \left(\frac{t_L^{(\varphi)}}{S_L^{is}}\right)^2 + \left(\frac{t_T^{(\varphi)}}{S_T^{is}}\right)^2 + \lambda\left(\frac{t_N^{(\varphi)}}{S_T^{is}}\right)\left(\frac{t_L^{(\varphi)}}{S_L^{is}}\right)^2 + \kappa\left(\frac{t_N^{(\varphi)}}{S_T^{is}}\right) \tag{2.59}$$

The failure index for fibre kinking will take the value:

$$\phi_\kappa = \max\{\max\{\phi_{KMC}\}, \max\{\phi_{KMT}\}\} \tag{2.60}$$

The kinking angle $\varphi$, is determined by:

$$\varphi = \operatorname{sgn}\{\sigma_{12}\}(\varphi_0 + \gamma_m) \tag{2.61}$$

$\varphi_0$ is the initial misalignment angle and $\gamma_m$ is the angle originated by the shear loading applied and depends on the shear constitutive law $\tau = f(\gamma_m)$. The initial misalignment $\phi_0$ can be analysed as a representation of local micro-structural defects from manufacture, or of the intrinsic fibre volume fraction oscillations in the material and can be calculated taking the particular case of the material under pure longitudinal compression $\sigma_{11} = -X_C$ and all other components of the stress tensor equal to zero ($X_C$ is the longitudinal compressive strength):

$$\varphi_0 = \varphi_C - \gamma_{mC} \tag{2.62}$$

$$\gamma_m = \frac{\varphi_0 G_{12} + \left|\sigma_{12}^{(\theta)}\right|}{G_{12} + \sigma_{11}^{(\theta)} - \sigma_{22}^{(\theta)}} \tag{2.63}$$

$\varphi_C$ is the angle at failure when a pure axial compression is applied:

$$\varphi_C = \arctan\left(\frac{1 - \sqrt{1 - 4\left(\frac{S_L is}{X_C} + \eta_L\right)\frac{S_L is}{X_C}}}{2\left(\frac{S_L^(\, is)}{X_C} + \eta_L\right)}\right) \tag{2.64}$$

$\gamma_{mC}$ is the angle $\gamma_m$ at failure under axial compression, and for a material that exhibits linear behaviour in shear:

$$\gamma_{mC} = \frac{\sin(2\varphi_C)X_C}{2G_{12}} \approx \frac{\varphi_C X_C}{G_{12}} \tag{2.65}$$

## 2.5 Three-dimensional invariant-based failure criteria for fibre-reinforced composites

The 3D failure criteria proposed in [56] has an invariant quadratic formulation based on structural tensors, accounting for the preferred directions of the anisotropic material. Anisotropy is derived by structural tensors, represented as an intrinsic material property. Therefore, the anisotropic constitutive equations are represented as isotropic tensor functions and description of anisotropy is independent of coordinate system. As in the previous criteria, these predict failure in a single unidirectional (UD) ply, and therefore it is required that the strains and stresses of each ply on a multidirectional laminate are determined. These criteria, like most of the other phenomenological criteria, present independent conditions for each failure mechanism. The transverse and longitudinal failure mechanisms are derived from different criteria.

### 2.5.1 Invariant-based criteria for transverse failure

The criteria for transverse failure mechanisms is based directly on the invariant theory. The transverse failure criteria proposed by the 3D invariant-based criterion is formulated directly from the yield function presented in [57]. Transversely isotropic materials can be characterized by a preferred direction $\mathbf{a}$, which for unidirectional ply is the fibre direction. In general case the fibre direction coincides with the 1 direction. In such case, the direction $\mathbf{a}$ is represented as:

$$\mathbf{a} = [\ 1 \quad 0 \quad 0\ ]^T \tag{2.66}$$

The structural tensor $\mathbf{A}$ of transverse isotropy is defined as the dyadic product of the preferred direction $\mathbf{a}$:

$$\mathbf{A} = \mathbf{a} \otimes \mathbf{a} \tag{2.67}$$

The functional basis for transverse isotropy is formed by the argument tensors $\boldsymbol{\sigma}$ and $\mathbf{A}$:

$$\mathrm{tr}\boldsymbol{\sigma}, \quad \mathrm{tr}\boldsymbol{\sigma}^2, \quad \mathrm{tr}\boldsymbol{\sigma}^3, \quad \mathrm{tr}(\mathbf{A}\boldsymbol{\sigma}) \quad \text{and} \quad \mathrm{tr}(\mathbf{A}\boldsymbol{\sigma}^2) \tag{2.68}$$

The quadratic invariants $\mathrm{tr}\boldsymbol{\sigma}^2$ and $\mathrm{tr}(\mathbf{A}\boldsymbol{\sigma}^2)$ of the functional basis (2.68) are derived considering a decomposition of the stress tensor $\boldsymbol{\sigma}$ in reaction stresses $\boldsymbol{\sigma}^r$ and plasticity inducing stresses $\boldsymbol{\sigma}^p$:

$$\boldsymbol{\sigma} = \boldsymbol{\sigma}^p + \boldsymbol{\sigma}^r \tag{2.69}$$

and:

$$\boldsymbol{\sigma}^r = \frac{1}{2}(\mathrm{tr}\boldsymbol{\sigma} - \mathbf{a}\boldsymbol{\sigma}\mathbf{a})\mathbf{I} - \frac{1}{2}(\mathrm{tr}\boldsymbol{\sigma} - 3\mathbf{a}\boldsymbol{\sigma}\mathbf{a})\mathbf{A} \tag{2.70}$$

$$\boldsymbol{\sigma}^p = \boldsymbol{\sigma} - \boldsymbol{\sigma}^r \tag{2.71}$$

The set of transversely isotropic invariants used to formulate the yield surface is [56]:

$$I_1 = \frac{1}{2}\mathrm{tr}(\boldsymbol{\sigma}^p)^2 - \mathbf{a}(\boldsymbol{\sigma}^p)^2\mathbf{a} \tag{2.72}$$

$$I_2 = \mathbf{a}(\boldsymbol{\sigma}^p)^2\mathbf{a} \tag{2.73}$$

$$I_3 = \mathrm{tr}\boldsymbol{\sigma} - \mathbf{a}\boldsymbol{\sigma}\mathbf{a} \tag{2.74}$$

Replacing equations (2.69) to (2.71) the invariants become:

$$I_1 = \frac{1}{4}\sigma_{22}^2 - \frac{1}{2}\sigma_{22}\sigma_{33} + \frac{1}{4}\sigma_{33}^2 + \sigma_{23}^2 \tag{2.75}$$

$$I_2 = \sigma_{12}^2 + \sigma_{13}^2 \tag{2.76}$$

$$I_3 = \sigma_{22} + \sigma_{33} \tag{2.77}$$

The transversely isotropic failure criterion for transverse failure of UD fibre-reinforced laminates is:

$$f_M = \alpha_1 I_1 + \alpha_2 I_2 + \alpha_3 I_3 + \alpha_{32} I_3^2 \leqslant 1 \tag{2.78}$$

and:

$$\alpha_3 = \alpha_3^t, \quad \alpha_{32} = \alpha_{32}^t \qquad \text{if} \quad I_3 > 0 \quad \text{and} \quad \alpha_3 = \alpha_3^c, \quad \alpha_{32} = \alpha_{32}^c \qquad \text{if} \quad I_3 \leqslant 0 \tag{2.79}$$

The distinction between $I_3 > 0$ and $I_3 \leqslant 0$ makes it possible for this criterion to represent failure when the stress tensor corresponds to a biaxial stress state. From the failure criterion represented by the equation (2.78) six failure parameters emerge, related to their respective invariants. These parameters are related to certain load states: transverse shear, in-plane shear, uni-axial tension/compression and biaxial tension/compression. By imposing single stress states and applying the failure criteria these failures parameters can be obtained:

$$\alpha_1 = \frac{1}{S_T^2} \tag{2.80}$$

$$\alpha_2 = \frac{1}{S_L^2} \tag{2.81}$$

$$\alpha_{32}^t = \frac{1 - \frac{Y_T}{2Y_{BT}} - \alpha_1 \frac{Y_T^2}{4}}{Y_T^2 - 2Y_{BT}Y_T} \tag{2.82}$$

$$\alpha_3^t = \frac{1}{2Y_{BT}} - 2\alpha_{32}^t Y_{BT} \tag{2.83}$$

$$\alpha_{32}^c = \frac{1 - \frac{Y_C}{2Y_{BC}} - \alpha_1 \frac{Y_C^2}{4}}{Y_C^2 - 2Y_{BC}Y_C} \tag{2.84}$$

$$\alpha_3^c = \frac{1}{2Y_{BC}} - 2\alpha_{32}^c Y_{BC} \tag{2.85}$$

$S_T$ and $S_L$ are the transverse and in-plane shear strengths, respectively. $Y_T$ and $Y_L$ are the transverse tensile and compressive strengths, and $Y_{BT}$ and $Y_{BC}$ are the biaxial transverse tensile and compressive strengths.

## 2.5.2 Criteria for Longitudinal failure

The criteria for longitudinal failure mechanisms are formulated based on different considerations. For tensile fibre failure the criteria is formulated by means of a non-interacting maximum allowable strain criterion. Longitudinal compressive failure is predicted by a three dimensional kinking model based on the fracture model developed for the transverse failure mechanisms.

### 2.5.2.1 Longitudinal tension fibre failure ($\sigma_{11} \geqslant 0$)

Similar to the failure criteria previously presented, the longitudinal tensile fibre failure is predicted by a non-interacting maximum allowable strain criterion:

$$f_F = \frac{\varepsilon_{11}}{\varepsilon_1^T} \leqslant 1 \tag{2.86}$$

### 2.5.2.2 Longitudinal compression fibre failure ($\sigma_{11} < 0$)

As previously, these criteria also assume a local initial fibre misalignment to represent the local micro-structural defects which generate the shearing stresses between fibres leading to instability. The formulation of coordinate systems is similar to that of the previous criteria, therefore the same coordinate systems, Figure 2.26, and matrix transformations, (2.52) and (2.54), are assumed.

Kinking failure is predicted using the invariant-based formulation for transverse failure in the misalignment frame. The preferred direction is the fibre direction, $\mathbf{a}^{\varphi}$ which coincides with the direction of $1^{\varphi}$, Figure 2.26.

To express the preferred direction, $\mathbf{a}^{\varphi}$, in the material coordinate system 123, it is necessary to perform two successive transformations, as in section 2.4.4:

$$\mathbf{a} = \mathbf{T}_{\theta 0} \cdot \mathbf{a}^{\theta} = \mathbf{T}_{\theta 0} \cdot \mathbf{T}_{\varphi \theta} \cdot \mathbf{a}^{\varphi} \tag{2.87}$$

where $\mathbf{T}_{0\theta}$ and $\mathbf{T}_{\theta\varphi}$ are given in equations (2.52) and (2.54). Solving equation (2.87) gives the preferred direction in the material coordinate system as:

$$\mathbf{a} = \begin{bmatrix} \cos(\varphi) \\ \cos(\theta)\sin(\varphi) \\ \sin(\theta)\sin(\varphi) \end{bmatrix} \tag{2.88}$$

The angle of the kinking plane can be obtained by equations (2.49) and (2.50), again by the maximum principal stress which acts on the transversely isotropic plane.

For a pure longitudinal compression, therefore $\sigma_{11} = -X_C$, the invariants calculated in the misalignment plane take the form:

$$I_1 = \frac{1}{4}\sigma_{11}^2 \sin^4(\varphi) \tag{2.89}$$

$$I_2 = \sigma_{11}^2 \sin^2(\varphi)\cos^2(\varphi) \tag{2.90}$$

$$I_3 = \sigma_{11} \sin^2(\varphi) \tag{2.91}$$

therefore $I_3 < 0$ and the failure criterion reads:

$$f = \frac{1}{4}\alpha_1\sigma_{11}^2\sin^4(\varphi) + \alpha_2\sigma_{11}^2\sin^2(\varphi)\cos^2(\varphi) + \alpha_3^C\sigma_{11}\sin^2(\varphi) + \alpha_{32}^C\sigma_{12}^C\sin^4(\varphi) - 1 \tag{2.92}$$

The kinking angle, taking into account non-linear shear behaviour, is given by:

$$\varphi = \operatorname{sgn}\left\{\sigma_{12}^{\varphi}(\varphi_0,\theta)\right\}\left\{\varphi_0 + \left|\frac{\sigma_{12}^{\varphi}(\varphi_0,\theta)}{G_{12}} + \beta\left[\sigma_{12}^{\varphi}(\varphi_0,\theta)\right]^3\right|\right\} \tag{2.93}$$

where $\varphi_0$ is the initial misalignment, which and for small misalignment angles is:

$$\varphi_0 = \varphi_C\left(1 + \frac{|X_C|}{G_{12}}\right)^{-1} \tag{2.94}$$

with:

$$\varphi_C = \frac{1}{2}\arccos\left[\frac{4\sqrt{\alpha_1 - 4\alpha_2 + \alpha_2^C X_C^2 + (\alpha_3^C)^2 + 2\alpha_2\alpha_3^C X_C + 4\alpha_{32}^C} + (\alpha_1 + 4\alpha_{32}^C)X_C + 4\alpha_3^C}{(\alpha_1 - 4\alpha_2 + 4\alpha_{32}^C)X_C}\right] \tag{2.95}$$

and $\sigma_{12}^{\varphi}(\varphi_0,\theta)$ is the shear stress applied in the misalignment plane:

$$\sigma_{12}^{\varphi}(\varphi_0,\theta) = \frac{1}{2}\left[-\sigma_{11} + \sigma_{22}\cos^2\theta + \sigma_{33}\sin^2\theta + \sigma_{23}\sin 2\theta\right]\sin 2\varphi_0 + (\sigma_{12}\cos\theta + \sigma_{13}\sin\theta)\cos 2\varphi_0 \tag{2.96}$$

## 2.6 Numerical modelling of damage in composite materials

Employing composite materials into structural components needs a more evolved and complex process due to their exquisite damage behaviour. The design development programs need to ascertain the performance of the structure prior to the real application. The process of validating the structural performance and durability of composite materials requires, generally, a comprehensive combination of testing and analysis. Due to the possible variability of composite materials, which can be custom tailored for any application, the amount of testing necessary is prohibitively expensive and time consuming because of the number of specimens needed to verify every geometry, loading, environment, and failure mode.

In order to reduce the overall cost and time of designing composite materials/parts/structures, there is an obvious need to develop accurate analytical and numerical tools able to predict the mechanical response of composites under general loading conditions and geometries to assess the structural integrity of composites or to quantify their energy absorption capability, particularly in the development and introduction of advanced composite materials into new applications. Computational advances allowed numerous published demonstrations of successful representations of the initiation and propagation of damage in composite materials. Without such tools, the design process will rely on costly matrices of mechanical tests based on a large number of test specimens and empirical knockdown factors [58].

The introduction of high-fidelity analysis methods to the current design and certification processes in order to reduce empiricism and extensive structural testing has clear benefits. One of which is the quantification of the structural fracture resistance under various loading conditions, fundamental for evaluating the residual strength and life of composite structures [59]. Damage mechanics is the field that deals with a quantitative description of the physical events which lead to irreversible changes in a material due to the loads applied. It aims to describe the response of the material and modifications to the mechanical behaviour of the structure induced by an evolving damage state, describing damage initiation and evolution up to and including rupture [60, 61].

The greatest difficulty in the development of an accurate and computationally efficient numerical procedure to predict damage growth has to do with how to analyse the material micro-structural changes and how to relate those changes to the material response [58].

For composite materials, the onset and evolution of damage is different and generally more complex, than for metallic materials [62]. In composites the damage prior to failure involves a loss of stiffness and strength which is more relevant than in metals [58]. Thus, if a damage model is idealized to predict damage initiation and growth and establish the intensity of each failure mechanism, it should consider this progressive behaviour, leading to the progressive damage models [62, 63]. However, even in the case of laminated composites (the most studied and, therefore, the best understood ones), the prediction of damage initiation and propagation, including final fracture, remains a major challenge in modern mechanics of composite materials [58].

Advances in computational methods led to numerous published demonstrations of successful representations of the initiation and propagation of damage in composite materials, in the last years. These developments brought a diversity of approaches and it is necessary to ascertain the conditions in which a given model is expected to work and when it is no longer adequate, which is somewhat difficult given the complexity of these methods [58].

### 2.6.1 Damage scale

The scale at which the failure mechanisms are modelled highly influences the ability of the damage models to predict initiation and propagation of damage. The damage process idealization, its identification, characterization and formulation of governing physical principles, may include information from molecular dynamics scales to structural mechanics scales, including the intermediate micro and mesomechanic scales [64].

For composite laminates, the in-plane dimensions exceed the length scale in which the mechanisms of failure, such as delamination, matrix cracking and fibre debonding, occur by one to several orders of magnitude, therefore the modelling scale is of significant importance. At lower structural scales, damage idealizations have higher resolution, higher kinematic freedom and are able to recreate all kinds of damage mechanisms, each of these captured with separate damage laws [58].

**Micromechanical scale models**, are idealized with experimental data from the constituent level, therefore being the smallest scale of composite damage idealization [64–66]. The experimental data of fibres and matrix materials is necessary to establish the properties of, firstly, the lamina and, then, the laminate and structure [65].

Matrix damage mechanisms, such as matrix plasticity and damage, and fibre/matrix interface cracking are explicitly represented at this scale [64]. This approach must be capable of predicting the effects of material changes before lamina test data is available and the influence of the geometry

and spatial distribution of the phases on the mechanical behaviour of the lamina [58].

Micromechanical models can provide precise estimations of onset and propagation of damage and an accurate prediction of the failure strength, but are still incomplete in regards to predicting damage and final fracture localization [63, 67].

**Mesomechanical scale models** considers the laminate layers or the sublaminates as basic homogeneous building blocks with orthotropic material properties related to the directions of the fibres, obtained from lamina characterization tests. With this information these models are able to predict the behaviour of the complete laminate, not taking into account imperfections and the variabilities which characterize smaller scales [58]. Continuum damage mechanics (CDM) and discrete damage mechanics (DDM) are both typically used to predict damage progression at this scale. To account for micromechanical effects such as fibre/matrix debonding, some mesomechanical methods perform concurrent analysis on idealized unit-cell models that represent typical distribution patterns of fibres in the matrix. Other mechanisms, such as transverse matrix cracking or fibre kinking, which depend on meso-scale data such as ply thickness, are usually taken into account with failure criteria and *in situ* strengths. These failure criteria are used in conjunction with material degradation schemes to soften the material properties associated with a particular mode of failure [58].

The analysis of delamination is performed at this scale level, represented at the mesoscale as a hard discontinuity between plies, and modelled using cohesive elements or non-linear springs [64].

**Mesoscale CDM models** are the most common approach to analyse damage initiation and propagation of structural components [64]. These continuum methodologies are defined within the realms of thermodynamics irreversible processes and consider crack initiation and its growth as an ultimate consequence of a gradual local declining of material integrity. There is no necessity of calibration, thus can possibly provide a truly predictive methodology of damage onset and propagation [58]. It is assumed that plies are composed of a homogeneous material with orthotropic properties (in the case of composite laminates), and damage modes, such as fibre fracture, fibre kinking and delamination, are defined by a reduction of the corresponding stiffness. A set of continuous damage variables together with activation functions, which explicitly describe the local loss of material integrity, illustrates the density and/or redistribution of the microscopic defects that characterize damage [58]. Thus, localized damage is represented as a "soft discontinuity", in contrast to the "hard discontinuities" used in DDM models [64]. The redistribution of the stress state within the body produces a concentration of deformation in a small region in front of the crack tip which leads to damage growth. From this the direction and rate at which the crack will propagate can be established. Hence, crack initiation and growth follows the principles of continuum mechanics theory, instead of separate fracture criteria [66].

In **Mesoscale DDM models** the plies are represented at the meso-scale level, i.e., the material is assumed to be homogeneous with orthotropic properties, but displacement discontinuities, such as cracks, are treated as a zero-thickness cohesive process zones. In alternative, embedded discontinuity models, such as the extended finite element method (X-FEM) allows to introduce cracks and delamination in locations independent of mesh orientation and without necessity of remeshing [58].

**Macromechanical damage models** consider the structural level. The material is assumed homogeneous and the contributions of constituent materials are made in the form of apparent average properties of the composite material, therefore the analysis of stress fields and damage patterns are accomplished assuming the composite as an homogeneous material [60]. Hence, propagation

criteria at the structural level is highly dependent on the material system and configuration of the laminate, which means that the criteria have to be determined for each new material and laminate stacking sequence. Also these models do not have the ability to handle the characteristics of the crack-tip damage zone nor the complex interactions between micro and macro-failures associated with the crack-extension process. They simulate the crack-tip damage as an "effective" notch-tip damage zone that is assumed to grow in a self-similar manner. The lack of resolution in the damage mechanisms often renders structural-level damage models inaccurate after a short damage propagation period.

Multi-scale approaches divide the various aspects of a structural problem into several different levels of observation, each at a well defined *length scale*. These different levels are connected through *length scale transitions*, to homogenize the structural behaviour and mechanical properties of two conjoining levels, or through finite element analysis (FEA) that are conducted at two different levels simultaneously, connected by matching the boundary conditions at both levels, usually invoking periodicity to reduce the amount of computations that need to be performed [58]. Multi-scale analyses can be performed by using the best out of each level of analysis [60]. For instance, in an information-passing multi-scale approach, analyses on unit cells at the micro-scale can determine the stiffnesses and strengths of the unidirectional material through homogenization techniques, and the mesomechanical unit cell describes the fibre architecture of the composite, providing stiffnesses and strengths for computations at the macro-scale.

# Chapter 3

# Finite element, lightning and constitutive models

## 3.1 Geometry and finite element model

A parametric analysis to ascertain the variation on the damage induced by the direct effects of mechanical forces originated by a lightning strike on a CFRP plate is the purpose of this work. This is accomplished through Finite Element (FE) simulations performed using Abaqus/Explicit. The finite element model with solid elements was used in conjunction with a modified continuum damage mechanics model proposed by Miamí et al. [8].

The proposed study concerns the analysis of a square (400×400 mm) CFRP plate of 8 T700/M21 UD plies with a quasi-isotropic $[45/0/-45/90]_S$ lay-up. The samples were protected using Expanded Copper Foil (ECF) with a surface weight of 73.3 g/m$^2$, designated 2Cu4-100FA (also referred to as ECF 73), and no paint layer was applied.

The heterogeneous lightning protection layer, composed by the expanded copper foil, ECF 73, and Hexcel®M21 epoxy resin, is modelled as a homogeneous orthotropic material. The effective elastic constants and thermal expansion coefficients are numerically derived from a microstructural FE homogenization approach using the commercial FE package ANSYS [68]. Table 3.1 displays the main characteristics of this material.

**Table 3.1:** Main characteristics of the expanded copper foil.

| ECF | 2CU4-100FA |
|---|---|
| Surface weight (g/m$^2$) | 73.3 |
| Thickness (mm) | 0.051 |
| Long way of the diamond (mm) | 2.54 |
| Small way of the diamond (mm) | 1.39 |
| Strand width (mm) | 0.102 |
| Relative surface opening area (–) | 0.84 |

The composite laminate is modelled using 8-node C3D8R 3D brick elements with reduced integration to model each layer of the composite structure and also the lightning strike protection

(LSP) layer, Figure 3.1. Each composite ply is modelled as homogenous orthotropic material, assuming transverse isotropy.

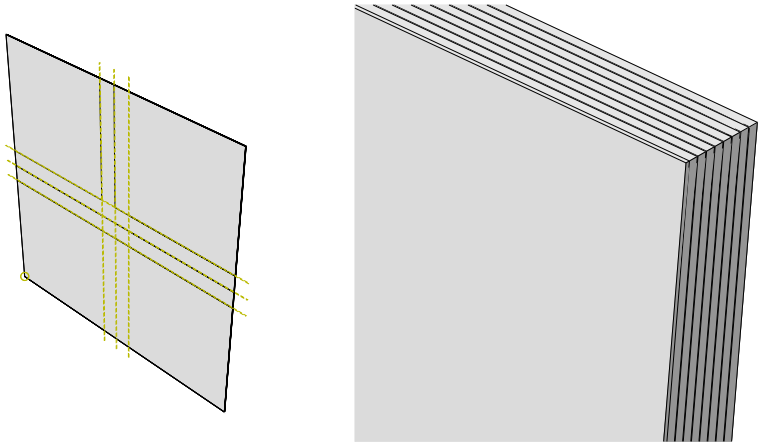


**Figure 3.1:** Model detail.

The aim of this parametric analysis is to show the performance and ability of the model to predict the behaviour of the composite plate with several different variants without the need to perform, time consuming, experimental tests. This allows a quicker design stage to decide upon the adequate material, to be validated in only one experimental test, complying with "right at first time" requirement of the industry. In this work, the analysis concerns the parameters:

- Stacking sequence effect;
- Lay up;
- Ply thickness effect.

The results are then compared to experimental observations in the literature.

The stacking sequence study is performed on an 8-ply symmetric quasi-isotropic laminate $[45/90/-45/0]_s$, with ply thickness of 0.118 mm and total thickness 1.065 mm, only varying the stacking sequence, to analyse the influence of the fibre relative angle. The considered cases are presented in Table 3.2.

**Table 3.2:** Alternative cases to study stacking sequence effects.

| Model | Stacking Sequence |
|---|---|
| $SS_1$ | $[0/45/90/-45]_s$ |
| $SS_2$ | $[-45/0/45/90]_s$ |
| $SS_3$ | $[90/-45/0/45]_s$ |
| $SS_4$ | $[0/90/45/-45]_s$ |

The lay-up effect and ply thickness is studied with respect to the same 8-ply symmetric quasi-isotropic laminate but now with the configurations of Table 3.3.

Individual plies are modelled by a single element, thickness-wise. To account for the *in situ* effect, consecutive plies with the same fibre orientation are attributed equal ply properties corresponding to the ply block thickness and position in the laminate, Table 3.5.

**Table 3.3:** Alternative cases to study lay-up and ply thickness effects.

| Model | Lay-up |
|---|---|
| UD | $[0]_8$ |
| CP | $[0/90]_{2s}$ |
| CP1 | $[0_2/90_2]_s$ |
| AP | $[45/-45]_{2s}$ |
| AP1 | $[45_2/-45_2]_s$ |

The mechanical properties of the plies used in the case studies are presented in Tables 3.4 and 3.5. The interlaminar properties are defined as: $G_{Ic}$ and $G_{IIc}$ are the Mode I and Mode II interlaminar fracture toughness, respectively, $\sigma_3$ and $\sigma_2$ are the Mode I and Mode II interlaminar strengths, respecitvely and $E_m$ is the elastic modulus of the interface material.

**Table 3.4:** Ply interlaminar and intralaminar properties.

| Interlaminar properties | $G_{Ic}$ N/mm | $G_{IIc}$ N/mm | $\sigma_3$ MPa | $\sigma_2$ MPa | $E_m$ MPa | | | | |
|---|---|---|---|---|---|---|---|---|---|
| | 0.765 | 1.25 | 60 | 60 | 7640 | | | | |
| Intralaminar properties | $E_{11}$ MPa | $E_{22}$ MPa | $G_{12}$ MPa | $\nu_{12}$ - | $\nu_{23}$ - | $S_{LP}$ MPa | $X_T$ MPa | $X_C$ MPa | $G_{XT}$ N/mm | $G_{XC}$ N/mm |
| | 165000 | 7640 | 5610 | 0.35 | 0.2 | 66.9 | 2200 | 1200 | 340 | 100000 |
| | $G_{YT}$ N/mm | $G_{YC}$ N/mm | $G_{SL}$ N/mm | $Y_{BT}$ MPa | $Y_{BC}$ MPa | | | | | |
| | 0.765 | 1.08335 | 1.25 | 46.5 | 592.75 | | | | | |

**Table 3.5:** Ply *in situ* properties.

| | $Y_T$ MPa | $Y_C$ MPa | $S_L$ MPa |
|---|---|---|---|
| 0.118 mm UD ply | 45 | 280 | 50 |
| 0.118 mm (single) inner ply | 252 | 686 | 122 |
| 0.236 mm (double) inner ply | 178 | 548 | 98 |
| 0.472 mm (four-ply block) inner ply | 126 | 464 | 83 |
| 0.118 mm (single) outer ply | 158 | 548 | 98 |
| 0.236 mm (double) outer ply | 112 | 464 | 83 |

The intralaminar properties are:

- $E_{11}$ - Longitudinal Young Modulus;
- $E_{22}$ - Transverse Young Modulus;
- $\nu_{12}$ - Poisson ratio;
- $\nu_{23}$ - Poisson ratio;

- $G_{12}$ - Transverse shear stiffness (in-plane);
- $S_{LP}$ - Plastic Shear;
- $X_T$ - Longitudinal tensile strength;
- $X_C$ - Longitudinal compressive strength;
- $G_{XT}$ - Mode I longitudinal fracture energy;
- $G_{XC}$ - Mode I longitudinal compression fracture energy;
- $G_{YT}$ - Mode I transverse fracture energy;
- $G_{YC}$ - Transverse compression fracture energy;
- $G_{SL}$ - Mode II transverse fracture energy;
- $Y_{BT}$ - Biaxial transverse tensile strength;
- $Y_{BC}$ - Biaxial transverse compressive strength;
- $Y_T$ - Transverse tensile strength (*in situ*);
- $Y_C$ - Transverse compression strength;
- $S_L$ - In-plane shear strength (*in situ*).

To obtain a more detailed information on the impact area, a fine mesh is applied in this zone. Outside of the impact area a coarser mesh is used for the sake of computational efficiency. The elements decrease their dimension linearly along the x and y axis towards the centre, Figure 3.2.

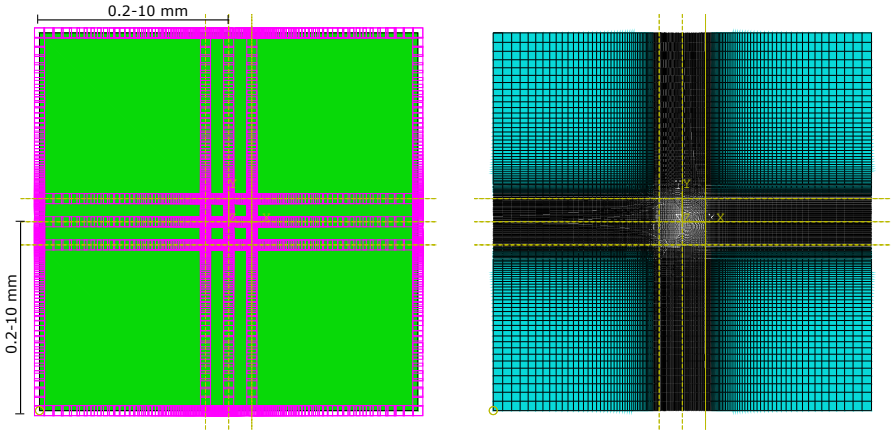



**Figure 3.2:** Seeding and mesh detail.

The following sections of this chapter present the mechanical loads applied in the model, the continuum damage model for intralaminar failure mechanisms and the modelling approach for delamination.

## 3.2 Mechanical lightning loads

Lightning strikes induce damage to materials used in airframe structures by several different physical mechanisms. These mechanisms, depend on the magnitude and rise time of the lightning current, have higher impact on structures made of composites materials, than on those made of metals, because of the low conductive characteristics of these materials. It is accepted that the most severe mechanical damage at and around the lightning attachment area protected and unprotected airframe composite structures/parts is caused by the transient lightning current components A or D [16], Figure 2.6. The mechanisms responsible for this damage are the shock waves generated by the exploding vaporized materials at the arc attachment area. However, the contributions from the shock waves caused by the supersonic expansion of the hot plasma channel and the magnetic volume forces caused by the impressed current flow in the electrically conducting structures cannot be neglected [68, 69].

The explosion of the lightning protection layer of CFRP structures is an important contribution to the mechanical damage. Experimental observations show that, when the arc root expands radially, the metallic protection is continuously removed from the top of the CFRP sample [70] and thermal damage on the first UD ply is relatively small. Therefore, it is assumed, as an approximation, that thermal and thermal-mechanical effects can be neglected, and mechanical damage is mainly caused by purely mechanical effects.

The mechanical loads applied to the model in this study follow the work of Karch et al. [68], with focus on the main non-thermal damage mechanisms and the mechanical forces resulting from lightning strikes: the magnetic field induced by the current impressed on the structures, the shock waves due to surface-explosions and the shock waves from supersonic channel expansion.

### 3.2.1 Lightning current

The lightning transient current waveform D is defined by the following double exponential function:

$$J(t) = \begin{cases} c(e^{-at} - e^{-bt}) & , \ t < t_{max} \\ c(e^{-af(t-v)} - e^{-bf(t-v)}) & , \ t \geqslant t_{max} \end{cases} \tag{3.1}$$

where $t_{max}$ is the time at the current peak. The parameters for the D current waveform with a time to peak of 26.8 $\mu$s, a decay time of 48.5 $\mu$s and a peak current of 96.4 kA, are given in Table 3.6.

**Table 3.6:** Parameters for root radius fit [68].

| $a$ ($s^{-1}$) | $b$ ($s^{-1}$) | $c$ (A) | $f$ (-) | $\nu$ (s) | $t_{max}$ (s) |
|---|---|---|---|---|---|
| 33833.1 | 41024.7 | 1361710.5 | 2.0814 | $1.392e^{-5}$ | $2.68e^{-5}$ |

### 3.2.2 Near surface explosion of the protection layer

The explosion of the LSP layer is assumed to be caused mainly by the rapid vaporization of the metallic mesh of the lightning protection layer due to Joule resistive heating. The spatial distribution of the expanding plasma pressure is assumed to be approximated by a Gaussian bell-shaped curve:

$$p(r,t) = p(t)k^{-2}\exp\left[-\frac{r^2}{(kR_R(t))^2}\right] \tag{3.2}$$

where $p(t)$ is the effective plasma overpressure, numerically determined in [68] and fitted to the sum of six Gauss functions of the form:

$$p(t) \approx \sum_{i=1}^{6} a_i \exp\left[-\left(\frac{log_{10}(t)-b_i}{c_i}\right)^2\right] - p_0 \tag{3.3}$$

where $p_0 = 1\ bar$ is the atmospheric pressure. The resulting parameters for ECF 73 are shown in Table 3.7 with t in $\mu s$ and $p(t)$ in bar. The parameter $k < 1$ is used to limit the pressure distribution mainly to the arc root area $\pi R_R(t)^2$.

**Table 3.7:** Parameters for the Gauss pressure fit of ECF 73 [68].

| $i$ | 1 | 2 | 3 | 4 | 5 | 6 |
|---|---|---|---|---|---|---|
| $a_i$ | 537.69 | -474.49 | -645.74 | 104.79 | -6913.8 | 8371.1 |
| $b_i$ | -1.0648 | -1.497 | -2.2927 | 0.16799 | -1.3168 | -1.3901 |
| $a_i$ | 0.20648 | 0.46628 | 0.59763 | 0.81308 | 0.5 | 0.86665 |

Karch et al. [68] calculated the root radius expansion $R_R(t)$ for the LSP layer using the finite volume degradation methodology. The computed root radius data of ECF 73 is fitted using a double exponential function until a time $t_s$, where it approaches a constant value $c = R_{R_0} + ae^{\alpha t_s} + be^{\beta t_s}$:

$$R_R(t) = \begin{cases} R_{R_0} + ae^{\alpha t} + be^{\beta t} & ,t \leqslant t_s \\ c & ,t > t_s \end{cases} \tag{3.4}$$

The parameters are shown in Table 3.8.

**Table 3.8:** Parameters for root radius expansion fit [68].

| | $a$ (mm) | $\alpha$ ($\mu$s$^{-1}$) | $b$ (mm) | $\beta$ ($\mu s^{-1}$) | $R_{R_0}$ (mm) | $t_s$ ($\mu$s) | c (mm) |
|---|---|---|---|---|---|---|---|
| ECF 73 | 50.726 | -0.001931 | -50.9 | -0.04668 | 0.5 | 64.2 | 42.7691 |

### 3.2.3 Supersonic plasma expansion

The supersonic shock wave is generated by the overpressure caused by the swift increase temperature of the plasma channel. The radially expanding shock wave is described by the following equation:

$$R_R(t) = \begin{cases} \alpha_s\sqrt{0.5}, & t < 0,5\ \mu s \\ \alpha_s\sqrt{t}, & t \geqslant 0,5\ \mu s \end{cases} \tag{3.5}$$

assuming a constant value for $t < 0.5$ $\mu$s, with $\alpha_s = 8.792528$ mm/$\sqrt{\mu s}$. The pressure of the shock wave up to the shock front $R(t)$ is expressed by the analytical approximation [68]:

$$p(t) = \begin{cases} \beta t, & t < 0,5\ \mu s \\ \dfrac{\alpha}{t}, & t \geqslant 0,5\ \mu s \\ 0, & t > 100\ \mu s \end{cases} \tag{3.6}$$

with $\alpha$=97.4562 bar·$\mu$s and $\beta$=388.1103 bar/$\mu$s.

### 3.2.4 Magnetic surface pressure

For protected CFRP structures the lightning current flow is mainly constrained within the high-conducting lightning protection layer. The lightning current flows from the plasma channel into the metallic protection layer through the arc root surface with an arc root radius $R_R(t)$. The thin protection layer can be formally split into two regions: the region that corresponds to the sample under the arc root ($0 < r < R_R(t)$) and the region beyond the arc root ($r > R_R(t)$). The effective magnetic surface pressure acting on the upper side of the LSP layer is:

$$p(r,t) = \begin{cases} \frac{\mu_r \mu_0 J(t)^2}{8\pi^2} \frac{r^2}{R_R^4(t)} & ,\ 0 < r < R_R(t) \\ \frac{\mu_r \mu_0 J(t)^2}{8\pi^2 r^2} & ,\ r > R_R(t) \end{cases} \tag{3.7}$$

where $\mu_0 = 4\pi \times 10^{-7}$ H·m$^{-1}$ is the permeability of the free space, $\mu_r = 1$ is the relative permeability of the non-magnetic LSP layer.

It is assumed that the contributions for the mechanical pressure induced by the explosion of the LSP layer, by the supersonic shock wave expansion, which depend both on time and space, act independently, neglecting any possible interactions between them.

The pressure distributions described before are applied to the top surface of the composite plate using a user-defined subroutine, **VDLOAD**, of the FE solver Abaqus/Explicit [71]. This user subroutine is used to specify the variation of the distributed load magnitude as a function of position and time on the top surface of the FE model. The equations are programmed into this subroutine. To allow a suitable time discretization of the applied surface pressures, the numerical simulation is divided into several steps. Table 3.9 presents the duration of each of these steps as defined in the FE model.

**Table 3.9:** Time duration of the FE steps.

| Step | Elapsed time ($\mu s$) |
|---|---|
| Near-surface Explosion | 0.1 |
| Shock Pressure | 0.9 |
| Magnetic Pressure | 9 |
| Final expansion | 40 |
| Over stressing | 300 |

## 3.3 Composite damage Model

The damage model used in conjunction with the finite element model for this analysis is a modified version of the continuum damage mechanics model proposed by Maimí et al. [8, 72], with the purpose to predict the onset of each intralaminar damage mechanism by means of appropriate damage initiation criteria [8] and damage accumulation through appropriate damage evolution laws [68, 72]. The material properties this model requires can be determined by standard experimental tests, such as ply-based test methods. This model employs ply properties, instead of laminate properties, which is an advantage. If laminate properties were used it would be necessary to test laminates for each lay-up or stacking sequence considered. This model also accounts for crack closure effects under load reversal, an important phenomenon in cases where a composite structure is subjected to multiaxial loading.

The model was modified to be suitable for cases where the triaxiality of the stress state is not negligible. The model proposed in [8, 72] assumed that the out-of-plane stress components are negligibly small to promote damage, and therefore only the in-plane stress components of the stress tensor activate damage. Therefore, in order to accurately predict damage initiation and evolution for 3D cases, the 3D invariant-based failure criterion for fibre kinking proposed in [56] is employed to define an artificial in-plane shear strength $S_L^{ef}$ which represents the effect of hydrostatic pressure on the shear response of the polymer matrix [73]. It is also applied to scale the fracture toughness for longitudinal compression, $G_{1-}$, and the longitudinal compressive strength ratio at the inflection point, $f_{XC}$, as a function of the applied hydrostatic pressure [73].

### 3.3.1 Complementary free energy and damage operator

The constitutive equations are formulated by the thermodynamics of irreversible processes. The constitutive law is defined by a scalar function, which must be positive definite and zero at the origin with respect to the free variables (the stresses) [74] and the complementary free energy density in the material. The ply complementary free energy density is defined as:

$$\begin{aligned} G = &\frac{\langle\sigma_{11}\rangle^2}{2(1-d_1)E_1} + \frac{\langle-\sigma_{11}\rangle^2}{2(1-d_1)E_{1c}} - \nu_{12}\sigma_{22}\left(\frac{\langle\sigma_{11}\rangle}{E_1} + \frac{\langle-\sigma_{11}\rangle}{E_{1c}}\right) + \frac{\sigma_{22}^2}{2(1-d_2)E_2} + \frac{\sigma_{12}^2}{2(1-d_6)G_{12}} + \\ &+(\alpha_{11}\sigma_{11} + \alpha_{22}\sigma_{22})\Delta T + (\beta_{11}\sigma_{11} + \beta_{22}\sigma_{22})\Delta M \end{aligned} \tag{3.8}$$

where $E_1$, $E_2$, $\nu_{12}$ and $G_{12}$ are the in-plane elastic orthotropic properties of a unidirectional lamina. Subscript 1 denotes the longitudinal (fibre) direction and 2 denotes the transverse direction. $\alpha_{11}$ and $\alpha_{22}$ are the coefficients of thermal expansion in the longitudinal and transverse directions, respectively. $\beta_{11}$ and $\beta_{22}$ are the coefficients of hygroscopic expansion in the longitudinal and transverse directions, respectively. $\Delta T$ and $\Delta M$ are the differences of temperature and moisture content with respect to the corresponding reference values. $\sigma_{ij}$ $(i, j = 1, 2)$ are the stress components and $d_i$ $(i = 1, 2, 6)$ are the scalar damage variables, related to longitudinal, transverse and shear damage modes, respectively.

The potential in equation (3.8) is the basis for establishing the relation between the stress and the strain tensors. To ensure the thermodynamic irreversibility of the damage process, the rate of change of the complementary free energy $\dot{G}$ minus the externally supplied work to the solid at constant strains, $\dot{\sigma} : \varepsilon$, must not be negative:

$$\dot{G} - \dot{\sigma} : \varepsilon \geqslant 0 \tag{3.9}$$

which leads to (ignoring the effects of temperature and moisture not considered in the model):

$$\varepsilon = \frac{\partial G}{\partial \sigma} = H : \sigma \tag{3.10}$$

$H$ is the lamina compliance tensor:

$$H = \frac{\partial^2 G}{\partial \sigma^2} = \begin{bmatrix} \frac{1}{(1-d_1)|\sigma_{11}|}\left(\frac{\langle\sigma_{11}\rangle}{E_1} + \frac{\langle-\sigma_{11}\rangle}{E_{1c}}\right) & \frac{-\nu_{12}}{|\sigma_{11}|}\left(\frac{\langle\sigma_{11}\rangle}{E_1} + \frac{\langle-\sigma_{11}\rangle}{E_{1c}}\right) & 0 \\ \frac{-\nu_{12}}{|\sigma_{11}|}\left(\frac{\langle\sigma_{11}\rangle}{E_1} + \frac{\langle-\sigma_{11}\rangle}{E_{1c}}\right) & \frac{1}{(1-d_2)E_2} & 0 \\ 0 & 0 & \frac{1}{(1-d_6)G_{12}} \end{bmatrix} \tag{3.11}$$

The closure of transverse cracks under load reversal is taken into account by defining four damage variables associated with longitudinal and transverse damage. To determine the active damage variables, it is necessary to define the longitudinal and transverse damage modes, equations (3.12) and (3.13):

$$d_1 = d_{1+}\frac{\langle\sigma_{11}\rangle}{|\sigma_{11}|} + d_{1-}\frac{\langle-\sigma_{11}\rangle}{|\sigma_{11}|} \tag{3.12}$$

$$d_2 = d_{2+}\frac{\langle\sigma_{22}\rangle}{|\sigma_{22}|} + d_{2-}\frac{\langle-\sigma_{22}\rangle}{|\sigma_{22}|} \tag{3.13}$$

The damage caused by tension is separated from damage by compression, depending on the sign of the respective stress. The shear damage variable, $d_6$, is not affected by the closure effect.

### 3.3.2 Damage activation functions

This model assumes a domain of elastic response based on the mechanisms of failure, or crack generation, of advanced composites. It is assumed that the elastic domain is enclosed by the four surfaces of each failure mechanism: longitudinal and transverse fracture under tension and compression. The surfaces of the domain are materialized by damage activation functions based on the LARC03 criteria [47] and the 3-D invariant-based failure criteria [56].

The four damage activation functions, $F_N$, relative to failure mechanisms in longitudinal ($N = 1+, 1-$) and transverse ($N = 2+, 2-$) modes are:

$$\begin{aligned} F_{1+} &= \phi_{1+} - r_{1+} \leqslant 0, \quad F_{1-} = \phi_{1-} - r_{1-} \leqslant 0, \\ F_{2+} &= \phi_{2+} - r_{2+} \leqslant 0, \quad F_{2-} = \phi_{2-} - r_{2-} \leqslant 0. \end{aligned} \tag{3.14}$$

The loading functions $\phi_N$ are defined by the failure criteria and depend on the strain tensor and material elastic and strength properties. $r_n$ are the elastic domain thresholds, associated with the relative failure mechanism, ($N = 1+, 1-, 2+, 2-$). Their initial value is 1 for undamaged material and increase with damage. This internal variables are related to the damage variables, $d_m$, by means of damage evolution laws.

### 3.3.3 Damage evolution

The evolution of the damage threshold values, $r_N$, is expressed by the Kuhn–Tucker conditions:

$$\dot{r}_N \geqslant 0;\ F_N \leqslant 0;\ \dot{r}_N F_N = 0 \tag{3.15}$$

Neglecting viscous effects, the damage activation functions, equations (3.14) have to be non-positive. While the damage activation function $F_N$ is negative, the material response is elastic. When the strain state activates a criterion, $F_N = 0$, it is necessary to evaluate the gradient $\dot{\phi}_N$. If the gradient is not positive, the state is one of unloading or neutral loading. If the gradient $\dot{\phi}_N$ is positive, there is damage evolution, and the consistency condition has to be satisfied:

$$\dot{F}_N = \dot{\phi}_N - \dot{r}_N \tag{3.16}$$

Under these conditions, it is possible to integrate the constitutive model explicitly. It is assumed that the longitudinal and transverse domains are not coupled.

#### 3.3.3.1 Transverse loading

Under load reversal, transverse cracks, which are perpendicular to the ply midplane, do not affect the compression response: the elastic domain and the compressive damage variable, $d_{2-}$, is not affected by $r_{2+}$. But matrix cracks caused by high compressive transverse stresses have the same effect as cracks perpendicular to the midplane when the load is reversed from compression to tension. Therefore the evolution of the elastic domain in the transverse direction is characterized by:

$$\text{Tension loading: } \dot{r}_{2+} = \dot{\phi}_{2+} \text{ and } \dot{r}_{2-} = 0 \tag{3.17}$$

$$\text{Compression loading: } \dot{r}_{2-} = \dot{\phi}_{2-} \text{ and } \dot{r}_{2+} = \begin{cases} \dot{\phi}_{2-} & \text{if } r_{2+} \leqslant r_{2-} \\ 0 & \text{if } r_{2+} > r_{2-} \end{cases} \tag{3.18}$$

Integration of this expressions results in:

$$r_{2+} = \max\left\{1, \max\left\{\phi^s_{2-}\right\}, \max\left\{\phi^s_{2+}\right\}\right\} \tag{3.19}$$

$$r_{2-} = \max\left\{1, \max\left\{\phi^s_{2-}\right\}\right\} \tag{3.20}$$

#### 3.3.3.2 Longitudinal loading

Under longitudinal tensile stresses, the fracture plane is perpendicular to the fiber direction. When reversing the load, the cracks close and can still transfer load. However, the broken and misaligned fibers do not carry any additional load. Therefore, the compressive stiffness is influenced by longitudinal damage. However, the elastic domain is assumed to remain unchanged. When the loads are reversed, the cracks generated in compression open and the elastic domain threshold increases. Therefore, the evolution of damage thresholds are:

$$\text{Tension loading: } \dot{r}_{1+} = \dot{\phi}_{1+} \text{ and } \dot{r}_{1-} = 0 \tag{3.21}$$

$$\text{Compression loading: } \dot{r}_{1-} = \dot{\phi}_{1-} \text{ and } \dot{r}_{1+} = \begin{cases} \dot{\phi}_{1-} & \text{if } r_{1+} \leqslant r_{1-} \\ 0 & \text{if } r_{1+} > r_{1-} \end{cases} \tag{3.22}$$

Integration of this expressions results in:

$$r_{1+} = \max\left\{1, \max\left\{\phi^s_{1-}\right\}, \max\left\{\phi^s_{1+}\right\}\right\} \tag{3.23}$$

$$r_{1-} = \max\left\{1, \max\left\{\phi^s_{1-}\right\}\right\} \tag{3.24}$$

### 3.3.4 Damage laws

Bilinear softening laws are used to model longitudinal damage growth in tension and in compression, including a residual stress plateau in compression to more accurately capture kink band broadening under crushing loads, Figure 3.3A-B. To model transverse tensile and compressive damage growth, linear softening laws are used, Figure 3.3C. Finally, to represent the inelastic in-plane shear response, a bilinear elasto-plastic law is assumed, followed by a linear softening law, Figure 3.3 [68].

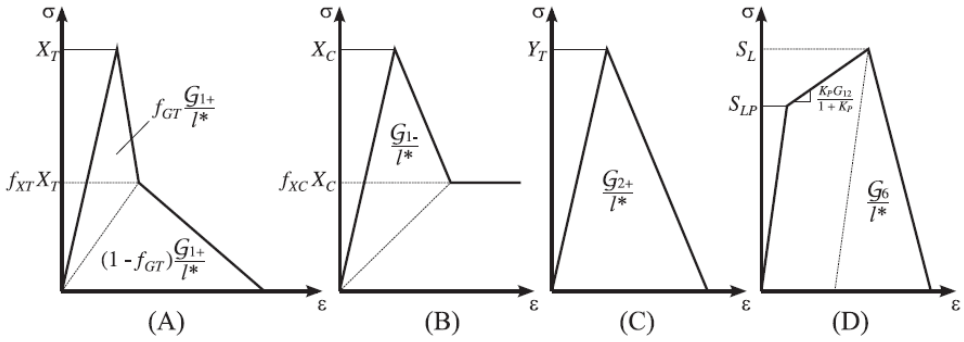



**Figure 3.3:** Damage evolution laws for longitudinal tension (A), longitudinal compression (B), transverse tension/compression (C), and in-plane longitudinal shear (D) failure modes [68].

The damage evolution laws used force strain softening as soon as one damage activation criterion is satisfied. However, softening constitutive equations may result in physically inadmissible responses.

While the stress–strain response of a material exhibits a positive definite tangent stiffness tensor there is an initial stage of damage commonly referred to as diffuse damage, and the numerical solution is independent of the numerical discretization. When the tangent stiffness tensor is not positive definite, damage localizes in a narrow band, and the numerical solution depends upon the numerical discretization: decreasing the element size in the localized zone decreases the computed energy dissipated. Therefore, the structural response is not objective because it does not converge to a unique solution with mesh refinement [72].

An energy regularization approach based on the fracture energy associated to each failure mechanism and based on the characteristic length of the finite elements, $l^*$, is used to ensure mesh independent results after damage onset, Figure 3.3. This regularization procedure is based on the crack band model proposed in [75]:

$$g_M = \frac{G_M}{l^*} \tag{3.25}$$

where $G_M$ is the fracture toughness, $g_M$ is the energy dissipated per unit volume, and $l^*$ is the characteristic length of the finite element.

This model is implemented in a user-defined subroutine **VUMAT** of the FE solver Abaqus/Explicit [71].

## 3.4 Delamination

Delamination between plies is modelled using a cohesive zone model implemented in the user-written material subroutine, VUMAT. The cohesive interaction is defined by a bilinear traction-separation damage law accounting for mode dependency according to the B-K law [76]. The cohesive element simulates the onset and propagation of the delamination in advanced composite materials. The delamination model is formulated by using a rigorous thermodynamic framework which takes into account the changes of mixed-mode loading conditions.

Mode-dependent (mode I and mode II) strengths and fracture energies are considered. The onset of interlaminar damage is predicted by a quadratic stress-based criterion. Turon et al. [77] demonstrated that changes in the local mode ratio in the evolution of damage during mixed mode loading might lead to erroneous calculation of the energy dissipation. For this reason, the shear strengths $\tau_1 = \tau_2$ are not fully independent material properties, but instead they are determined as a function of the mode I and mode II fracture toughness, $G_{Ic}$ and $G_{IIc}$ respectively, and the normal strength $\tau_3$:

$$\tau_1 = \tau_2 = \tau_3 \cdot \sqrt{\frac{G_{IIc}}{G_{Ic}}} \tag{3.26}$$

# Chapter 4

# Model definitions and convergence study

## 4.1 Mass Scaling

### 4.1.1 Introduction

Industry design and development of objects, materials, structures, etc, has progressively become less expensive and less time consuming due to simulation based design, which has become a standard tool, in particular the finite element method (FEM). Simulations are used whether in stationary or dynamic analysis.

For dynamic analysis, time integration can be carried out in explicit or implicit forms. Explicit integration in finite elements is a popular method to simulate the dynamic behaviour of a system due to their inherent lack of convergence problems. To apply a formally explicit form, one must use a lumped mass matrix in which the equations of motion are decoupled. This integration form leads to lower required memory and minimal time per time step, because the time step size needed to solve the transients is often of the same order of magnitude as the critical time step imposed by the conditional stability of the time integration scheme. The drawback is that this method is only conditionally stable and the time step must be smaller than the so-called critical time step, in order to avoid numerical instabilities [78–80]. Therefore, runtime on a transient dynamics model is not only function of the model size but also the time step.

These difficulties are particularly relevant for solid-shell models or a model in which the thickness is significantly smaller than the in-plane dimensions, in which the problem of high ratio of transverse to in-plane normal stiffness arises, with a high finite element maximum eigenfrequency and, hence, stiffness matrix ill-conditioning [81].

In explicit dynamics, the time step is internally calculated to provide a stable solution and to accurately predict the propagation of the highest frequency waves in the model, the stress and shock waves.

In an undamped case a stable time-step must satisfy the condition:

$$\Delta t \leqslant \frac{2}{\omega_{max}} \tag{4.1}$$

where $\omega_{max}$ is the maximum eigenfrequency of the assembled mesh. Also:

$$\omega_{max} \leqslant \omega^{e}_{max} \tag{4.2}$$

$\omega^{e}_{max}$ is the highest eigenfrequency of an individual element in the mesh. A physical interpretation of the stability limit can be obtained from the Courant, Friedrichs and Lewy condition which prescribes that the time-step must be smaller than the time required by a dilatational stress wave to traverse the smallest element of the mesh [81]:

$$\Delta t \leqslant \frac{L^e}{c},\ c = \sqrt{\frac{\lambda + 2\mu}{\rho}} \tag{4.3}$$

$L^e$ is the element smallest geometric dimension (element characteristic length), $\lambda$ and $\mu$ are Lame's constants, $\rho$ is the mass density and $c$ is the wave propagation speed.

One approach commonly used in the structural dynamics community to increase the critical time step in a heuristic manner is *mass scaling*. Two different methods for *mass scaling* can be found in the literature.

The simplest method is to simply increase uniformly the mass density of the material, which means this technique is not mass preserving. This increase will affect in the same way all structural eigenmodes, which can lead to unacceptable inaccuracies. This method has been reported as satisfactory for relatively slow forming processes.

A more accurate approach is to add a non-diagonal matrix with net zero mass to the original mass matrix. This method is mass-preserving and affects mainly the higher frequencies, thus it is more suitable for dynamic analysis. In inertia dominated problems, better results can then be obtained by selectively scaling element masses, in such a way that masses associated to element rigid body modes are not modified [80, 81].

Since the critical time step is limited by the highest eigenfrequency of the system, it would be preferable to focus the mass scaling to the upper eigenfrequency domain which generally only contains small amounts of kinetic energy and the lower eigenfrequency domain should remain as unaffected as possible [78, 79]. This method is designated as *selective mass scaling*, increasing density only in the smallest elements which control the time step.

### 4.1.2 Reference model analysis

The reference model, in this work, is a model of an 8-plies CFRP plate $[45/90/-45/0]_s$, where the interface between different plies is defined by cohesive elements, forming interlaminar layers. The thickness of these layers is considerably smaller than the thickness of a ply. Consequently, due to this smaller thickness, the characteristic length, $L^e$, of these elements will be very small. The small $L^e$ will force Abaqus/Explicit to introduce a very small time increment throughout the whole model, leading to a very large computational time to complete the simulation.

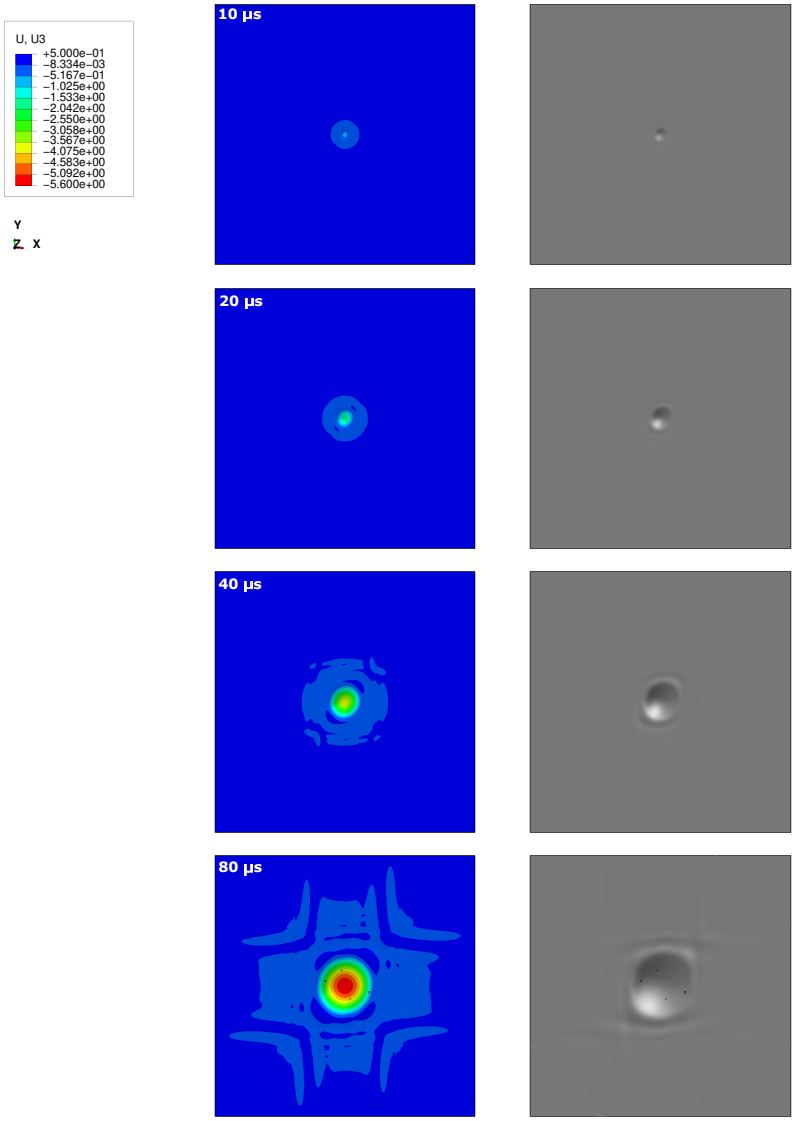
To improve computational efficiency it is possible, in Abaqus, to scale the mass of these controlling elements at the beginning of each step, and therefore, increase significantly the stable time increment. Normally, the mass increase is very small, thus, the produced effect on the overall dynamic behaviour of the model may be negligible [71].

The loading solicitation of the analysis which models the mechanical effects of the lightning strike can be resembled to an impact analysis. In this case, the elements closer to the impact zone

are expected to suffer significant amounts of deformation and their reduced characteristic lengths will result in a smaller global time increment which leads to a considerably large computational time. Also, the progressively defined discretization adopted, in order to have better precision on the impact zone, includes fine meshes in some regions that will define and impose a small time step to the whole model.

The analysis of the reference model was performed without *mass scaling* to evaluate the computational efficiency, and also, to provide data to be analysed and compared against more efficient models. The model provided the expected results, but had a very large computational time.

Deformation occurs immediately after the lightning strike, Figure 4.1b. The impact creates a very small crater which progressively grows and it is already easily visible at 10 $\mu$s. Deformation is immediately present in all the plies, being visible from the back of the plate, Figure 4.2.




a) b)

**Figure 4.1:** Evolution of a) displacement in the thickness direction ($U_3$) and b) deformed mesh on the top ply of the reference model.

### 4.1. Mass Scaling

Throughout the time the crater becomes larger and deeper, Figure 4.1b, confirmed by the growth of displacements in the thickness direction, Figure 4.1a. The displacement is very small in the earliest times being less than 0.7 mm at 10 $\mu$s and then it grows very quickly to 5.6 mm at 80 $\mu$s.

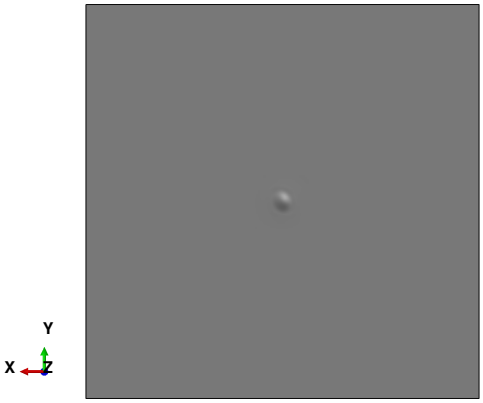



**Figure 4.2:** Crater visible on the bottom ply at 10 $\mu$s.

The stress state evolution predictably has a similar behaviour, being very small in the initial instants and growing very quickly. In the beginning it is very localized and then it spreads. The maximum is reached at around 40 $\mu$s. Figure 4.3 shows different stress states between the top and bottom ply at equal instants.

The top ply has two separate regions that achieve the maximum stress and spread individually, whereas the bottom ply has a single larger stressed region. Figures 4.4 and 4.5 show the influence of the orientation of the fibres on the stress field, by comparing the Maximum Principal (Absolute) stress with the corresponding internal variable corresponding to the fibre tension failure mode. It is shown that the higher magnitudes of the stress field occur at the two topmost layers, thus, where more damage is expected.

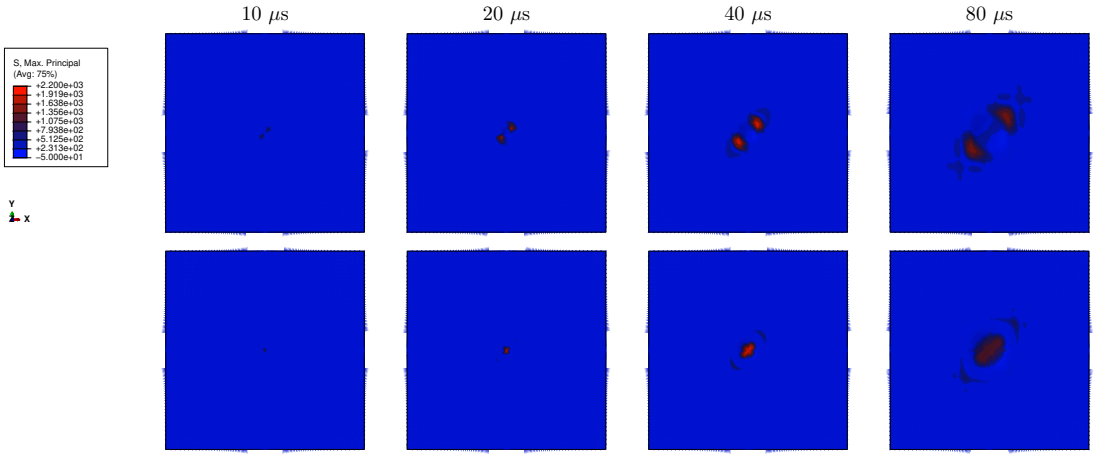



**Figure 4.3:** Evolution of the maximum principal stress top) on the top ply and bottom) on the bottom ply of the reference model.

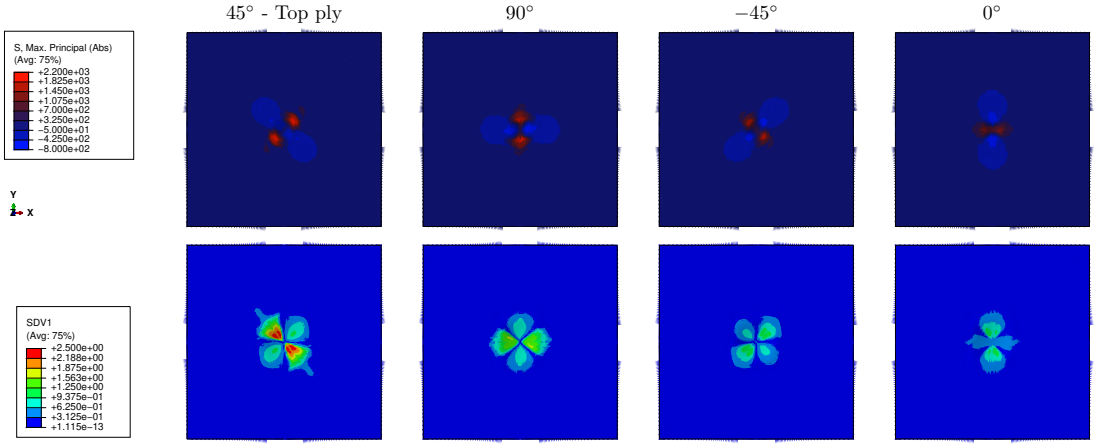



**Figure 4.4:** Maps of top) Maximum Principal (Absolute) stress and bottom) internal variable corresponding to fibre tension failure of the 4 top layers at 40 $\mu$s.

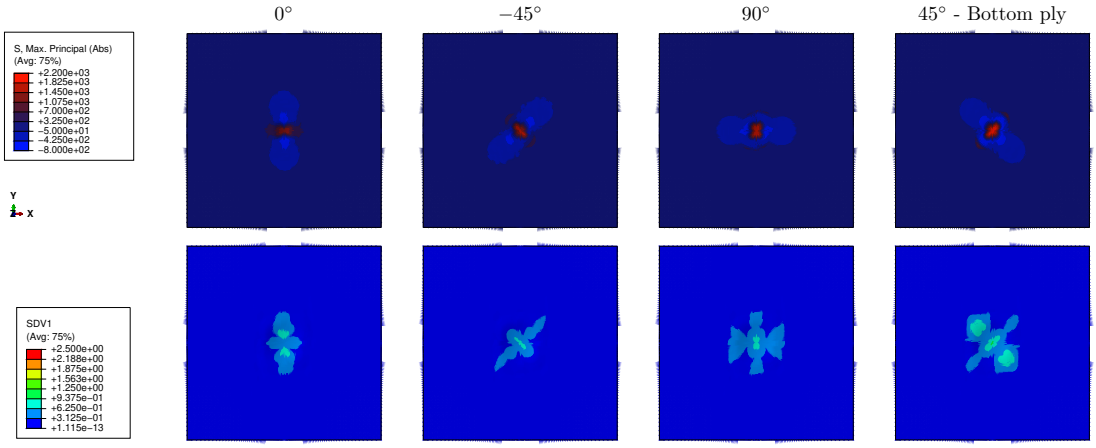



**Figure 4.5:** Maps of top) Maximum Principal (Absolute) stress and bottom) internal variable corresponding to fibre tension failure of the 4 bottom layers at 40 $\mu$s.

This simulation ran for 239.05 h, more than a week, and it was stopped before reaching the end. During this time the simulation ran through all the steps until the final of the first frame of step 5, *over stressing*. The elapsed time was circa 80 $\mu s$ of the total 350 $\mu s$. The large computational time was caused by the low stable time increment of the interlaminar elements defined by Abaqus as the critical elements. The compressive deformation imposed to some of these very small elements was very severe, resulting in considerable variation of their sizes which led to a very small time step increment, between $5.683 \times 10^{-11}$ to $7.699 \times 10^{-11}$ from step 3, *magnetic pressure*, onwards. The magnitude of this stable increment was two orders lower than the order of the stable increment until step 2, greatly increasing the CPU run time. Figure 4.6 shows the location of the most critical element.

The simulation ran for more than a week and still missing one step, which is not desirable nor admissible for real industry simulations. *Mass scaling* was applied to reduce this time significantly.

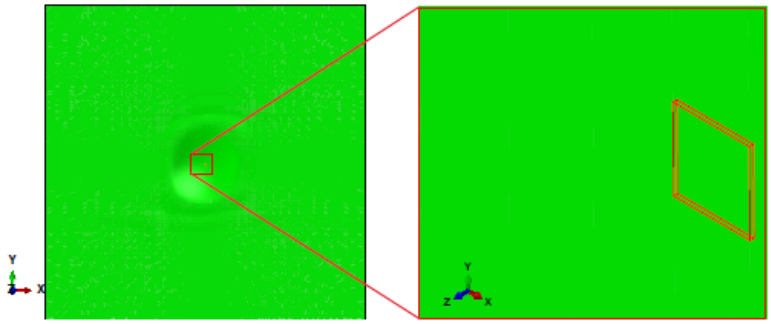


**Figure 4.6:** Critical interlaminar element responsible for the small time step increment.

In Abaqus, *mass scaling* is an automated procedure allowing the user to define an allowable minimum time step. Once this minimum is defined the code will perform *mass scaling* by increasing only the density of the elements which are controlling the time step,i.e., the elements that impose a time increment lower than the minimum defined. This *selective mass scaling* is very efficient by only increasing the density of necessary elements, meaning that the increase of mass in the whole model is as minimal as required.

The computational time of the original model was very high with increments of magnitude $10^{-11}$ s. To achieve an acceptable time duration for the simulations, the minimal time step increments will be one and two orders higher. Three models with different minimum time step will be analysed and compared to the original, Table 4.1.

**Table 4.1:** Alternative cases to study the *mass scaling* effect.

| Model | Imposed minimum stable time increment (s) |
|---|---|
| Original | - |
| $MS_1$ | $1.00\times10^{-9}$ |
| $MS_2$ | $5.00\times10^{-10}$ |
| $MS_3$ | $1.00\times10^{-10}$ |

### 4.1.3 Discussion

*Mass scaling* introduces modifications in the model to a certain degree, which will eventually lead to a variation in results. An exaggerated increase in mass percentage introduces significant modifications to the kinetics of the model and may lead to a different behaviour from that of the original model, which means that an analysis is necessary to identify the adequate *mass scaling* to use in order to have a similar model and much better computational efficiency. As explained earlier, in Abaqus, one way to define the degree of *mass scaling* is to limit the minimum time step increment. Its selection can be determined by a parametric analysis. The objective of the parametric analysis is the identification of an adequate minimum time step which would increase the density of required elements and lower the computation time, whilst providing accurate solutions.

Computational time is influenced by the imposed time step. Increasing the minimum time step imposed to the model leads to a shorter time duration of the simulations but also higher increase of mass, which modifies the mass matrix of the system and can lead to erroneous results. To this end

several models with different minimum time steps were tested and their results compared to those of the original model without *mass scaling*. The adequate time step increment is the one which leads to the fastest run time without introducing significant changes to the model and its results. To establish the acceptability of an applied *mass scaling*, the kinetic energy, the internal energy, displacements and velocities of each model can be compared [82]. Figures 4.7 and 4.8 show the behaviour of the evolution of the kinetic and internal energy of the reference model. Figure 4.9 shows the displacement in the thickness direction of the centre of the plate.

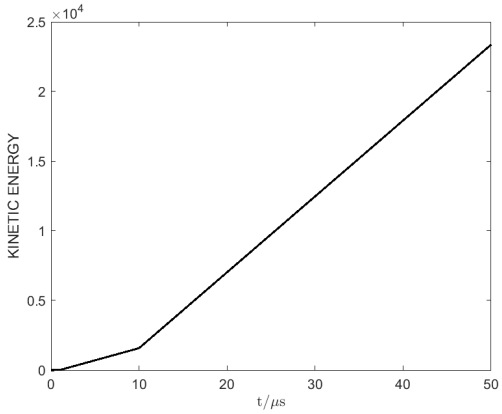



**Figure 4.7:** Kinetic energy of the reference model.

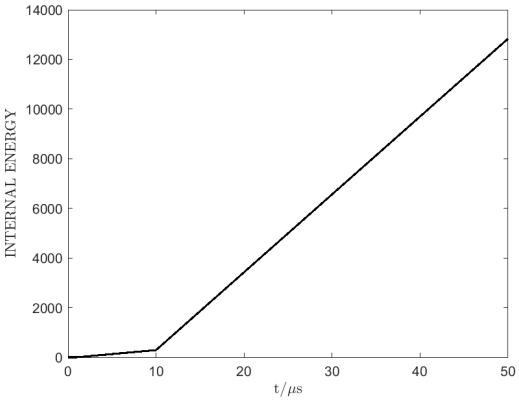



**Figure 4.8:** Internal energy of the reference model.

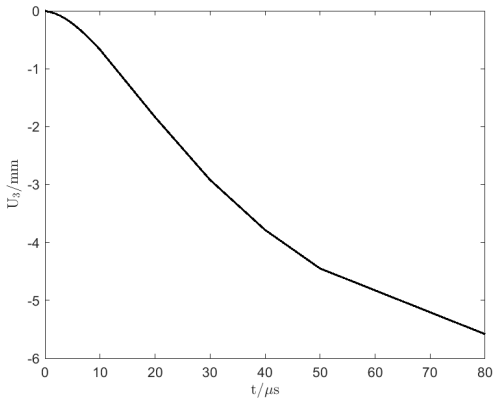



**Figure 4.9:** Displacement of the centre of the reference model in the thickness direction.

Table 4.2 shows the mass change of the system, which is very small in all cases. As expected, model $MS_3$ with the lowest mass change is the most accurate. In the other two cases, $MS_1$ and

$MS_2$, the percentage of mass change is higher which means that a greater quantity of elements had its density increased in order to respect the minimum stable time increment, introducing slight variations to the results. The column named Von Mises presents the maximum Von Mises stress achieved in the top layer throughout the lightning, which occurred at 20 $\mu$s. The tension values of all models were very similar and close to the reference model. The simulations run time decreased drastically, from more than a week to three or one day and a few hours, which was the goal of this analysis.

**Table 4.2:** Performance parameters of the models under study.

| Model | Minimum stable increment (s) | CPU Time (h) | Mass Change (%) | Maximum Von Mises stress (MPa) |
|---|---|---|---|---|
| Original | - | 239.05 (incomplete) | - | $2.184\times10^{3}$ |
| $MS_1$ | $1.00\times10^{-9}$ | 31.93 | $7.45\times10^{-5}$ | $2.185\times10^{3}$ |
| $MS_2$ | $5.00\times10^{-10}$ | 29.50 | $3.01\times10^{-5}$ | $2.185\times10^{3}$ |
| $MS_3$ | $1.00\times10^{-10}$ | 65.00 | $2.50\times10^{-6}$ | $2.183\times10^{3}$ |

Table 4.3 presents the maximum values of the damage variables, for all models. The maximum damage values occurred before 80 $\mu$s, after this instant the damage variables decreased in all models where the information is available, which leads to believe that these are the maximum damage values even for the reference model. Tables 4.4 and 4.5 show the maps of the envelope of the damage variables for the two topmost layers. It is of interest that the models analysed predict damage fairly well, and for that reason it is essential that, even though the mass of the system is altered, these variables show similar behaviour.

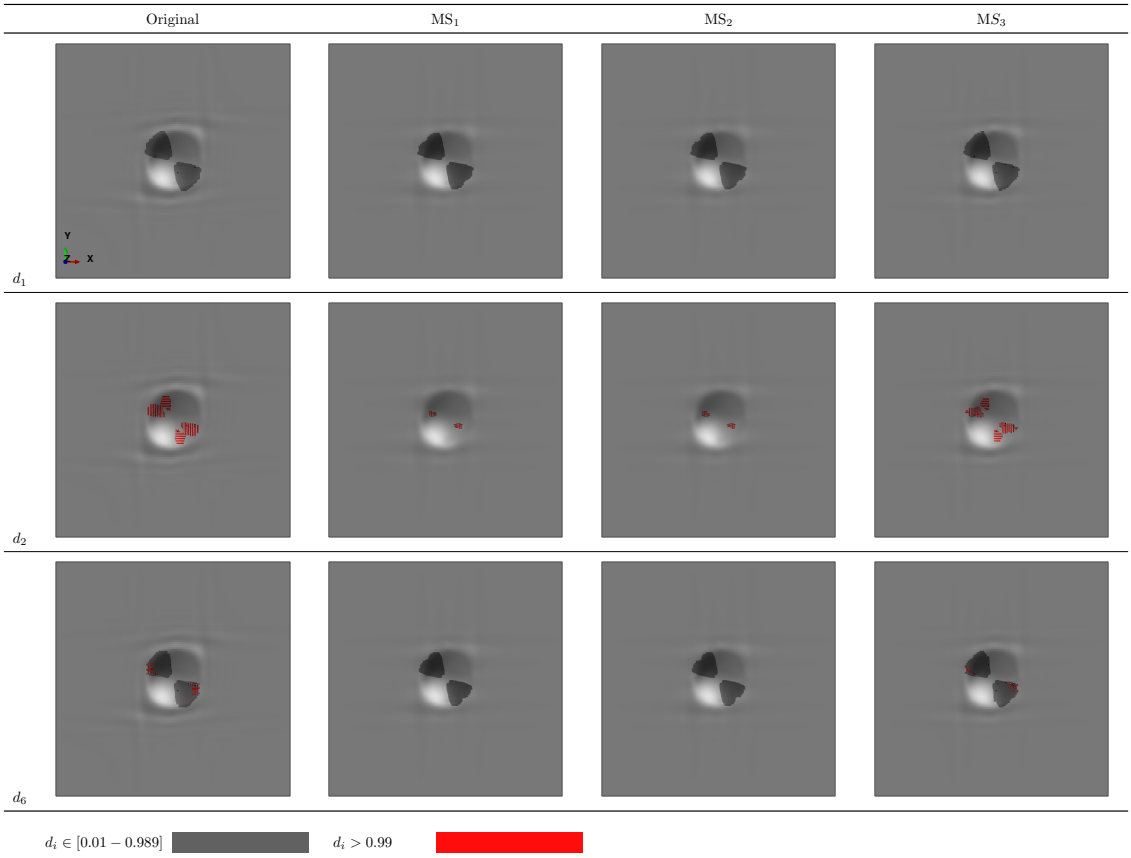
**Table 4.3:** Maximum values of the damage variables for the two top layers.

| | Top layer | | | Second topmost layer | | |
|---|---|---|---|---|---|---|
| | $d_1$ | $d_2$ | $d_6$ | $d_1$ | $d_2$ | $d_6$ |
| Original | 0.6949 | 0.9900 | 0.9900 | 0.5371 | 0.9800 | 0.9800 |
| $MS_1$ | 0.6341 | 0.9900 | 0.8459 | 0.4037 | 0.0000 | 0.3691 |
| $MS_2$ | 0.6339 | 0.9900 | 0.8438 | 0.4038 | 0.0000 | 0.3691 |
| $MS_3$ | 0.6866 | 0.9900 | 0.9900 | 0.5327 | 0.9800 | 0.9800 |

Tables 4.4 and 4.5 show that all the models presented similar behaviour regarding the damage variable in the longitudinal direction, $d_1$. For the damage variable in the transverse direction, $d_2$, models $MS_1$ and $MS_2$ showed significantly different behaviour even for the top layer. As can be seen in Table 4.4 the envelope for these models is significantly smaller than that of the original model. In the second topmost layer these two models do not show any damage at all in the transverse direction. The maximum values of these two damage variables, Table 4.3, predicted by these two models are significantly lower, especially for the second topmost layer. The shear damage variable, $d_6$, is a combination of the other two damage variables, thus, these models have a significant different behaviour regarding this damage variable.

All the damage envelopes of the model $MS_3$ are very close in area and shape to the reference model, as are the maximum values of the damage variables. Thus, this model shows a behaviour which is very similar to the reference model regarding damage.

**Table 4.4:** Maps of the envelope of the damage variables of the top ply for the *mass scaling* analysis at 80 $\mu$s.




Figures 4.10 and 4.11 show a comparison between the kinetic and internal energy of the models. This comparison highlights important differences between the behaviour of models $MS_1$ and $MS_2$ to the behaviour of the original model. The higher percentage of mass increase in the system led to a significant different behaviour, as noted before.

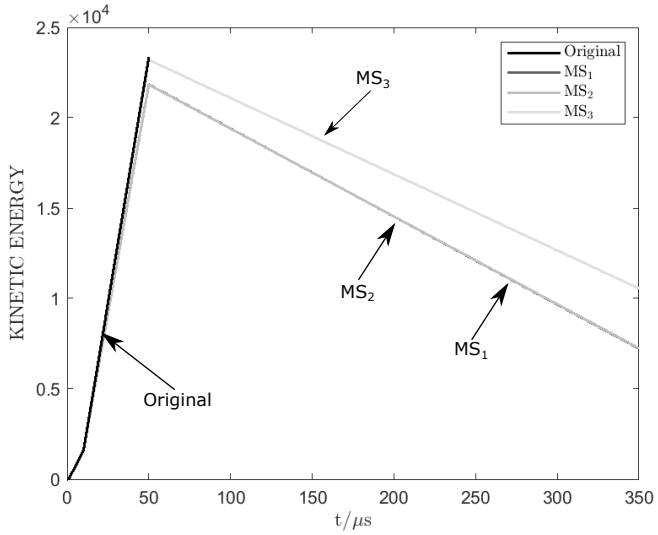



**Figure 4.10:** Comparison of the kinetic energy.

### 4.1. Mass Scaling

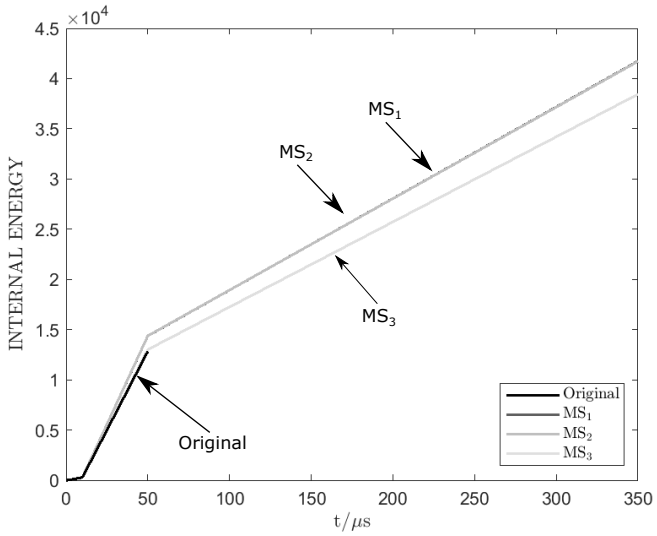
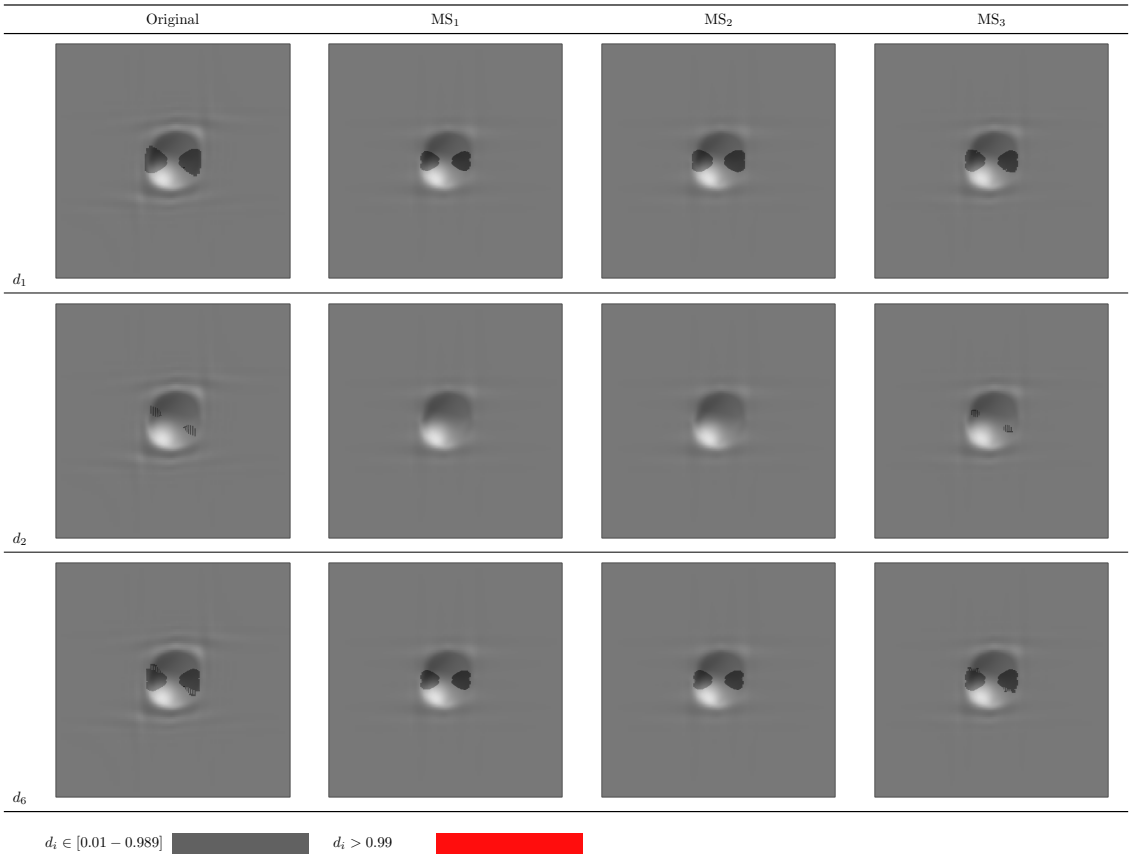



**Figure 4.11:** Comparison of the internal energy.

Although the increase in mass may seem very small the results show it was significant enough to provoke a shift in the energies of the system. These models present lower maximum kinetic energy and higher maximum internal energy, compared with the original model. Also the slopes, which give the initial growth rates of each energy, are significantly different.

**Table 4.5:** Maps of the envelope of the damage variables of the second topmost ply for the *mass scaling* analysis at 80 $\mu$s.



Model $MS_3$, on the other hand, produced similar results to the original model. The highest difference of the maximum values of the damage variables is only 1.2%, remarkable considering the computational time has reduced from 239.05 (incomplete) to 65 hours (complete). Also, in terms of energy the behaviour of model $MS_3$ is very similar to the original model. Figures 4.10 and 4.11 show that the growth rates of the kinetic and internal energy of $MS_3$ are identical to the reference model.

Figure 4.12 shows the evolution of the displacement of the centre of the top layer in the thickness direction. In the time interval, 80 $\mu$s, in which data is available for the Original model, there is hardly any understandable difference between all models. After that, relatively small differences can be seen, but too small to be relevant.

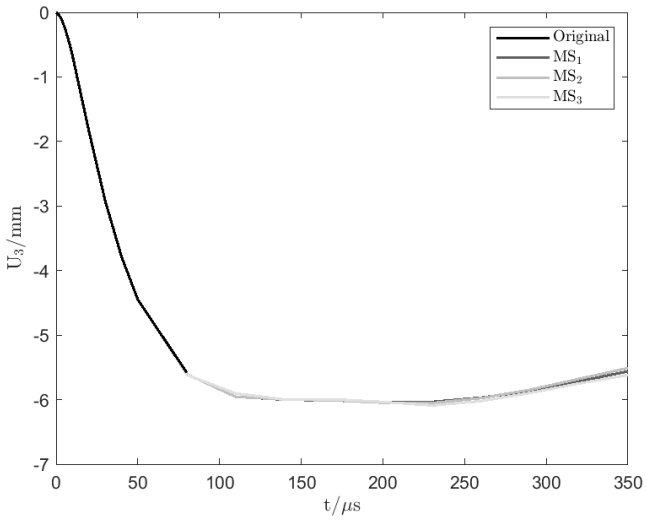



**Figure 4.12:** Comparison of the displacement of the centre of the top layer.

## 4.2 Mesh Sensitivity

Finite element models may be influenced by the dimension of their elements. If their dimensions are not adequate the results can have an inadmissible degree of error or will not be able to describe with precision the phenomenon under analysis. A mesh sensitivity analysis enables the understanding of the response of the model with different mesh sizes. Computational efficiency is also affected by the discretization of the mesh. A model with a higher level of discretization, and therefore, composed by a higher number of elements, will have a longer time duration for each simulation. With the analysis of the spatial discretization, an adequate mesh can be selected, which has at the same time acceptable precision and suitable simulation time duration.

The reference model has a minimum element size of 0.2 mm and a maximum element size of 10 mm. The size of the elements grows linearly from the centre of the model to the periphery, Figure 4.13. The lightning strike is applied on the centre of the panel, therefore, it is important that on the centre the elements are very small and in high number, to be able to describe with precision the behaviour of the composite.

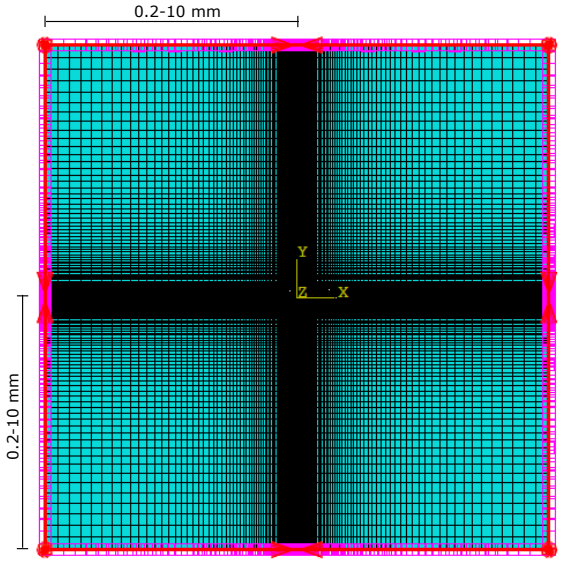



**Figure 4.13:** Mesh discretization.

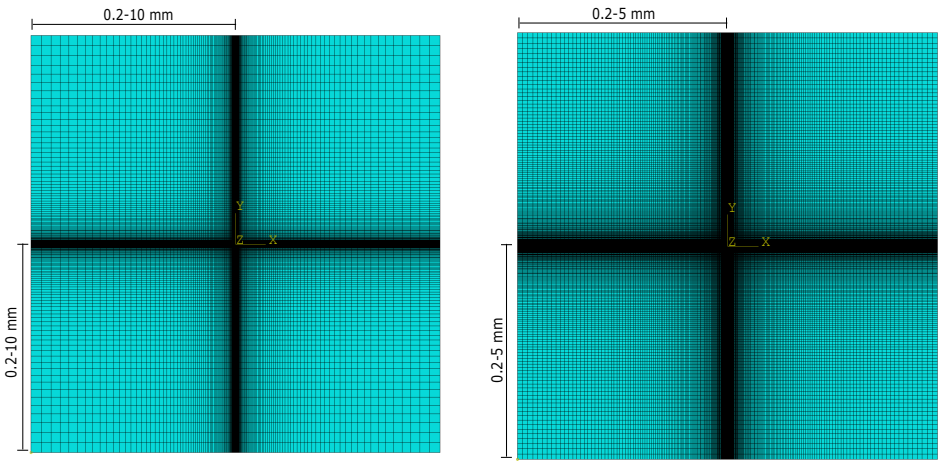
The number of elements can be altered by modifying its size. Table 4.6 presents the models used in this analysis and their parameters.

**Table 4.6:** Alternative cases to study mesh sensitivity.

| Model | Minimum element size (mm) | Maximum element size (mm) | Total number of elements - |
|---|---|---|---|
| Original | 0.2 | 10 | 394,384 |
| $Mesh_1$ | 0.2 | 5 | 1132,096 |
| $Mesh_2$ | 0.3 | 10 | 322,624 |
| $Mesh_3$ | 0.4 | 10 | 278,784 |

Figure 4.14 shows the appearance of the model with the finer mesh, $Mesh_1$, and of the reference

model. As can be seen the number of elements is higher and their dimensions smaller, resulting in a wider centre localized fine mesh with a bigger quantity of elements. The time of the simulation was greatly augmented for the finer discretization, $\text{Mesh}_1$.




a) b)

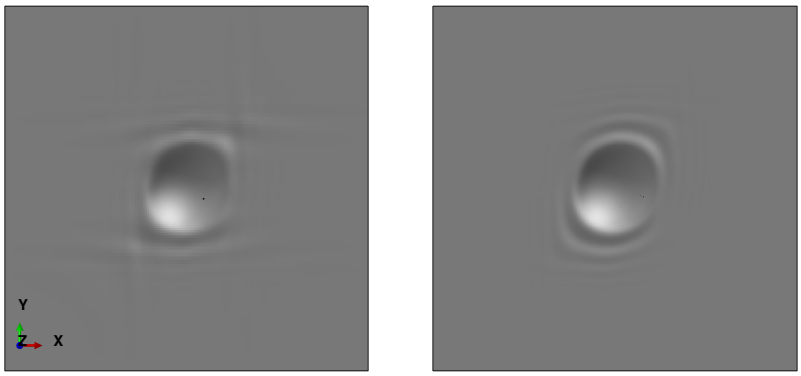
**Figure 4.14:** Meshes of a) the reference model and b) $\text{Mesh}_1$.

### 4.2.1 Discussion

Generally, the model with a finer mesh is able to produce more accurate and detailed results due to its very small and high number of elements, which greatly approximate the behaviour of the system to a real continuous system. The disadvantage is the computational time, which becomes significantly larger. The mesh sensitivity analysis provides a comparison between the results of similar models with different meshes, that allows to select the most appropriate model, the one which provides good results in an acceptable time.

As expected, the model $\text{Mesh}_1$, the model with highest number of elements, provided more detailed results and can be assumed the most accurate. Figure 4.15 makes a comparison of the deformed shape of the reference model and $\text{Mesh}_1$, where it is noticeable that model $\text{Mesh}_1$ creates more rounded and smooth surface lines/wrinkles, much closer to the deformed shapes of real planes.

The envelopes of the damage variables of the two top plies, Tables 4.7 and 4.8, show some differences between the models. Model $\text{Mesh}_2$ presents slightly smaller areas for the damage variable $d_1$, for both top layers, and much smaller area regarding the damage variable $d_2$ for the top layer. Thus, the envelope of the damage variable $d_6$ is also smaller in both layers. In addition, the deformed shape of this model shows significant differences: the outside wrinkle is not reproduced, the perimeter of the crater has a slightly smaller radius and it is closer to a circular shape, opposed to the more oval shape of the Original model and $\text{Mesh}_1$. Model $\text{Mesh}_3$, which is slightly coarser than $\text{Mesh}_2$, has similar results with less detail.

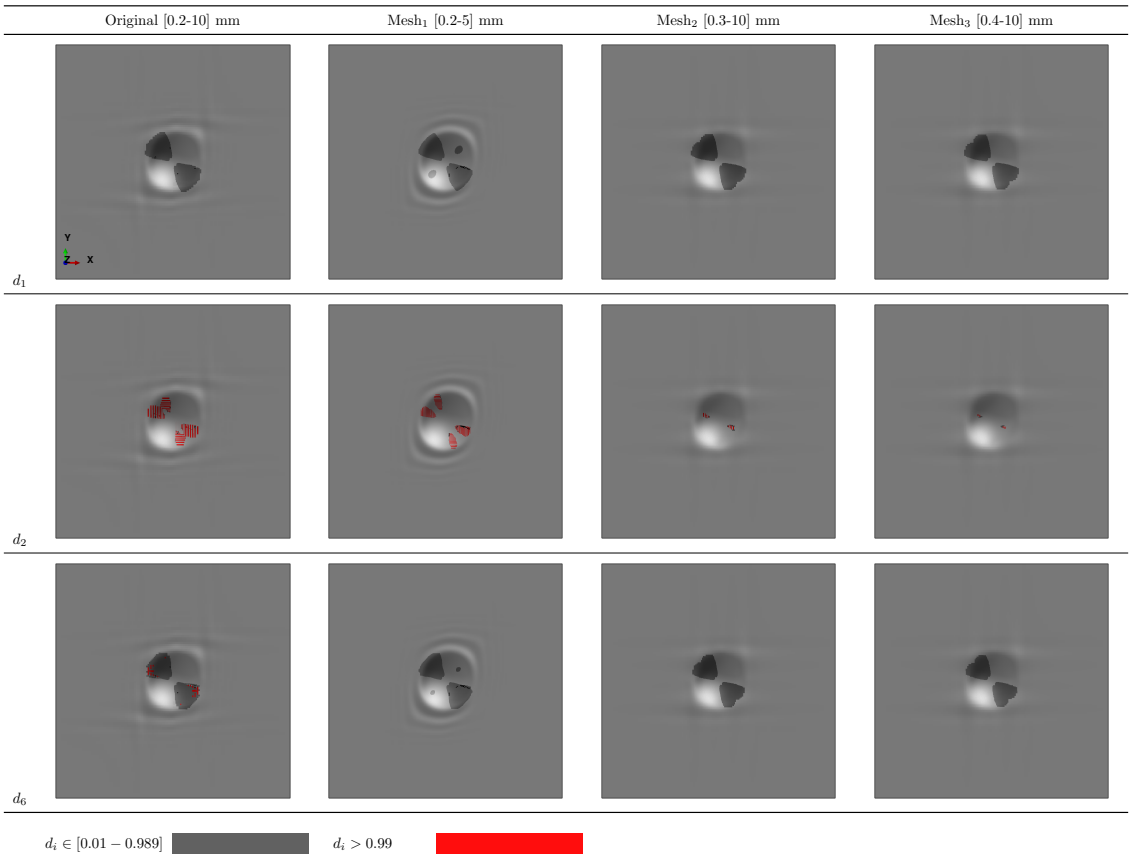



a) b)

**Figure 4.15:** Deformed shape of a) the reference model and b) $\text{Mesh}_1$.

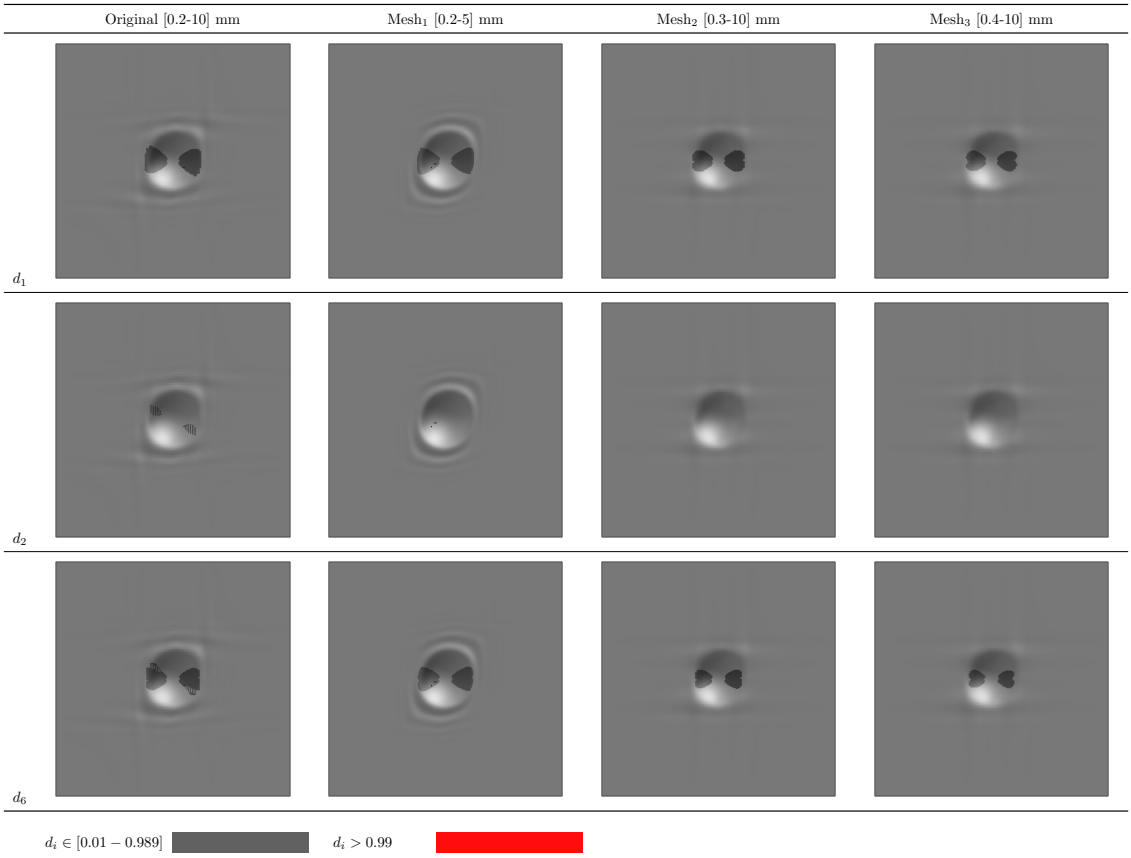
The envelopes of the damage variables of the reference model show very similar shapes, albeit they are a little more rough due to a coarser mesh than that of model $\text{Mesh}_1$. The areas of the envelopes are similar but slightly bigger, which makes the reference model more conservative than model $\text{Mesh}_1$. Thus, regarding damage, the reference model is able to predict a behaviour that is very close to the model with a much finer mesh, with the advantage of requiring less computational effort.

**Table 4.7:** Maps of the envelope of the damage variables of the top ply for the mesh sensitivity analysis at 80 $\mu$s.




Figures 4.16 and 4.17 provide respectively a comparison of the maximum principal stress field at the instant when the maximum values are achieved, t=20 $\mu$s, and the internal variable

**Table 4.8:** Maps of the envelope of the damage variables of the second topmost ply for the mesh sensitivity analysis at 80 $\mu$s.




corresponding to fibre tensile failure at the top and second topmost layer. When compared to the reference model, the stress field of models Mesh$_2$ and Mesh$_3$ shows a slight different shape, for both layers and the zones of maximum stress are smaller as well as the maximum stress value obtained, Table 4.9.

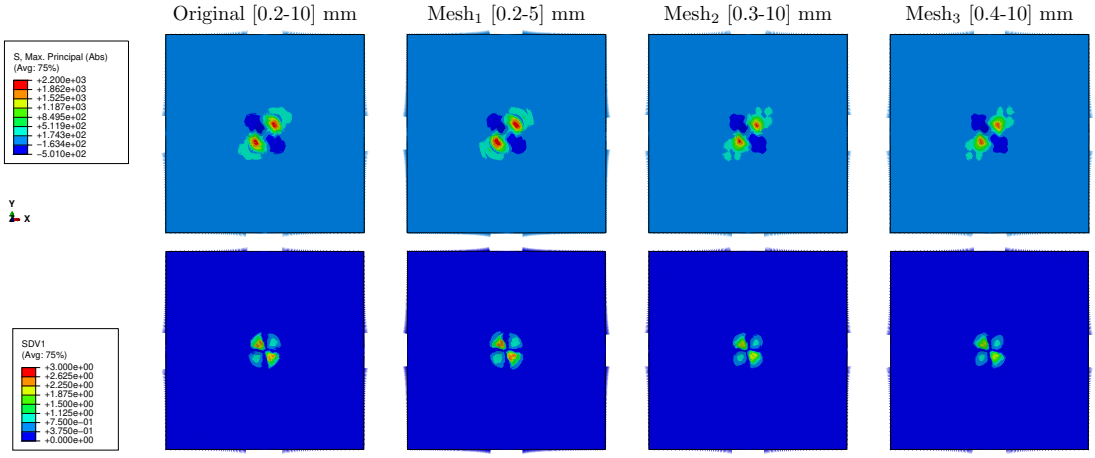



**Figure 4.16:** Comparison of the Maximum Principal (Absolute) stress fields (top) and internal variable corresponding to fibre tensile failure (bottom) of the top layer.

### 4.2. Mesh Sensitivity

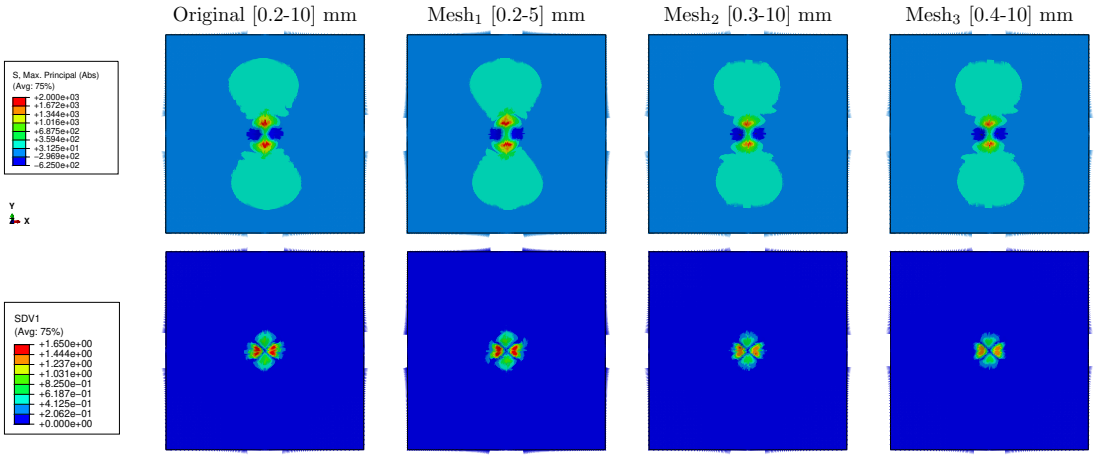



**Figure 4.17:** Comparison of the Maximum Principal (Absolute) stress fields (top) and internal variable corresponding to fibre tensile failure (bottom) of the second topmost layer.

These two models show significant differences in predicting the stress field, providing maximum values considerably smaller, explaining the smaller damaged areas. The response of the internal variable corresponding to fibre tensile failure also highlight the different behaviour of models $\text{Mesh}_2$ and $\text{Mesh}_3$, representing a significantly lower level of tensile damage in the fibres. These two models, although faster, are not able to provide results with acceptable accuracy and their behaviour is not conservative.

**Table 4.9:** Maximum values of the Maximum Principal (Absolute) stress of the two top plies for the mesh sensitivity analysis.

| | Original [0.2-10] mm | $\text{Mesh}_1$ [0.3-10] mm | $\text{Mesh}_2$ [0.2-5] mm | $\text{Mesh}_3$ [0.4-10] mm |
|---|---|---|---|---|
| Top layer | 2178.73 MPa | 1933.99 MPa | 2198.03 MPa | 1877.61 MPa |
| Second topmost layer | 1920.51 MPa | 1739.26 MPa | 1968.3 MPa | 1656.33 MPa |

Once again the Original model showed very similar results to the model with the most refined mesh. Figure 4.18 presents the displacement of the centre of the plate in the thickness direction of all models, where the time history for both the Original model (witout *mass scaling*) and model $\text{Mesh}_1$ (with *mass scaling*) is incomplete due to the time required to complete the simulations. The displacement is similar for all models up to 80 $\mu$s, where the time history for the Original model ends. After this instant, the displacement of model $\text{Mesh}_1$ has a slight different behaviour comparing to models $\text{Mesh}_2$ and $\text{Mesh}_3$, which are similar, providing a slightly higher displacement. This result is in accordance with the previous results where models $\text{Mesh}_2$ and $\text{Mesh}_3$ have reported smaller values, and where the Original model has shown very similar behaviour to the most refined model. Thus, according to the previous results, the displacement that the reference model provides is similar to the most refined model.

This analysis revealed that the mesh applied to the Original model presented accurate enough results, very close to those of a model with almost 3 times more elements. The loss in detail of the solutions is very small considering the gain in CPU time, once *mass scaling* is applied.

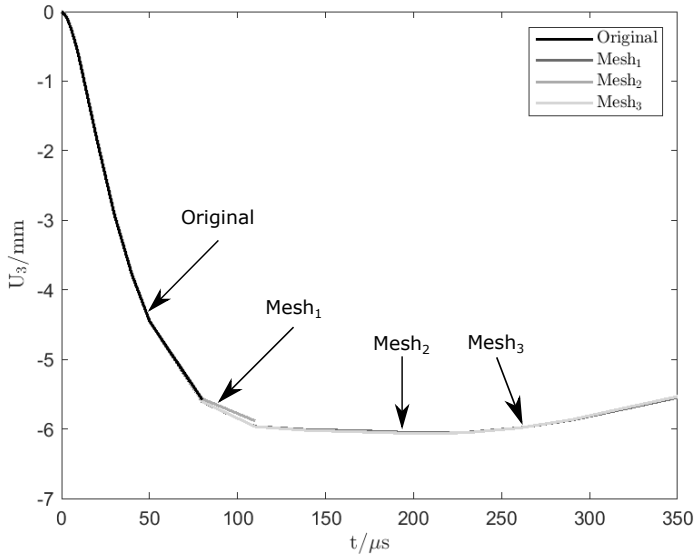



**Figure 4.18:** Comparison of the displacement of the centre of the top layer.

## 4.3 Conclusions

This particular study was realized because of the necessity to reduce significantly the computational time of the model used to perform the parametric analysis of this work. The method chosen relied upon *selective mass scaling* as being the most adequate method and the one which introduces less changes to the model. Abaqus allows for this method to be implemented automatically and intuitively by selecting the minimum allowable time increment of the model. This is materialized by increasing the density of the elements which have the time increment smaller than the one prescribed. The bigger the time increment chosen is, the highest the number of elements that will have its density increased, whereas a smaller time increment affects less elements. The amount of elements which have their density increased is relevant as it may introduce significant changes to the mass matrix of the system leading to different results. On the other hand, a bigger time increment leads to a smaller computation time which was the goal. Therefore, a trade-off is performed to get the best compromise between computational time and accuracy.

A parametric study was needed to understand the sensitivity of the model to *mass scaling* and to establish the adequate minimum time increment to apply to the model. Various models were tested varying only the minimum time stable increment. The kinetic and the internal energies were compared to identify the minimum stable time increment that provided a similar behaviour to the reference model and smaller computational time. The most adequate model defined a minimum stable time increment of $1 \times 10^{-10}$ s with the lowest mass change and better compromise between accuracy and CPU time. It can be concluded that the applicability of *selective mass scaling* is an adequate method to pursuit time efficiency in the simulations.

An analysis of mesh sensitivity was also developed to understand the influence of the mesh on the solutions. When an analysis is performed on a finite element model, the accuracy obtained may be inadequate due to insufficient mesh refinement. To unveil if the mesh applied is adequate to produce the precision required it is necessary to perform a parametric analysis altering the mesh of the model. The refinement of the mesh increases the number of elements which leads to more precise results but also higher CPU time.

In the analysis performed, the two most refined models (Original and $\text{Mesh}_1$) presented similar

results with very small variations, although with very different number of elements, thus showing that the solution is converging. The selection relied upon the second most refined model (Original) as a consequence of the small error in relation to the most refined model, and a much higher computational efficiency.

# Chapter 5

# Finite element analysis and parametric study

The reference model for this parametric analysis is an 8 ply CFRP plate $[45/90/-45/0]_s$ and its mesh is composed of finite elements of sizes that range from the minimum size of 0.2 mm to maximum size of 10 mm. *Mass scaling* is applied and is defined by a minimum increment time step of $1 \times 10^{-10}$ $\mu$s. The measurement of velocity and displacement is realized at the bottom ply, the opposed face to where the lightning strike is applied, at five discrete points simulating VISAR measurements. These "virtual sensors" are located on the centre of the plate and around it, Figure 5.1.

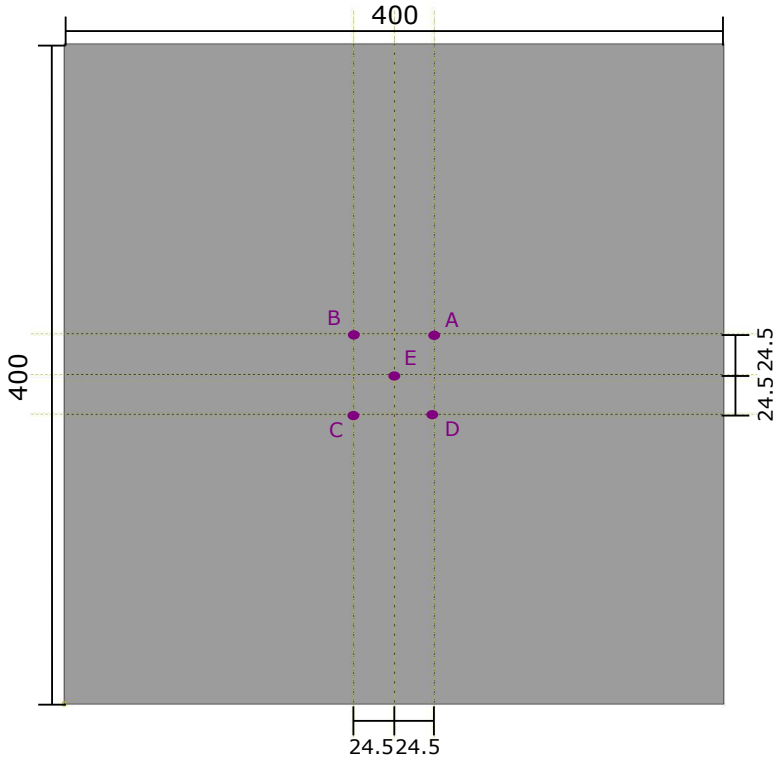



**Figure 5.1:** Geometry of the finite element model.

Figure 5.2 shows the evolution of warping on the centre of the plate, at the end of each step. As expected, it is small at the initial stages, becoming wider and more significant towards the end. Li

et al. [35], through experimental tests, showed that the fibre damage is confined to a circle within the centre of the plate. Similar results were obtained with the present model, Figure 5.3.

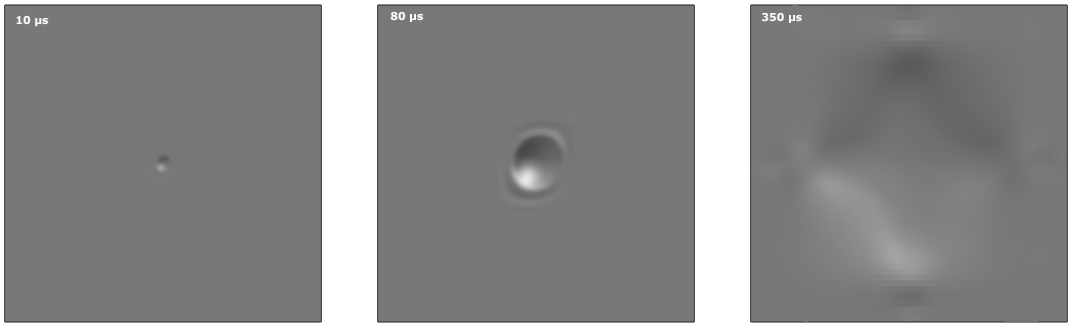
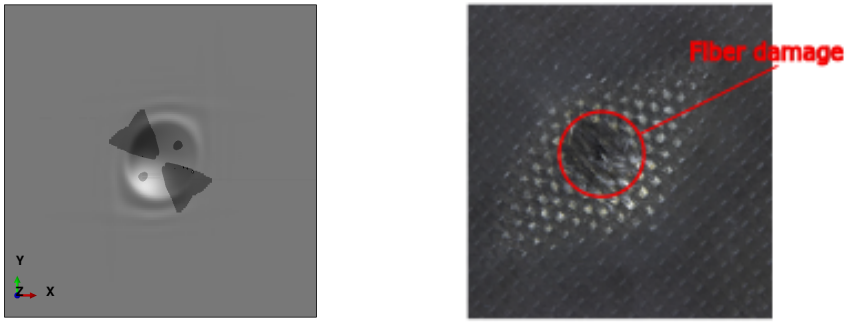



**Figure 5.2:** Evolution of the deformed shape of the top ply of the Original model.




a b

**Figure 5.3:** Comparison of top layer fiber damage of a) the Original model at 80 $\mu$s and b) similar real tested laminate [35].

The measurement of displacement and velocity imposed by the lightning strike at the centre of the laminate is presented in Figures 5.4 and 5.5. The maximum velocity and displacement is measured at the point of lightning strike application, the centre of the plate of designation E. The surrounding points of measurement, A, B, C and D show nonzero displacement from $t = 50$ $\mu$s onwards, which is the time it takes for the deformations to propagate to the circumference which contain these points. Nodes A and C have a distinct behaviour from nodes B and D. Nodes A and C show a higher positive displacement, at around $t = 50$ $\mu$s, before reaching the same displacement in the thickness direction as the centre. The deformed shape of the laminate shows that a small wrinkle is present around the crater, and due to its oval shape, nodes A and D are positioned right at the crest of the wrinkle at this instant, Figure 5.6, explaining the higher positive displacement observed at these two points. The maximum velocity is measured at the centre of the laminate, and thus the point with higher deformation achieving close to 6 mm of deflection. After the peak of the displacement, some oscillation is predicted due to a varying velocity in the time interval [120,300] $\mu$s. After 250 $\mu$s the centre recovers around 0.5 mm of deflection. The displacement of nodes A, B, C and D reach around 5.2 mm without oscillation for the simulated strike time.

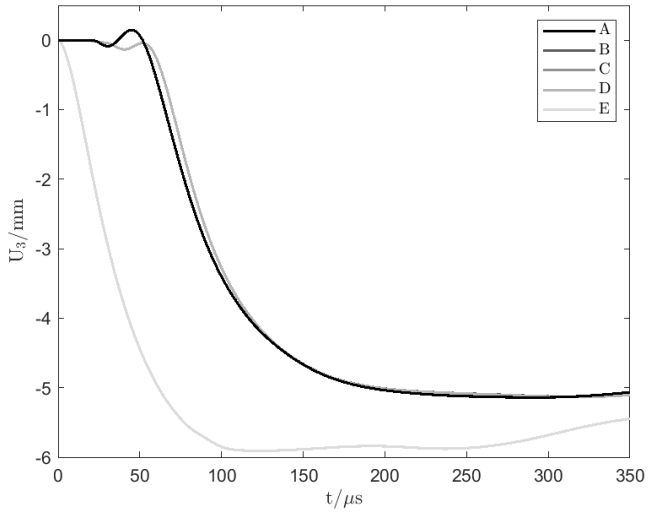



**Figure 5.4:** Measurement of the displacement in the thickness direction the Original model.

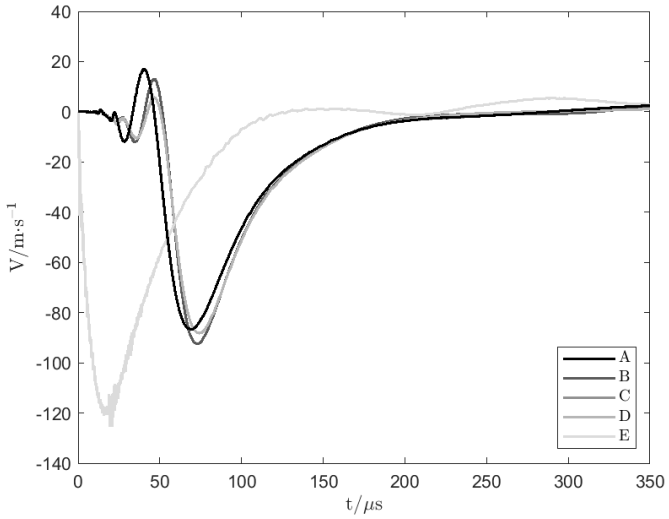
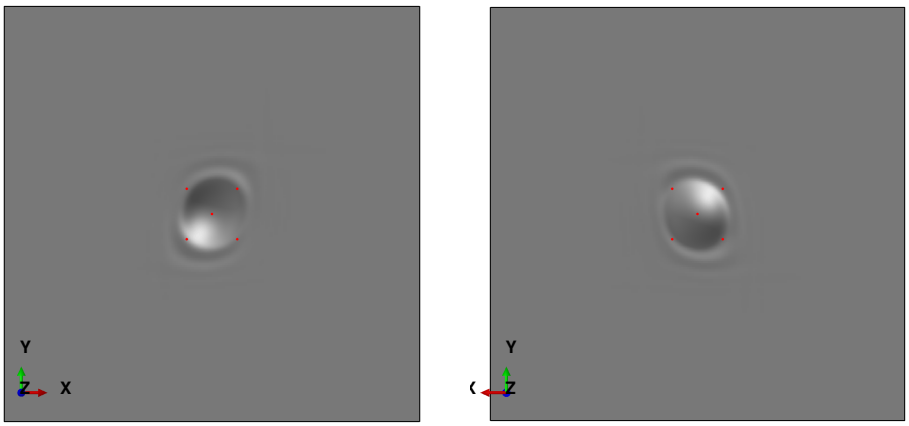



**Figure 5.5:** Measurement of the out-of-plane velocity of the Original model.




a b

**Figure 5.6:** Deformed shape of the top ply of the Original model from top) front and bottom) back at 80 $\mu$s.

## 5.1 Stacking sequence analysis

To analyse the influence of the fibre relative angle, a parametric analysis of the stacking sequence was performed. The analysed models were all quasi-isotropic varying the relative position of the plies within the laminate. Table 3.2 presents the stacking sequences considered.

Kawakami [39] concluded that the fibre relative angle has influence on the projected damage area and no effect on the damage depth. The relative fibre angle affects the damage distribution by changing its shape, due to the damage growth being primarily dependent on the fibre orientation.

Tables 5.1 and 5.2 show the maps of the envelope of the damage variables of the two topmost plies for all models for the parametric analysis of the effect of fibre relative angle on the onset of damage. The results show that the damage distribution is influenced by the stacking sequence due to the different direction of the fibres. As expected, the variable of damage in the fibre direction, $d_1$, produces a damage distribution which propagates parallel to the fibre orientation of each ply. The matrix damage, $d_2$, is also influenced by the fibre direction, thus, it is also dependent on the stacking sequence as can be seen in Table 5.1. The load applied did not produce delamination in any of the models.

Models $SS_2$ and $SS_3$ have very similar damage areas with similar shapes to the original model, the only noticeable difference being the orientation of these areas, which are influenced by the direction of the fibres. Besides the orientation of the damage areas, Model $SS_1$ has a slightly bigger damage area for the variable $d_1$ of the top ply than the Original model. Model $SS_4$ is the model which presents most differences for fibre damage, $d_1$, presenting a bigger damage area for the top ply and smaller damage area at the second topmost ply. The damage was confined to the top layers as there was no damage present in any of the models below the third layer.

The deformed shape is also influenced by the stacking sequence as can be seen by the different shapes. Models $SS_2$, $SS_3$ and Original have an oval deformed shape. Model $SS_4$ has a circular shape and model $SS_1$ generates a deformed shape between the previous oval and circular shapes. Thus, the stacking sequence produces an effect on the evolution of the deformed shape. The in-plane properties of all models are the same, but the variation of the relative position of the sub-laminates originates different out-of-plane responses.

**Table 5.1:** Maps of the envelope of the damage variables of the top ply for the stacking sequence analysis at 80 $\mu$s.

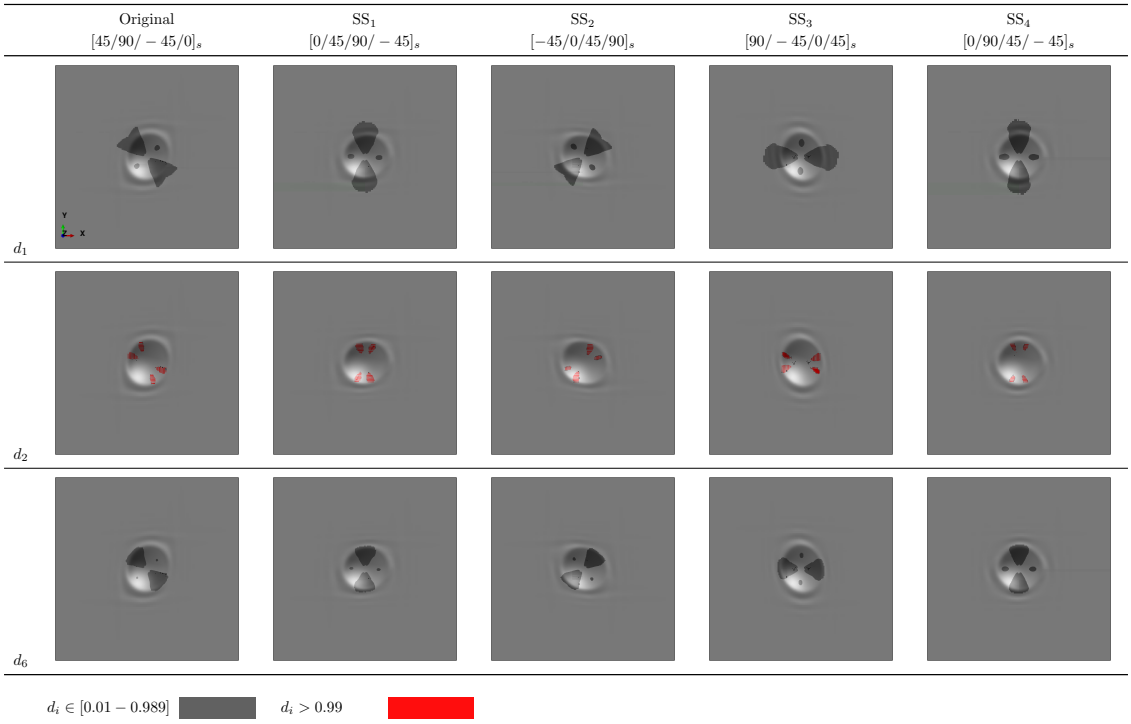
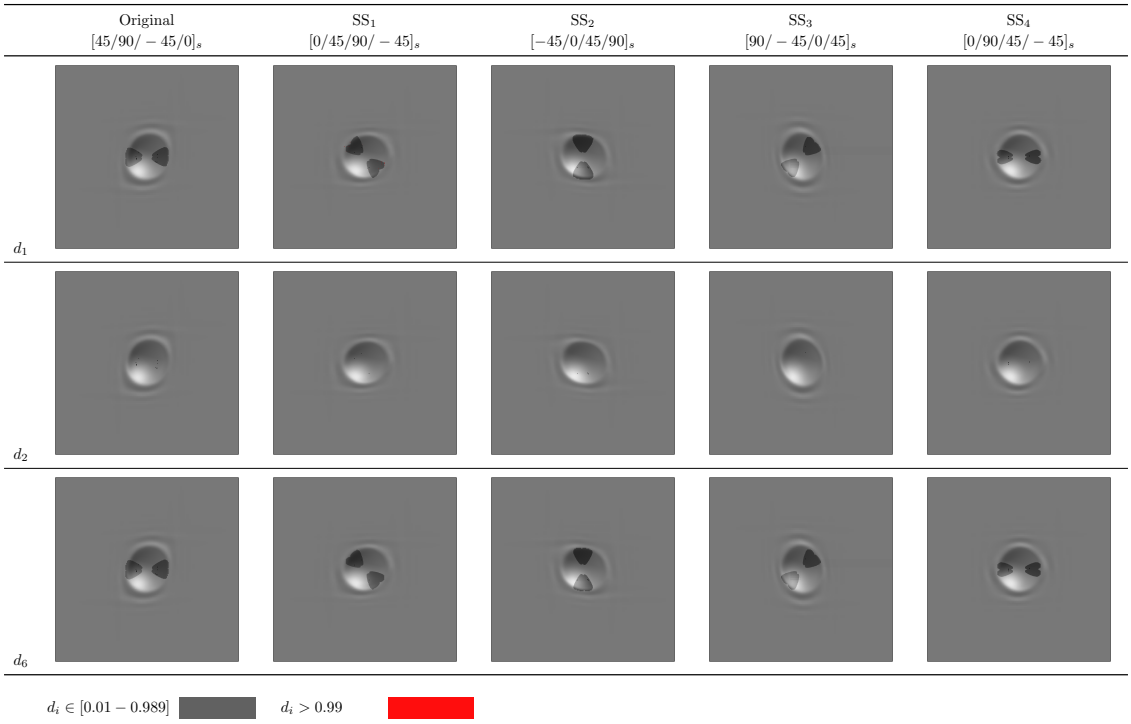



**Table 5.2:** Maps of the envelope of the damage variables of the second topmost ply for the stacking sequence analysis at 80 $\mu$s.



### 5.1. Stacking sequence analysis

The comparison of displacements, Figures 5.7 and 5.8, shows that the Original model and models $SS_2$ and $SS_3$ have very similar behaviour. The displacements of Models $SS_1$ and $SS_4$ have slight differences with respect to the Original model. Model $SS_1$ presents slightly smaller displacements regarding the positive displacements of points A, B, C, D at the crest of the wrinkle, while model $SS_4$ does not have positive displacements at points A, B, C, D.

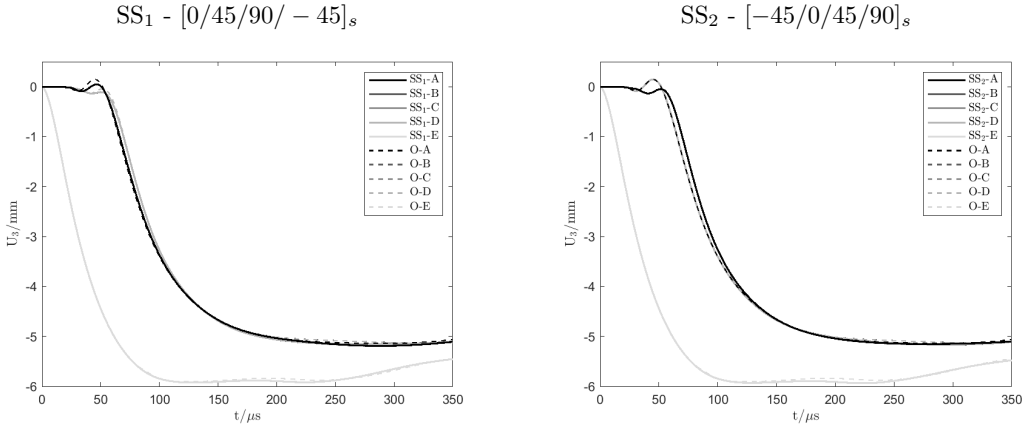



**Figure 5.7:** Comparison of displacement in the thickness direction of the measurement points of model $SS_1$ and model $SS_2$ with the Original model (O).

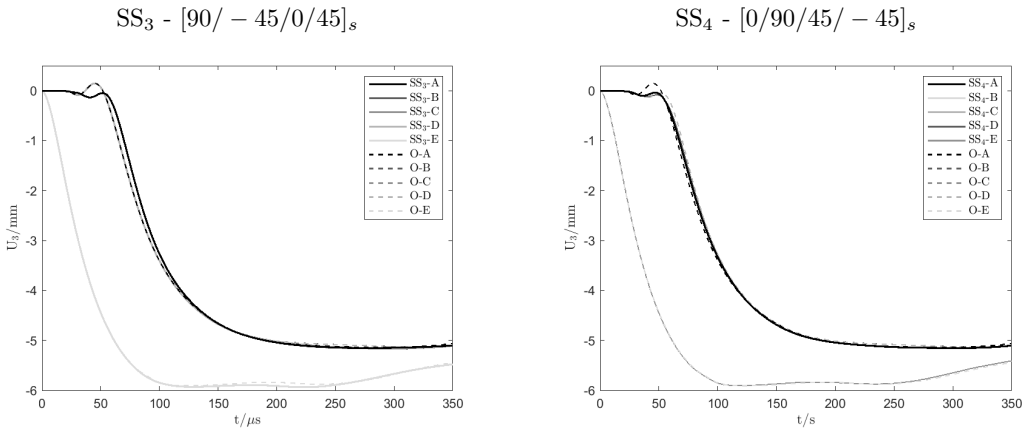



**Figure 5.8:** Comparison of displacement in the thickness direction of the measurement points of model $SS_3$ and model $SS_4$ with the Original model (O).

Figure 5.9 shows the deformed shape of both the Original and $SS_4$ models, at the instant in which the crest of the wrinkle achieves the points A, B, C, D. In the case of $SS_4$ the almost circular shape means that the four points are closely at equivalent heights in the crest, and thus, the displacements of the four points are similar.

The comparison of the measured velocities of the parametric models and the Original model is presented in Figures 5.10 and 5.11. Higher out-of-plane velocities may lead to higher installed stress state which can potentially lead to higher levels of damage.

The velocities measured at the centre of the plate were very similar for all models analysed. Models $SS_2$ and $SS_3$ show similar evolution of velocities with time, the only difference being the points which measure the highest velocities due to the different orientation of the oval shape. Both these models show higher maximum velocities of positive signal for points A, B, C, D than the




a) b)

**Figure 5.9:** Position of the measurement nodes relative to the crest of the deformed shape of a) Original and b) $SS_4$ models.

Original model. The node B of Model $SS_1$ has a different evolution of velocity than the same node of the original model, achieving higher maximum and higher minimum.

$SS_1$ - $[0/45/90/-45]_s$ $SS_2$ - $[-45/0/45/90]_s$

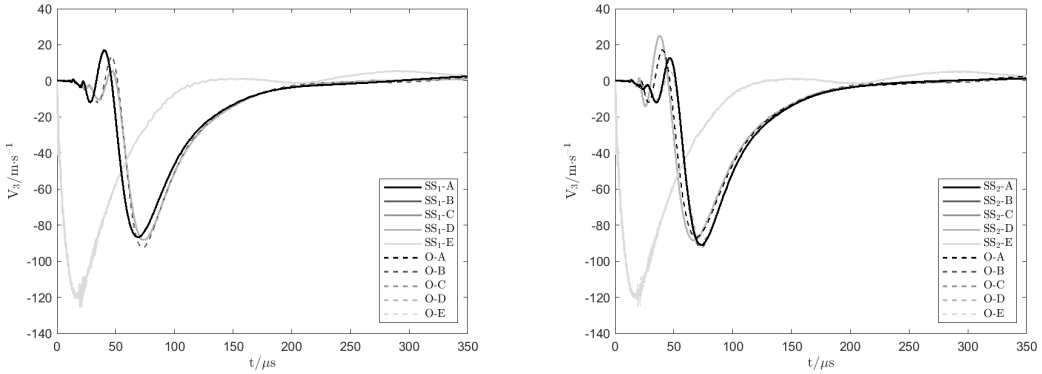



**Figure 5.10:** Comparison of the measurement of out-of-plane velocity of model $SS_1$ and model $SS_2$ with the Original model (O).

$SS_3$ - $[90/-45/0/45]_s$ $SS_4$ - $[0/90/45/-45]_s$

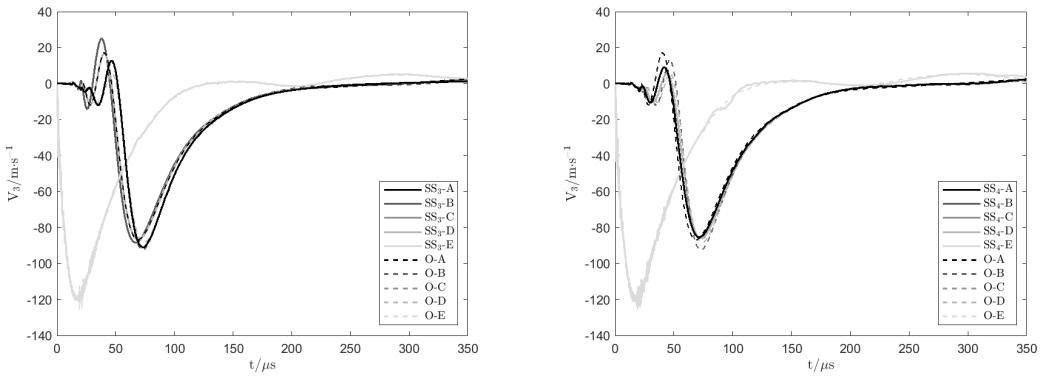
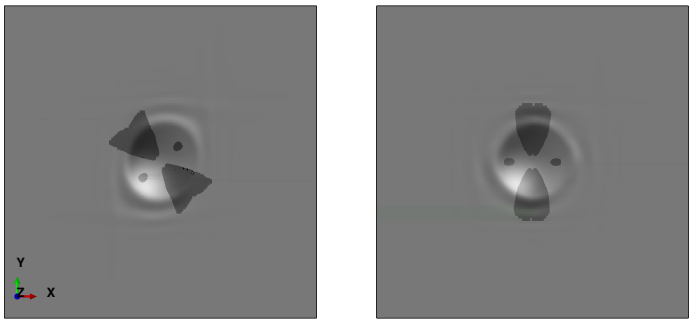



**Figure 5.11:** Comparison of the measurement of out-of-plane velocity of model $SS_3$ and model $SS_4$ with the Original model (O).

Model $SS_4$, apart from the central point which shows similar behaviour to the Original model,

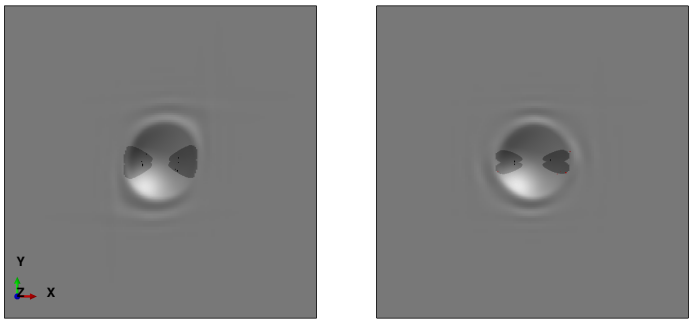
presents lower velocities of points A, B, C, D with lower velocity peaks, either positive or negative. This leads to smaller deformations and consequently can lead to less damage.

The model $SS_4$ is the model that presented more differences with respect to the Original model, and in regards to the maps of the damage variable $d_1$, Tables 5.1 and 5.2, it appears to have a behaviour more prone to sacrifice the external layer, presenting bigger damage area, protecting the inner layers as shown by the smaller damage area of its second topmost layer. Figures 5.12 to 5.14 provide a comparison, between the original model and $SS_4$, of the maps of the envelope of the damage variable $d_1$ for the top three layers. Although Figure 5.14 shows a slightly bigger damage area at the third layer for model $SS_4$, the maximum $d_1$ value achieved is below 0.2 which means there is barely any damage. Model $SS_4$ shows an improvement in damage behaviour over the Original model, absorbing/dissipating a greater amount of the energy damaging the first layer, which in turn protects the rest of the laminate, resulting in less damage in the inner layers.



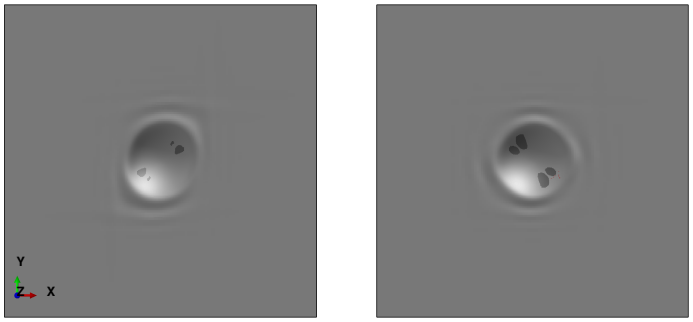

a) b)

**Figure 5.12:** Map of the envelope of the damage variable $d_1$ of the top layer of models a) Original and b) $SS_4$.




a) b)

**Figure 5.13:** Map of the envelope of the damage variable $d_1$ of the second topmost layer of models a) Original and b) $SS_4$.




a) b)

**Figure 5.14:** Map of the envelope of the damage variable $d_1$ of the third topmost layer of models a) Original and b) $SS_4$.

Regarding the mechanical effects of the lightning strike, through this parametric analysis it was possible to observe that the stacking sequence has influence on the damage distribution, not only on its orientation, but also on the size of the damage area. It also has an effect on the evolution of the deformed shape, provoked by the different out-of-plane properties of each stacking sequence. The stacking sequence also influences slightly the evolution of velocities which in turn influences the deformation patterns. Experimental evidence [35, 39] shows that the relative fibre orientation mainly affects the shape of the projected damage area, which can lead to a different damage extension, as confirmed by the present study. Finally, as stated in previous studies [35, 39], the stacking sequence has no effect on the damage depth.

## 5.2 Lay-up analysis

Lay-up parameters, such as ply thickness and fibre angle, influence the damage induced by lightning strike. Studies have shown that thicker ply blocks usually lead to a larger damage projected area [39, 40] and thicker skin panels have a better ability to protect the core layers from damage caused by lightning strikes.

The ply thickness effect on the damage distribution is analysed by a parametric study where the ply thickness is varied by comparing differently stacked laminates with similar fibre relative angle and internal ply clusters of various sizes. Table 3.3 presents the models used in this study.

Tables 5.3 and 5.4 present a comparison of the maps of each damage variable for the Original model and the Unidirectional model (UD). Tables 5.5 and 5.6 show the damage distribution for the top and second topmost layers of the other models.

The UD model shows considerable smaller damage distribution areas than the Original model for the damage variable related to the fibre direction, $d_1$, for both layers. But even though the area is smaller, the damage is very severe, Tables 5.3 and 5.4. At 80 $\mu$s there is already a great amount of broken fibres in both top layers of the UD model. In the case of a solicitation higher than the longitudinal tensile strength, the layer will break in the fibre direction, which in the finite element model corresponds to the deletion of the corresponding element (for $d_1 \approx 1$). It is assumed that a broken layer in the fibre direction ceases to contribute to the structural behaviour of the laminate.

The severe damage of this model is not restricted to the two top layers. Figure 5.15 shows the extent of damage through all the layers even at the bottom of the laminate. This laminate, which can be regarded as a very thick ply block of fibres oriented on the 0° direction, shows a

very poor behaviour to the mechanical effects of the lightning strike, allowing damage to propagate through the thickness, contrary to the models analysed so far which confined the damage to the top layers.

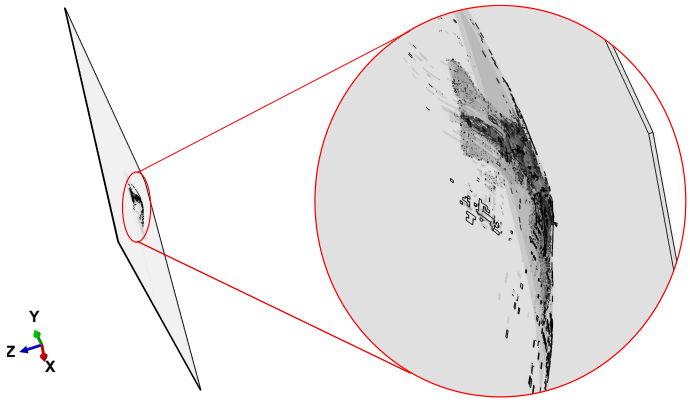
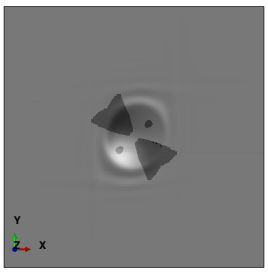
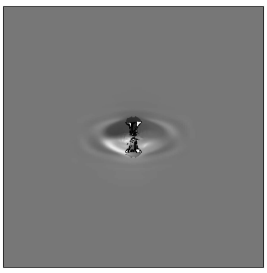
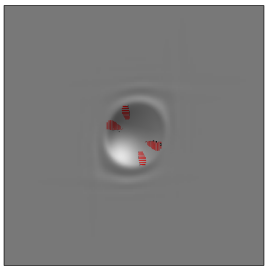
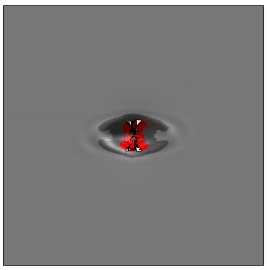
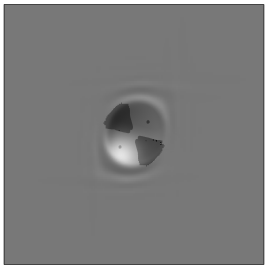
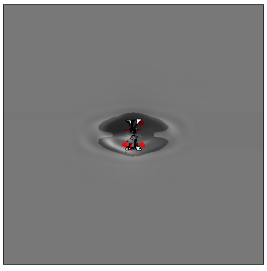


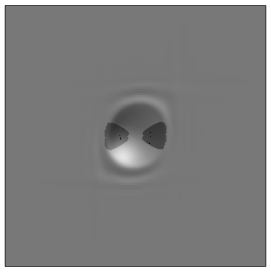
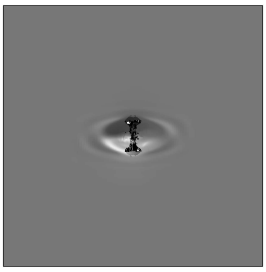
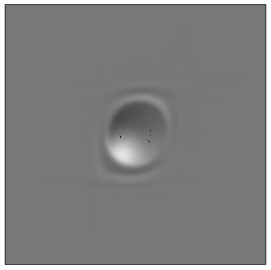
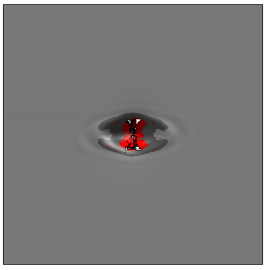
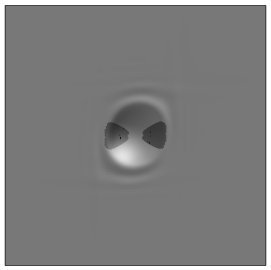
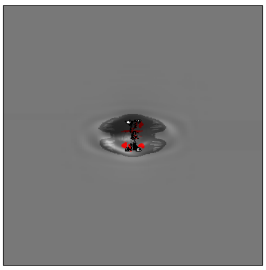

**Figure 5.15:** Detail of deleted elements throughout all plies of the UD model.

**Table 5.3:** Comparison between the maps of the envelope of the damage variables for the top ply of the Original model and UD model, at 80 $\mu$s.

| | Original $[45/90/-45/0]_s$ | UD $[0]_8$ |
|---|---|---|
| $d_1$ |  |  |
| $d_2$ |  |  |
| $d_6$ |  |  |
| | $d_i \in [0.01 - 0.989]$ | $d_i > 0.99$ |

The matrix damage of the UD model is also very significant as can be seen by the maps

**Table 5.4:** Comparison between the maps of the envelope of the damage variables for the second topmost ply of the Original model and UD model, at 80 $\mu$s.

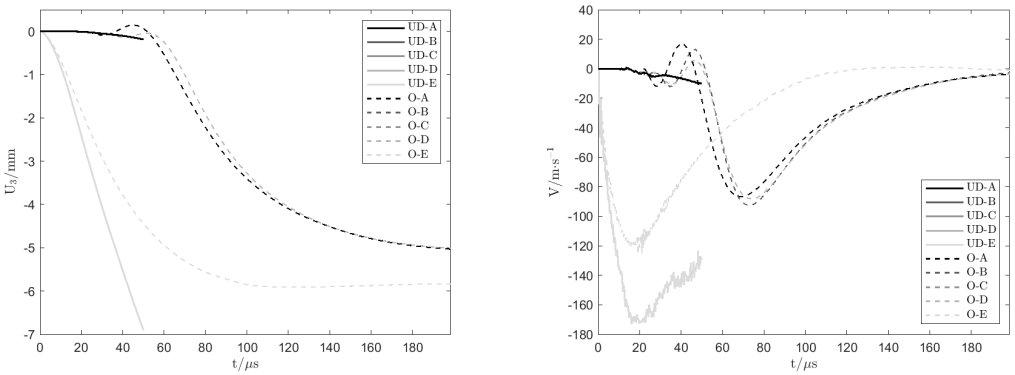
| | Original $[45/90/-45/0]_s$ | UD $[0]_8$ |
|---|---|---|
| $d_1$ |  |  |
| $d_2$ |  |  |
| $d_6$ |  |  |

$d_i \in [0.01 - 0.989]$ $d_i > 0.99$

of the damage variable $d_2$, presenting larger damage areas. Experimental evidence shows that the lightning-induced damage in UD laminates [7] can be substantially different from that of multidirectional laminates.

Figure 5.16 presents the measurement of the displacements and velocities of the UD model, in the thickness direction. The high deformations and damage developed in this model led to a very high computational time, thus the simulation was not completed. At 50 $\mu$s, the maximum displacement in the thickness direction of the centre of the UD model has not been achieved but it is already 7 mm, more than 1 mm higher than the maximum achieved by the Original model throughout the whole simulation. The velocities at the centre of the plate are almost 180 $\mathrm{m{\cdot}s^{-1}}$, much higher than those predicted in the Original model, which explains the large amount of damage.

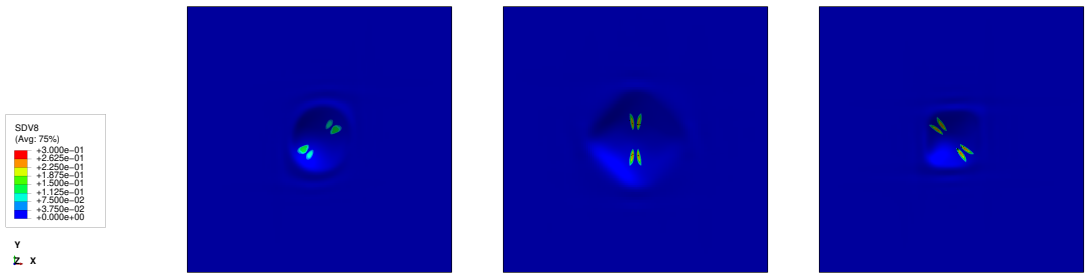
This analysis demonstrates the effect that thick ply blocks has on the behaviour of laminates to the mechanical effects of lightning strikes, showing that a unidirectional laminate has low resistance to this type of loading.




a b

**Figure 5.16:** Comparison of a) displacements in the thickness direction and b) predicted out-of-plane velocity of the UD model and Original model (O).

The CP and AP models present considerably smaller damage distribution areas in their top and second topmost layers when compared with the damage areas of the Original model, Tables 5.5 and 5.6. The relative fibre angle between layers is the same in both models, thus the really significant difference between their damage distribution maps is its orientation which is influenced by the stacking sequence. Figure 5.17 presents a comparison of fibre damage at the third laminate layer of the Original, CP and AP models which show that models CP and AP have smaller damage distribution areas in the third layer.




Original $[45/90/-45/0]_s$ CP $[0/90]_{2s}$ AP $[45/-45]_{2s}$

**Figure 5.17:** Comparison of fibre damage of the third layer of Original, CP and AP models.

Although, the damage areas of models CP and AP are generally smaller than the ones from the Original model, the measured displacements show higher values from 40 $\mu$s onwards at the centre of the plate, Figures 5.18 and 5.19. The evolution of displacements and its values are very similar between the two models and 1 mm higher than the displacements of the Original model from 100 $\mu$s onwards. This is justified by the measured velocities of these two models, Figures 5.20 and 5.21, which are very similar to the Original model, achieving a slightly higher maximum but retaining more velocity throughout the time and thus higher deformations.

In Tables 5.5 and 5.6 the damage of the topmost and second topmost layers of models CP1 and AP1 can also be seen. In the case of these two models, these two layers correspond to a thicker ply. Thus, what can be observed in these maps is the evolution of damage through the thickness of this thicker outer layer.

**Table 5.5:** Maps of the envelope of the damage variables of the top ply for the lay-up analysis at 80 $\mu$s.

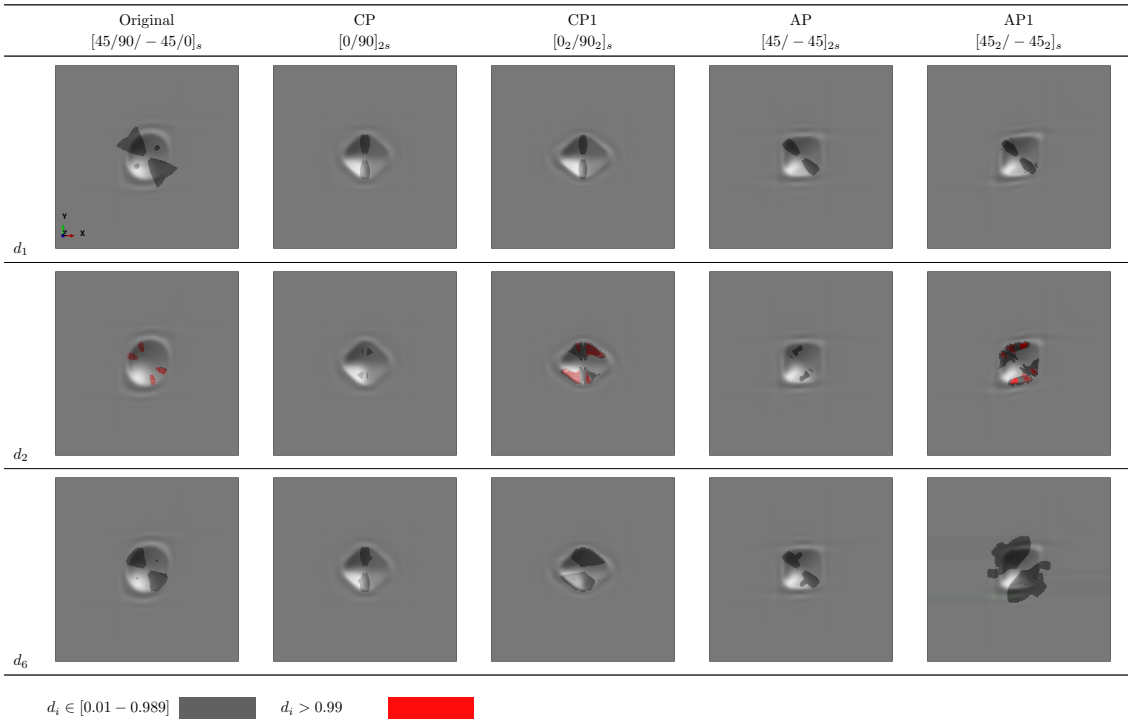
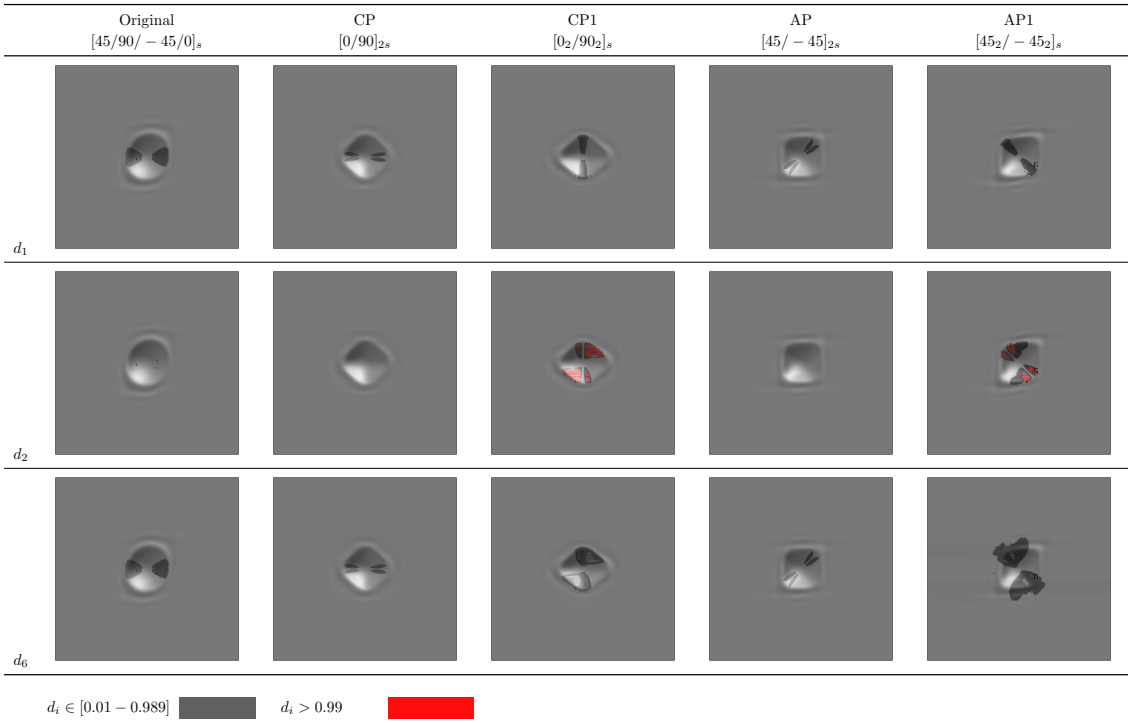



**Table 5.6:** Maps of the envelope of the damage variables of the second topmost ply for the lay-up analysis at 80 $\mu$s.




The top layer of models CP1 and AP1 have similar damage area distribution in the fibre direction, $d_1$, to the top layer of models CP and AP, respectively. This damage is practically constant throughout the thickness of the thicker layer of models CP1 and AP1, as can be seen by

a very similar damage area of the second topmost layer, Table 5.6.

The matrix damage of the top thicker layer of models CP1 and AP1 is much larger than that presented by models CP and AP, respectively. This can be attributed to the *in situ*, since thicker ply blocks have lower ply strengths (e.g. Figure 2.23). The top layer of models CP1 and AP1 show significant larger damage areas, as observed experimentally [39, 40]. Figures 5.22 and 5.23 show that the stress field of the third layer of CP1 and AP1 is larger, thus meaning that ply thickness affects the internal stresses in the laminate. Table 5.7 shows considerably larger damage distribution areas on the third layer of models CP1 and AP1.

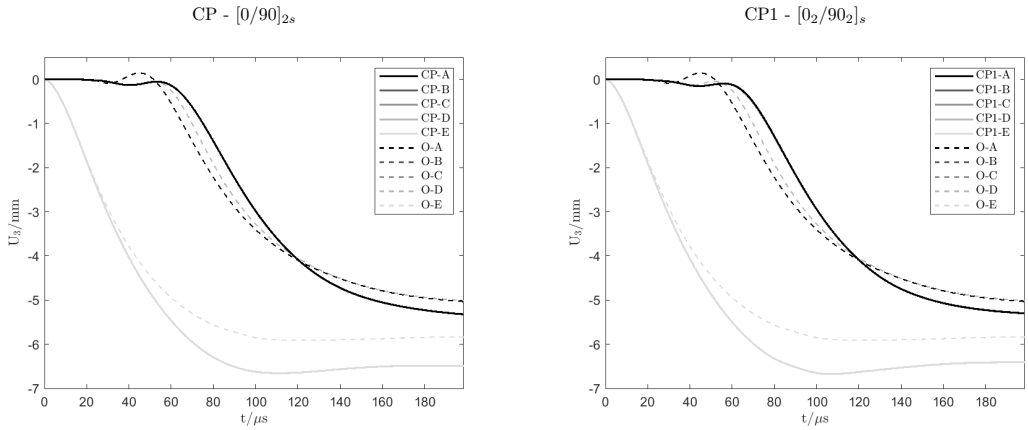



**Figure 5.18:** Comparison of displacement in the thickness direction of the measurement points of model CP and model $CP_1$ with the Original model (O).

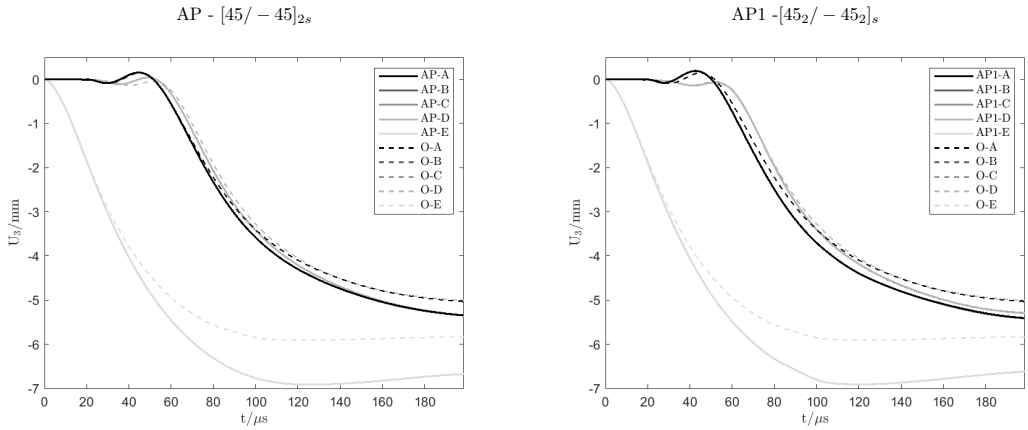



**Figure 5.19:** Comparison of displacement in the thickness direction of the measurement points of model AP and model $AP_1$ with the Original model (O).

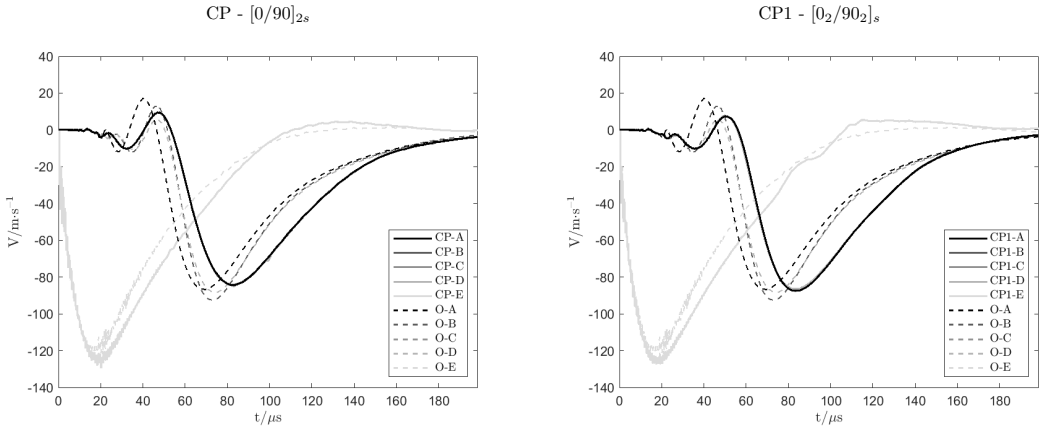



**Figure 5.20:** Comparison of the predicted out-of-plane velocity of model CP and model $CP_1$ with the Original model (O).

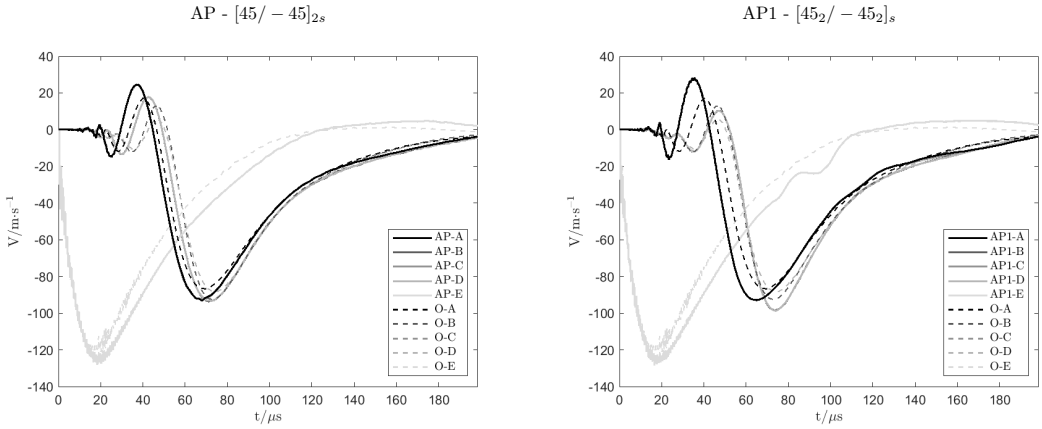



**Figure 5.21:** Comparison of the predicted out-of-plane velocity of model AP and model $AP_1$ with the Original model (O).

Figure 5.24 shows a slightly larger displacement field in the thickness direction and larger area of maximum displacement for the model CP1 than CP model. The maximum displacement is around 6.8 mm which is almost 1 mm higher than the maximum displacement of the Original model. Figure 5.25 shows similar behaviour for model AP1, the significant difference being the slightly higher displacements of models AP and AP1.

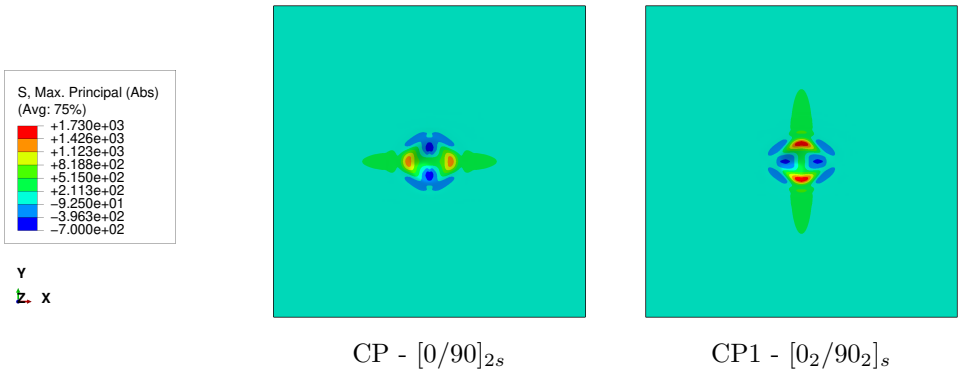
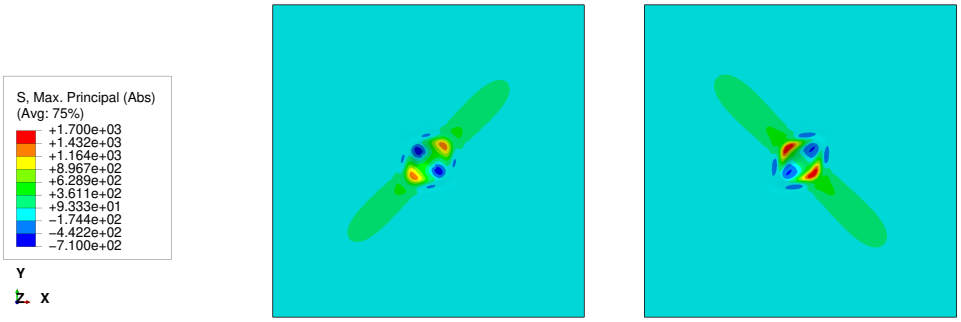



**Figure 5.22:** Maximum Principal stress (Absolute) of the third layer of models CP and CP1 at 40 $\mu$s.

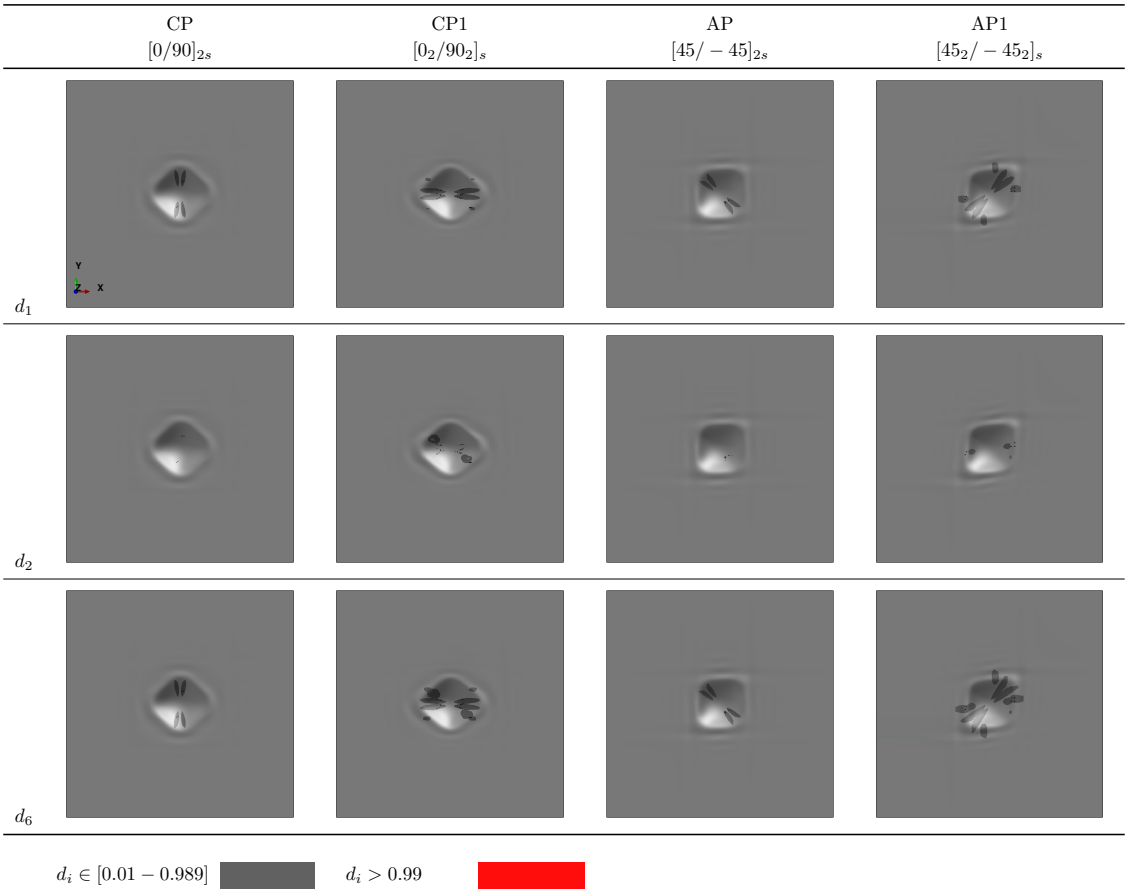
### 5.2. Lay-up analysis




AP - $[45/-45]_{2s}$ AP1 - $[45_2/-45_2]_s$

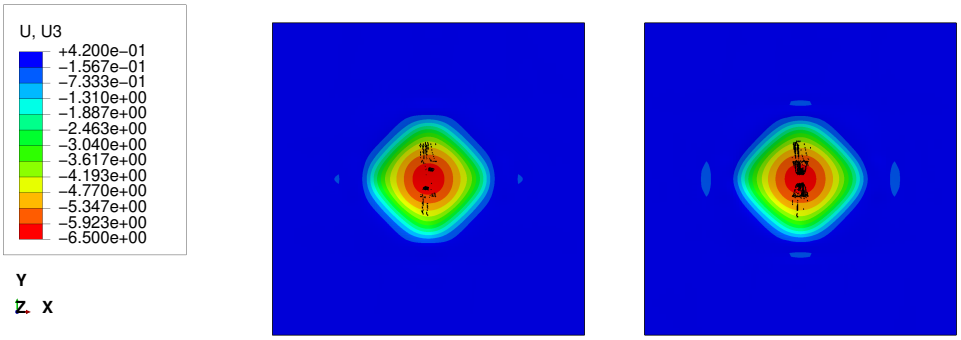
**Figure 5.23:** Maximum Principal stress (Absolute) of the third layer of models AP and AP1 at 40 $\mu$s.

**Table 5.7:** Maps of the envelope of the damage variables for the third topmost ply of models CP, CP1, AP and AP1 at 80 $\mu$s.



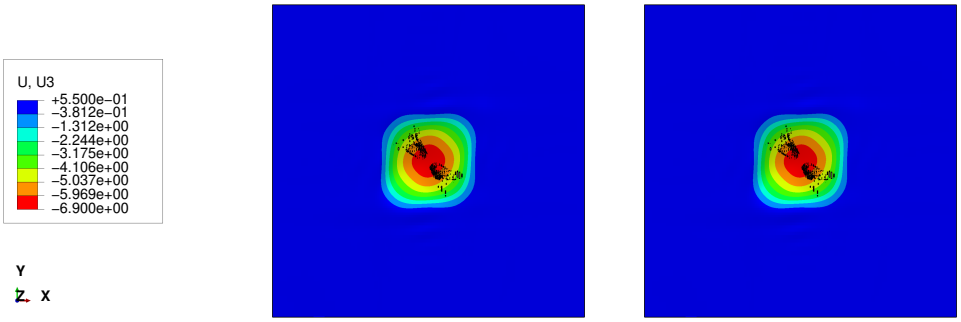

The deformed shape is, as already stated, influenced by the stacking sequence and its out-of-plane flexural properties, thus, all models reported different shapes, Figure 5.26. The deformed shape of the UD model is elongated in the direction of the fibres. Models CP and AP have the same fibre relative angle, hence, both deformed shapes have a very similar quadrangular shape. The different orientation of the quadrangular shape is an effect of the fibres direction in each model.

The deformed shape of Models CP1 and AP1 is very close to the deformed shape of models CP and AP, respectively. A small difference is observed due to the fibre direction of the thicker outer




CP - $[0/90]_{2s}$ CP1 - $[0_2/90_2]_s$

**Figure 5.24:** Displacement in the thickness direction of the top ply of models CP and CP1 at 170 $\mu$s.




AP - $[45/-45]_{2s}$ AP1 - $[45_2/-45_2]_s$

**Figure 5.25:** Displacement in the thickness direction of the top ply of models AP and AP1 at 170 $\mu$s.

ply block. Models CP1 and AP1 also present higher number of deleted elements at the top ply reflecting a higher damage at the top layer than the models CP and AP.

The results provided by the analysed models reached similar conclusions to those of previous studies [39, 40], which also validates the finite element model used. The models with thicker ply blocks revealed larger damage projected areas and also higher damage depth, as shown by the UD model. Models CP1 and AP1 showed that the thicker outer layer was more damaged than all remaining multi-directional models.

The lay-up certainly has an effect on the damage projected areas, and the proposed model captured these effects accurately. Thus, it showed the importance and relevance that computational modelling can have on the development, choice and optimization of laminates for application in an aircraft.

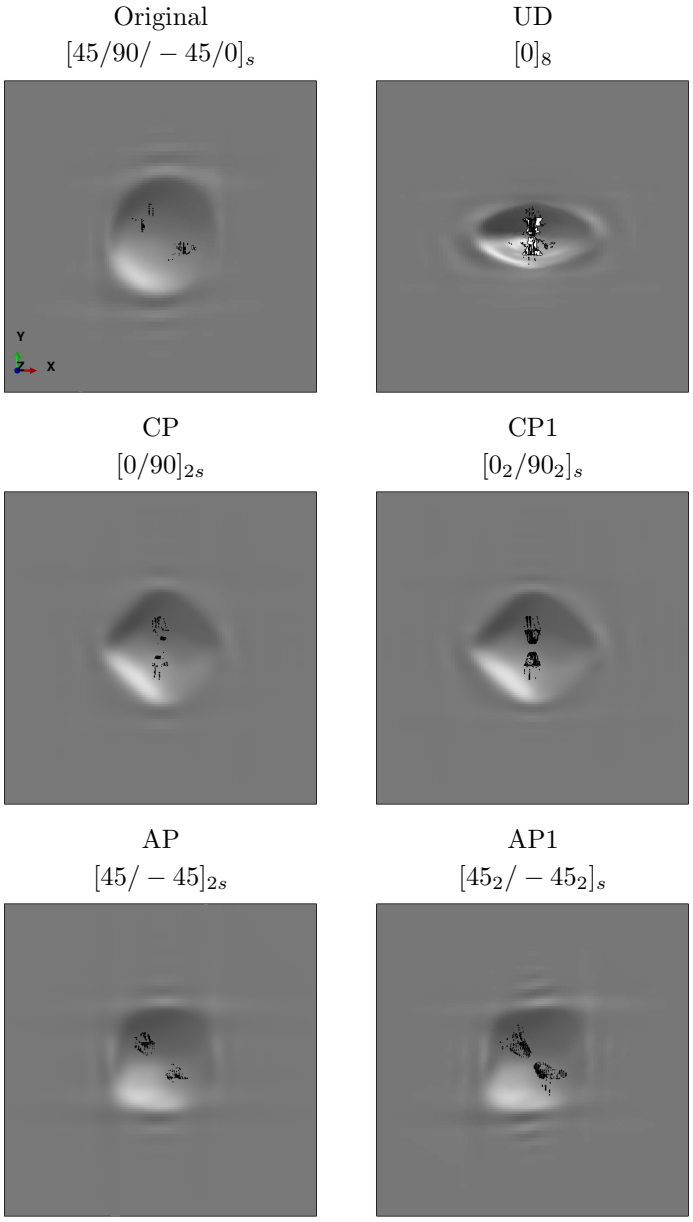



**Figure 5.26:** Comparison of the deformed shape of the lay-up alternative cases at 170 $\mu$s.

# Chapter 6

# Conclusions and future work

The aircraft industry is always searching for new ways to improve airplanes in order to satisfy the ever increasing demands. Contemporary challenges for aircraft are fuel efficiency and reducing the emission of greenhouse gases. There are several fields of improvement to achieve the goal, the more significant are: development of more efficient turbines, more efficient aerodynamics and reduce the overall weight of the structure. The first two fields are already considerably well developed and the weight of the aircraft is improving, in recent times, due to the use of carbon fibre composites in many primary structural parts of the airplane, such as wing boxes, fuselage and others, which has contributed to the weight reduction. However, the use of new materials is not straightforward as each material besides advantages also has its drawbacks. Carbon fibre composites present a very agreeable strength/weight relation but contrary to their metallic predecessors, these materials have lower electrical and thermal conductivity which lead to an increase in the thermo-mechanical constraints and turns a lightning strike into a serious threat to these materials and the structures of airplanes. Consequently, a lightning strike may induce serious damage to composites: fibre breakage, matrix burning and delamination in the thickness direction of the laminate. Thus, to certify aeronautic/aerospace composite structures manufacturers must be able to understand and predict the behaviour of these structures to a variety of lightning events.

In order to improve the behaviour of composites to lightning strikes, lightning protections are applied to the composites which in turn increase the weight of the structure reducing the benefits of these materials. The need to optimize these protections and laminates has become predominant. An accurate understanding of the lightning mechanisms, as well as models and computational tools to predict the behaviour of these materials when subjected to these solicitations, are essential for aircraft manufacturers. Computational models can aid in the pursue for the optimization of the laminates and its protections, thus improving the structures, and also reduce time and cost by avoiding numerous and costly tests.

The comprehension of the lightning strike and its direct effects on composite structures is very important because the total amount of inside damage and its detectability from the outside are serious issues for the industry. These damages: fibre breakage, matrix cracks and delamination, decrease the mechanical properties of the structures and may lead to structural failure of parts. The lightning strike is a complex event, which involves various physical processes: thermal, electromagnetic and mechanical, which can be coupled. The direct effects of the lightning strike introduce thermal and mechanical constraints to the structures. Thermal constraints can cause deformation, melting or puncture of the fuselage, and mechanical constraints may lead to fracture, delamination

and puncture of materials.

The aim of this study was to increase the knowledge of the damage caused by the mechanical forces, induced by the direct effects of lightning strikes, to the most commonly utilized laminates on the aeronautic industry. For this, a 3D finite element model was developed which included interlaminar and intralaminar damage models of the composite material. The intralaminar damage was included through a modified continuum damage mechanics model proposed by Miamí et al [8]. The interlaminar damage, or delamination, was modelled using a user-defined cohesive formulation [71]. The cohesive interaction is defined by a bilinear traction-separation damage law accounting for mode dependency according to the B-K law [76]. The mechanical loads applied to the model follows previous work [68], with focus on the main non-thermal damage mechanisms and the mechanical forces resulting from lightning strikes: the magnetic field induced by the current impressed on the structures, the shock waves due to surface-explosions and the shock waves from supersonic channel expansion.

Due to the complexity of the lighting strike mechanical effects and the damage behaviour of the composites, naturally, the model is also very complex and computationally very heavy, which means high periods of time to perform the simulations. In order to pursue computational efficiency, a *mass scaling* parametric study was performed. In this particular study, the density of the elements which have the time increment smaller than the one prescribed was increased. The bigger the time increment chosen, the higher the number of elements that had its density increased. The quantity of altered elements is relevant as it may introduce significant changes to the mass matrix of the system leading to different results. For a smaller computational time, bigger time increments revealed good performance. The parametric study revealed that the *mass scaling* method is adequate and was able to reduce considerably the CPU time of the model. A mesh sensitivity analysis was also performed to define the adequate mesh that could provide adequate and detailed results and an acceptable CPU time.

The model was applied to study the effect that the stacking sequence and lay-up of laminates have on the damage induced by the mechanical effects of lightning strikes. This was achieved through parametric studies in which the stacking sequence and the lay-up was altered.

The stacking sequence parametric study revealed that the stacking sequence has influence on the damage distribution, not only on its orientation, but it may also affect the size of the damage area. The stacking sequence also influences slightly the evolution of velocities which in turn influences the displacement and therefore, deformations. The deformed shape of the crater produced during loading is also influenced by the stacking sequence, because of the different out-of-plane properties of each stacking sequence. It was also verified that the stacking sequence has no effect on the damage depth.

The lay-up parametric study reached similar conclusions to those of previous studies [39, 40], which also validates the finite element model used. Laminates with thicker ply blocks revealed larger damage projected areas and also higher damage depth.

The lay-up analysis also showed that it has great influence on the damage projected areas, managing considerable reduction of these damage areas by altering the lay-up. Models CP and AP presented smaller damage areas together with higher deformations, in comparison to the Original model.

This work highlights the advantages that computational modelling can provide to the development, choice and optimization of laminates for application in an aircraft, through simulations that do not require fabrication of laminates nor expensive tests, allowing for the prediction of the

laminates behaviour in a cost-efficient and time saving manner.

For further studies, it would be interesting to analyse laminates with alternative stacking sequences and lay-ups (such as thicker outer layers and thin inner layers of different fibre orientations) in order to ascertain its benefits as this can be one way to optimize the laminates for the mechanical effects of lightning strikes. Moreover, none of the models analysed showed significant delamination, which previous studies concluded is greatly linked with the thermal constraints of the lightning strike, thus a future development would be to develop a model which would join the thermal effects to the mechanical effects here analysed, providing an ampler and complete information of the damage induced by lighting strikes to carbon composites.

# References


[1] Soulas F. Development of a lightning strike mechanical model for the prediction of damage of aeronautical composite panels. Ph.D. thesis; Institut Supérieur de l'Aéronautique et de l'Espace, Univ. Toulouse Midi-Pyrénés; 2016.

[2] Chemartin L, Lalande P, Peyou B, Chazottes A, Elias PQ, Delalondre C, et al. Direct effects of lightning on aircraft structure: Analysis of the thermal, electrical and mechanical constraints. Journal AerospaceLab 2012;5:1–15.

[3] Feraboli P, Miller M. Damage resistance and tolerance of carbon/epoxy composite coupons subjected to simulated lightning strike. Composites Part A: Applied Science and Manufacturing 2009;40(6-7):954–67.

[4] Lepetit B, Escure C, Guinard S, Revel I, Peres G. Thermo-mechanical effects induced by lightning on carbon fiber composite materials. In: 2011 International Conference on Lightning and Static Electricity (ICOLSE 2011). 2011, p. 1–2.

[5] US DOT/FAA Advisory Circular AC 25-21 Section 25.581 lightning protection . Certification of transport aircraft structures. 1999.

[6] Martins RS. Experimental and theoretical studies of lightning arcs and their interaction with aeronautical materials. Ph.D. thesis; Université Paris-Saclay; 2016.

[7] Mamizu H, Kuraishi A, Ikeda Y, Saito K, Wakayama T, Hirano Y, et al. Lightning damage evaluation of composite laminates using direct measurements. In: 2017 International Conference on Lightning and Static Electricity (ICOLSE 2017). 2017, p. 1–5.

[8] Maimí P, Camanho PP, Mayugo JA, Dávila CG. A continuum damage model for composite laminates: Part I — Constitutive model. Mech Mater 2007;39(10):897–908.

[9] Rakov V, Uman MA. Lightning: physics and effects. New York: Cambridge University Press; 2003.

[10] Fisher FA, Plumer JA. Lightning Protection of Aircraft. NASA; 1977.

[11] MacGorman DR, MacGorman R, Rust WD. The electrical nature of storms. Oxford University Press on Demand; 1998.

[12] Soula S. Electrical Environment in a Storm Cloud. J Aerosp Lab 2012;5:1–10.

[13] Schoene J. Direct and nearby lightning strike interaction with test power distribution lines. University of Florida; 2007.

[14] Takahashi T. Riming electrification as a charge generation mechanism in thunderstorms. J Atmos Sci 1978;35(8):1536–48.

**References**


[15] Stolzenburg M, Marshall TC. Charge structure and dynamics in thunderstorms. Space Sci Rev 2008;137(1).

[16] SAE Committee report:ARP-5412 . Aircraft lightning environment and related test waveforms. 1999.

[17] Legrand . Protection against lightning effects. 2009.

[18] Mazur V. Physical processes during development of lightning flashes. C R Physiques 2002;3(10):1393–409.

[19] Mazur V, Ruhnke LH. Model of electric charges in thunderstorms and associated lightning. J Geophys Res 1998;103(D18):23299–308.

[20] Cooray V. An introduction to lightning. Springer; 2015.

[21] Jones C, Rowse D, Odam G. Probabilities of catastrophe in lightning hazard assessments. Tech. Rep.; SAE Technical Paper; 2001.

[22] Larsson A. The interaction between a lightning flash and an aircraft in flight. C R Physique 2002;3(10):1423–44.

[23] Chemartin L. Modélisation des arcs électriques dans le contexte du Foudroiement des aéronefs. Ph.D. thesis; Université de Rouen; 2008.

[24] EUROCAE ED-84 . Aircraft lightning environment and related test waveform standard. 1997.

[25] Karch C, Metzner C. Lightning protection of carbon fibre reinforced plastics—an overview. In: 2016 33rd International Conference on Lightning Protection (ICLP). IEEE; 2016, p. 1–8.

[26] Tholin L, Chemartin P, Lalande F. Numerical investigation of the surface effects on the dwell time during the sweeping of lightning arcs. In: 2013 International Conference on Lightning and Static Electricity (ICOLSE 2013). 2013, p. 1–11.

[27] EUROCAE ED-91 . Aircraft lightning zoning. 1998.

[28] Zaglauer H, Lalande P. Zone definitions on a generic aircraft and helicopter. EU Project FULMEN AL-95-SC.204 – D4.2b; 1999.

[29] Neufeld RB. Lightning direct effects on anisotropic materials from electro-thermal simulation. In: 2015 International Conference on Lightning and Static Electricity (ICOLSE 2015). 2015, p. 7 (5 .)–7 (5 .).

[30] Hirano Y, Katsumata S, Iwahori Y, Todoroki A. Artificial lightning testing on graphite/epoxy composite laminate. Composites Part A: Applied Science and Manufacturing 2010;41(10):1461–70.

[31] Lepetit B, Soulas F, Guinard S, Revel I, Peres G, Duval Y. Analysis of composite panel damages due to a lightning strike: mechanical effects. In: Int. Conf. on Lightning Static Electricity (Seattle); vol. 5. 2013, p. 1–8.

[32] Bigand A, Duval Y. Quantification of the mechanical impact of lightning strike protection explosion confined by thick paint. In: 2013 International Conference on Lightning and Static Electricity (ICOLSE 2013); vol. 1. 2013, p. 1–6.

[33] Kamiyama S, Hirano Y, Okada T, Ogasawara T. Lightning strike damage behavior of carbon fiber reinforced epoxy, bismaleimide, and polyetheretherketone composites. Composites Science and Technology 2018;161:107–14.

[34] Sonehara T, Hirano Y, Kusano H, Tokuoka N. Visualization of lightning impulse current discharge on CFRP laminate. In: 2014 International Conference on Lightning Protection (ICLP). IEEE; 2014, p. 835–9.

[35] Li Y, Li R, Lu L, Huang X. Experimental study of damage characteristics of carbon woven fabric/epoxy laminates subjected to lightning strike. Composites Part A: Applied Science and Manufacturing 2015;79:164–75.

[36] Hosokawa N, Ooto T, Kubo S, Anzai M, Yoshiya A, Nakagoshi A. Lightning strike protection for composite laminates by pitch-based carbon fiber skin. In: 19th International Conference on Composite Materials, Montreal, Canada. 2013, p. 1–10.

[37] Rupke E. Lightning direct effects handbook. Lightning Technologies Inc., Pittsfield; 2002.

[38] Naghipour P, Pineda EJ, Arnold S. Challenges in Modelling of Lightning-induced Delamination; Effect of Temperature-Dependent Interfacial Properties. In: 29th American Society for Composites Technical Conference. 2014, p. 1–12.

[39] Kawakami H. Lightning strike induced damage mechanisms of carbon fiber composites. Ph.D. thesis; University of Washington; 2011.

[40] Yamashita S, Sonehara T, Takahashi J, Kawabe K, Murakami T. Effect of thin-ply on damage behaviour of continuous and discontinuous carbon fibre reinforced thermoplastics subjected to simulated lightning strike. Composites Part A: Applied Science and Manufacturing 2017;95:132–40.

[41] Li Y, Li R, Huang L, Wang K, Huang X. Effect of hygrothermal aging on the damage characteristics of carbon woven fabric/epoxy laminates subjected to simulated lightning strike. Materials and Design 2016;99:477–89.

[42] Murillo R, Flourens F, Garcia V, Duval Y, Cavaliere F. Lightning strike protection of carbon composite skin. Kinetic and signature of the damage. In: 2017 International Conference on Lightning and Static Electricity (ICOLSE 2017). 2017, p. 1–13.

[43] Lepetit B, Escure C, Guinard S, Revel I, Peres G, Duval Y. Thermo-mechanical effects induced by lightning on carbon fiber composite materials. In: 2011 International Conference on Lightning and Static Electricity (ICOLSE 2011). 2011, p. 1–8.

[44] Karch C, Metzner C. Lightning protection of carbon fibre reinforced plastics — an overview. In: 2016 33rd International Conference on Lightning Protection (ICLP). IEEE; 2016, p. 1–8.

[45] Gagné M, Therriault D. Lightning strike protection of composites. Progress in Aerospace Sciences 2014;64:1–16.

[46] Daniel IM, Ishai O. Engineering mechanics of composite materials. Oxford university press New York; 2006.

[47] Dávila CG, Camanho PP, Cheryl A. Failure Criteria for FRP Laminates. J Compos Mater 2005;39:323–45.

[48] Puck A, Schürmann H. Failure analysis of FRP laminates by means of physically based phenomenological models. Composites Science and Technology 1998;58:1045–67.

[49] González C, LLorca J. Mechanical behavior of unidirectional fiber-reinforced polymers under transverse compression: Microscopic mechanisms and modeling 2007;67:2795 – 2806.

[50] Parvizi A, Garrett K, Bailey J. Constrained Cracking in Glass Fibre-reinforced Epoxy Cross-ply Laminates. Journal of Material Science 2002;13:195–201.

[51] Camanho PP, Dávila CG, Pinho ST, Iannucci L, Robinson P. Prediction of in situ strengths and matrix cracking in composites under transverse tension and in-plane shear. Composites Part A: Applied Science and Manufacturing 2006;37(2):165 –76.

[52] A. Puck HS. Failure analysis of FRP laminates by means of physically based phenomenological models. Composites Science and Technology 2002;62:1633–62.

[53] Argon AS. Fracture of Composites; vol. 1. Treatise of Materials Science and Technology Academic Press, New York; 1972.

[54] Catalanotti G, Camanho PP, Marques AT. Three-dimensional failure criteria for fiber-reinforced laminates. Compos Struct 2013;95:63–79.

[55] Pinho ST, Iannucci L, Robinson P. Physically-based failure models and criteria for laminated fibre-reinforced composites with emphasis on fibre kinking: part I: development. Composites Part A: Applied Science and Manufacturing 2006;37(1):63–73.

[56] Camanho PP, Arteiro A, Melro AR, Catalanotti G, Vogler M. Three dimensional invariant-based failure criteria for fibre-reinforced composites. Int J Solids Struct 2014;55:92–107.

[57] Vogler M, Rolfes R, Camanho P. Modeling the inelastic deformation and fracture of polymer composites — Part I: Plasticity model. Mech Mater 2013;59:50–64.

[58] Arteiro A. Technology development and structural mechanics of composites built of spread tow thin-ply technology. Master's thesis; University of Porto; 2012.

[59] Song K, Li Y, Rose C. Continuum damage mechanics models for the analysis of progressive failure in open-hole tension laminates. In: 52nd AIAA/ASME/ASCE/AHS/ASC Structures, Structural Dynamics and Materials Conference 19th AIAA/ASME/AHS Adaptive Structures Conference 13t. 2011, p. 1861.

[60] António RM. Analytical and numerical modelling of damage and fracture of advanced composites. Ph.D. thesis; University of Porto; 2011.

[61] Dávila CG, Camanho PP. Failure Criteria for FRP Laminates in Plane Stress. NASA Langley Research Center,Hampton, Virginia 2003;L-19012:1–28.

[62] Turon A, J. JC, Maimí P, Trias D, Mayugo JA. A progressive damage model for unidirectional fibre-reinforced composites based on fibre fragmentation. Part I: Formulation. Compos Sci Technol 2005;65:2039–48.

[63] Ladevéze P, Lubineau G, Violeau D, Marsal D. A computational damage micromodel for laminate composites. In T. Sadowski, editor, IUTAM Symposium on Multscale Modelling of Damage and Fracture Processes in Composite Materials. Springer 2006;:1–12.

[64] Dávila CG, Rose CA, Iarve EV. Modeling fracture and complex crack networks in laminated composites. In: Mathematical methods and models in composites; vol. 5. World Scientific; 2014, p. 297–347.

[65] Soden PD, Kaddour AS, Hinton MJ. Recommendations for designers and researchers resulting from the world-wide failure exercise. Compos Sci Technol 2004;64:589–604.

[66] Peerlings RHJ, de Borst R, Brekelmans WAM, Geers MGD. Localisation issues in local and nonlocal continuum approaches to fracture. Eur J Mech A-Solid 2002;21:175–89.

[67] González C, Llorca J. Mechanical behavior of unidirectional fiberreinforced polymers under transverse compression: Microscopic mechanisms and modeling. Compos Sci Technol 2007;67:2795–806.

[68] Karch C, Arteiro A, Camanho PP. Modelling mechanical lightning loads in carbon fibre-reinforced polymers. Int J Solids Struct 2019;162:217–43.

[69] Karch C, Wulbrand W. Contributions of Lightning Current Pulses to Mechanical Damage of Protected CFRP Structures: Part 1 - Theoretical Survey. 2013.

[70] Karch C, Honke R, Steinwandel J, Dittrich K. Contributions of lightning current pulses to mechanical damage of cfrp structures. In: 2051 International Conference on Lightning and Static Electricity (ICOLSE 2015). IET; 2015, p. 1–8.

[71] Dassault Systems Simulia Corp . Abaqus 6.14 Documentation. Providence, RI, USA; 2014.

[72] Maimí P, Camanho PP, Mayugo JA, Dávila CG. A continuum damage model for composite laminates: Part II — Computational implementation and validation. Mech Mater 2007;39:909–19.

[73] Arteiro A, Gray P, Camanho PP. Edge impact and compression after edge impact simulations in cfrp laminates 2018;Submitted for publication to Compos Struct.

[74] Malvern LE. Introduction to the Mechanics of a Continuous Medium. Prentice-Hall, Englewood Cliffs; 1969.

[75] Bazant ZP, Oh BH. Crack band theory for fracture of concrete. Materials and structures 1983;16:155–177.

[76] Benzeggagh ML, Kenane M. Measurement of mixedmode delamination fracture toughness of unidirectional glass/epoxy composites with mixed-mode bending apparatus. Compos Sci Technol 1996;49:439 – 449.

[77] Turon A, Camanho PP, Costa J, Dávila C. A damage model for the simulation of delamination in advanced composites under variable-mode loading. Mechanics of materials 2006;38(11):1072–89.

[78] Olovsson L, Simonsson K, Unosson M. Selective mass scaling for explicit finite element analyses. Int J Numer Meth Engng 2005;63(10):1436–45.

[79] Olovsson L, Simonsson K. Iterative solution technique in selective mass scaling. Int J Numer Meth Engng 2006;22(1):77–82.

[80] Askes H, Nguyen DC, Tyas A. Increasing the critical time step: micro-inertia, inertia penalties and mass scaling. Comput Mech 2011;47(6):657–667.

[81] Cocchetti G, Pagani M, Perego U. Selective mass scaling and critical time-step estimate for explicit dynamics analyses with solid-shell elements. Computers & Structures 2013;127:39–52.

[82] Chung WJ, Cho JW, Belytschko T. On the dynamic effects of explicit FEM in sheet metal forming analysis. Engineering Computations 1998;15:6:750–776.